Publication Year	2018
Acceptance in OA	2020-10-23T10:46:52Z
Title	Cosmic evolution and metal aversion in superluminous supernova host galaxies
Authors	Schulze, S., Krühler, T., Leloudas, G., Gorosabel, J., Mehner, A., Buchner, J., Kim, S., Ibar, E., Amorín, R., Herrero-Illana, R., Anderson, J. P., Bauer, F. E., Christensen, L., de Pasquale, M., de Ugarte Postigo, A., GALLAZZI, Anna Rita, Hjorth, J., Morrell, N., Malesani, D., Sparre, M., Stalder, B., Stark, A. A., Thöne, C. C., Wheeler, J. C.
Publisher's version (DOI)	10.1093/mnras/stx2352
Handle	http://hdl.handle.net/20.500.12386/27956
Journal	MONTHLY NOTICES OF THE ROYAL ASTRONOMICAL SOCIETY
Volume	473

Monthly Notices
of the
ROYAL ASTRONOMICAL SOCIETY

MNRAS **473,** 1258–1285 (2018) doi:10.1093/mnras/stx2352
Advance Access publication 2017 September 13

Cosmic evolution and metal aversion in superluminous supernova host galaxies

S. Schulze,[1,2,3★] T. Krühler,[4] G. Leloudas,[1,5★] J. Gorosabel,[6,7,8] A. Mehner,[9] J. Buchner,[2,3] S. Kim,[2] E. Ibar,[10] R. Amorín,[11,12] R. Herrero-Illana,[8,9] J. P. Anderson,[9] F. E. Bauer,[2,3,13] L. Christensen,[5] M. de Pasquale,[14] A. de Ugarte Postigo,[8] A. Gallazzi,[15] J. Hjorth,[5] N. Morrell,[16] D. Malesani,[5] M. Sparre,[17] B. Stalder,[18] A. A. Stark,[19] C. C. Thöne[8] and J. C. Wheeler[20]

Affiliations are listed at the end of the paper

Accepted 2017 September 8. Received 2017 September 4; in original form 2016 December 18

ABSTRACT

The SUperluminous Supernova Host galaxIES survey aims to provide strong new constraints on the progenitors of superluminous supernovae (SLSNe) by understanding the relationship to their host galaxies. We present the photometric properties of 53 H-poor and 16 H-rich SLSN host galaxies out to $z \sim 4$. We model their spectral energy distributions to derive physical properties, which we compare with other galaxy populations. At low redshift, H-poor SLSNe are preferentially found in very blue, low-mass galaxies with high average specific star formation rates. As redshift increases, the host population follows the general evolution of star-forming galaxies towards more luminous galaxies. After accounting for secular evolution, we find evidence for differential evolution in galaxy mass, but not in the B band and the far-ultraviolet luminosity (3σ confidence). Most remarkable is the scarcity of hosts with stellar masses above $10^{10}\,\mathrm{M}_\odot$ for both classes of SLSNe. In case of H-poor SLSNe, we attribute this to a stifled production efficiency above ∼0.4 solar metallicity. However, we argue that, in addition to low metallicity, a short-lived stellar population is also required to regulate the SLSN production. H-rich SLSNe are found in a very diverse population of star-forming galaxies. Still, the scarcity of massive hosts suggests a stifled production efficiency above ∼0.8 solar metallicity. The large dispersion of the H-rich SLSNe host properties is in stark contrast to those of gamma-ray burst, regular core-collapse SN, and H-poor SLSNe host galaxies. We propose that multiple progenitor channels give rise to this subclass.

Key words: galaxies: evolution – galaxies: high-redshift – galaxies: luminosity function, mass function – galaxies: starburst – galaxies: star formation.

1 INTRODUCTION

In the past decade, untargeted supernova (SN) surveys, e.g. the Texas SN Search (Quimby et al. 2005), the ROTSE SN Verification Project (Yuan et al. 2007), the Palomar Transient Factory (PTF; Law et al. 2009), and Pan-STARRS (PS; Tonry et al. 2012), discovered a new class of SNe with peak magnitudes exceeding $M_\mathrm{V} = -21$ mag (Gal-Yam 2012). These so-called superluminous supernovae (SLSNe) have been a focus of SN science ever since, because of the opportunity they provide to study new explosion channels of very massive stars in the distant Universe (Howell et al. 2013; Cooke et al. 2012), the interstellar medium (ISM) in distant galaxies (Berger et al. 2012; Vreeswijk et al. 2014), and their potential use for cosmology (Inserra & Smartt 2014; Scovacricchi et al. 2016). In addition, SLSNe provide a new opportunity to pinpoint star-forming (SF) galaxies independently of galaxy properties, which can ultimately lead to a better understanding of galaxy evolution at the faint end of luminosity and mass functions (MFs, Lunnan et al. 2014; Leloudas et al. 2015c; Angus et al. 2016; Chen et al. 2016; Perley et al. 2016b). Despite these prospects, SLSNe are very rare. At $z \sim 0.2$, one H-poor SLSN is expected to be produced for every 1000–20 000 core-collapse SNe (CCSNe, hydrogen-rich SLSNe have a higher rate; Quimby et al. 2013a).

Phenomenologically, SLSNe can be classified by their hydrogen content into H-poor and H-rich SLSNe. The light curves of H-poor SLSNe (SLSNe-I), identified as a new class of transients by

---

★E-mail: steve.schulze@weizmann.ac.il (SS); giorgos@dark-cosmology.dk (GL)

Published by Oxford University Press on behalf of the Royal Astronomical Society

Quimby et al. (2011c), are ∼3.5 mag brighter and three times broader than regular stripped-envelope SNe, but the shapes of their light curves are similar (e.g. Quimby et al. 2011c; Inserra et al. 2013; Nicholl et al. 2015a). Early spectra of H-poor SLSNe show a characteristic w-shaped absorption feature at ∼4200 Å due to oxygen in the ejecta (Quimby et al. 2011c) that is usually not seen in Type Ibc SNe (e.g. Modjaz et al. 2009). About a month after maximum light, the ejecta cool down to temperatures typical of regular Type Ibc SNe at maximum light. At that point, SLSN spectra also exhibit absorption features similar to Type Ibc SNe (e.g. Pastorello et al. 2010; Inserra et al. 2013; Nicholl et al. 2014).

A subgroup of H-poor SLSNe shows exceptionally slowly rising and slowly declining light curves ($\tau_{\rm rise} > 25$ d and $\tau_{\rm decay} > 50$ d; Nicholl et al. 2015a), hereafter called slow-declining SLSN-I. In some cases, the decay slope is comparable to that of the radioactive decay of ^{56}Ni. Gal-Yam et al. (2009) argued that in the case of SN2007bi, the SN was powered by the radioactive decay of several solar masses of ^{56}Ni (Gal-Yam 2012), which were synthesized during a pair-instability SN (PISN) of a star with a zero-age-main-sequence (ZAMS) mass of $M_{\rm ZAMS} \sim 200\,{\rm M}_{\odot}$ (e.g. Fowler & Hoyle 1964; Barkat, Rakavy & Sack 1967; Bisnovatyi-Kogan & Kazhdan 1967; Rakavy & Shaviv 1967; Fraley 1968; Heger et al. 2003; Woosley, Blinnikov & Heger 2007). However, the SN was discovered only shortly before it reached maximum light. Information about the rise time was not available, which is critical to distinguish between SN models. The well-sampled SLSNe PTF12dam and PS1-11ap, which were spectroscopically similar to SN2007bi at late times, had rise times that were incompatible with PISN models (Nicholl et al. 2013). This also cast doubt on the PISN interpretation of SN2007bi. However, recent findings by Kozyreva et al. (2017) showed that PISN models can predict short rise times similar to that of PTF12dam. Models of PISN spectra, on the other hand, are incompatible with the spectra of PTF12dam and SN2007bi (Dessart et al. 2013; Chatzopoulos et al. 2015; Jerkstrand et al. 2016).

The energy source powering H-poor SLSNe is highly debated. The most discussed models include magnetars formed during the collapse of massive stars (e.g. Kasen & Bildsten 2010; Inserra et al. 2013), the interaction of the SN ejecta with dense H-deficient circumstellar material (CSM) expelled by the progenitor prior to the explosion (Woosley et al. 2007; Blinnikov & Sorokina 2010; Chevalier & Irwin 2011; Chatzopoulos & Wheeler 2012; Quataert & Shiode 2012; Sorokina et al. 2016), PISNe, and pulsational PISNe (e.g. Woosley et al. 2007; Yan et al. 2015).

Hydrogen-rich SLSNe are characterized by an initial blue continuum and narrow Balmer lines, similar to classical Type IIn SNe (Schlegel 1990; Filippenko 1997; Kiewe et al. 2012) which are powered by the interaction of the SN with its CSM (e.g. Chevalier & Irwin 2011). Recent observations suggest a richer phenomenology. Spectra of the SNe 2008es and 2013hx showed broad H α emission components and their light curves showed a linear decline after maximum, similar to normal IIL SNe (Gezari et al. 2009; Miller et al. 2009; Inserra et al. 2016). Another intriguing object is CSS121015:004244+132827 (hereafter called CSS121015). It first evolved as an H-poor SN, but at 49 d after the maximum, its spectrum showed broad and narrow H α emission lines (Benetti et al. 2014). These properties are different from superluminous Type IIn SNe. Because of the similarities to Type II SNe, we label this subclass SLSN-II.

The possible diversity of SLSN progenitors suggests ZAMS masses up to a few hundred solar masses. Given the characteristic distance scale of SLSNe, a direct search for their progenitors is unfeasible. Alternatively, host observations have the potential to indirectly provide constraints on the progenitor population. The first systematic study of a sample of 17 H-poor and H-rich SLSNe by Neill et al. (2011) suggested that the hosts are low-mass galaxies with high specific star formation rates (sSFRs) between 10^{-8} and $10^{-9}\,{\rm yr}^{-1}$. However, these measurements are very uncertain because of the limited available wavelength coverage. This initial finding was supported by studies of the hosts of SN2010gx (Chen et al. 2013) and PS1-10bzj (Lunnan et al. 2013). Their spectroscopic observations also showed that both events occurred in low-metallicity galaxies with $Z < 0.4\,{\rm Z}_{\odot}$.

A survey of 31 H-poor SLSN host galaxies by Lunnan et al. (2014) consolidated the picture of H-poor SLSNe exploding in subluminous low-mass dwarf galaxies with median sSFRs of $2 \times 10^{-9}\,{\rm yr}^{-1}$. Furthermore, the preference for galaxies with a median metallicity of $Z \sim 0.5\,{\rm Z}_{\odot}$ hinted at a stifled production efficiency at high metallicity (see also Leloudas et al. 2015c). Perley et al. (2016b) confirmed this trend by modelling the MF of 18 SLSN-I hosts at $z < 0.5$ from the PTF survey (see also Chen et al. 2016). *Hubble Space Telescope* (*HST*) observations of 16 hosts of H-poor SLSNe by Lunnan et al. (2015) revealed that the locations of H-poor SLSNe are correlated with the ultraviolet (UV) light distribution within their host galaxies. Yet, they are not as strongly clustered on the UV-brightest regions of their hosts as long-duration gamma-ray bursts (GRBs; see also Angus et al. 2016; Blanchard, Berger & Fong 2016), which are also connected with the death of massive stars (e.g. Woosley 2012). Furthermore, on average, the ISM of SLSN-I host galaxies is characterized by significantly weaker absorption lines than GRBs (Vreeswijk et al. 2014).

In 2012, we initiated the SUperluminous Supernova Host galaxIES (SUSHIES) survey (Leloudas et al. 2015c) to characterize a large set of host galaxies of H-poor and H-rich SLSNe over a large redshift range. The goals of this survey are to study SLSN host galaxies in context of other SF galaxies and to place constraints on the nature of their progenitors. To achieve this, our survey has spectroscopic and imaging components to characterize the integrated host properties, such as mass, metallicity, SFR, age of the stellar populations, and dust attenuation.

In the first SUSHIES sample paper, Leloudas et al. (2015c) discussed the spectroscopic properties of 17 H-poor and 8 H-rich SLSN host galaxies. We showed that the host galaxies of H-poor SLSNe are characterized by hard ionization fields, low metallicity, and very high sSFRs. A high number (∼50 per cent) of H-poor SLSNe at $z < 0.5$ occurred in extreme emission-line galaxies (e.g. Atek et al. 2011; Amorín et al. 2014, 2015), which represent a short-lived phase in galaxy evolution following an intense starburst. Moreover, in Thöne et al. (2015), we performed spatially resolved spectroscopy of the host of PTF12dam, the most extreme host galaxy in the sample with high signal-to-noise ratio, and found strong evidence for a very young stellar population at the explosion site with an age of ∼3 Myr. These findings let us conclude in Leloudas et al. (2015c) that the progenitors of SLSNs are possibly the very first stars to explode in a starburst, at an earlier evolutionary stage than GRB progenitors. Therefore, not only metallicity but also age is likely a critical condition for the production of SLSN progenitors. Chen et al. (2016) and Perley et al. (2016b) questioned the importance of the age and proposed that metallicity is the primary factor for SLSN-I progenitors.

While H-poor SLSNe are preferentially found in rather extreme environments, the findings by Leloudas et al. (2015c) and Perley et al. (2016b) point to a weaker dependence on environment properties for H-rich SLSNe, e.g. higher average metallicities and softer ionization states.

In this second sample paper of the SUSHIES survey, we present photometric data of a sample of 53 H-poor and 16 H-rich SLSN host galaxies out to $z \sim 4$, including almost every SLSN reported in the literature and detected before 2015. The scope of this paper is to provide distribution functions of physical properties, such as luminosities, masses of the stellar populations, and SFRs, to investigate their redshift evolution and to compare these results to other samples of starburst galaxies.

Throughout the paper, we adopt a flat Λcold dark matter cosmology with $\Omega_\mathrm{m} = 0.315$, $\Omega_\Lambda = 0.685$, and $H_0 = 67.3$ km s^{-1} Mpc^{-1} (Planck Collaboration XVI 2014). Uncertainties and dispersions are quoted at 1σ confidence. We refer to the solar abundance compiled in Asplund et al. (2009).

2 SAMPLE DEFINITION, OBSERVATIONS AND DATA REDUCTION

2.1 Sample definition

Among all SLSNe reported in the literature (∼120), we selected those that were discovered before the end of 2014 and announced before 2015 April. Therefore, many of the SLSNe published recently by Perley et al. (2016b) are not included in this paper. In addition, we screened the Asiago Supernova catalogue (Barbon et al. 2010) for objects with an absolute magnitude of significantly brighter than $M = -21$ mag and spectroscopic information. This revealed two additional H-poor SLSNe, SNe 2009de, and 2011ep (Drake et al. 2009b; Moskvitin et al. 2010; Graham et al. 2011a), and two H-rich SLSNe, SNe 2009nm, and SN2011cp (Drake et al. 2009c; Christensen et al. 2009; Drake et al. 2011c,d; Graham et al. 2011b). The SN properties are summarized in Table 1.

Our final sample comprises of 53 H-poor and 16 H-rich SLSNe. The H-poor sample includes seven slow-declining H-poor SLSNe, while the H-rich sample includes the SLSNe-II CSS121015, SN2008es, and SN2013hx. The size of the final sample is not only a factor of >2 larger than the SLSN host sample presented in Perley et al. (2016b) but includes a large population of hosts at $z > 0.5$ (which is the highest redshift in Perley et al. 2016b). Fig. 1 displays the redshift distribution of our sample. It covers a redshift interval from $z \sim 0.1$ to 2 with a singular object at $z \sim 4$ (SN1000+0216; Cooke et al. 2012). The redshift distribution of the H-poor sample covers the full range and has a median of $\tilde{z} = 0.46$. The H-rich sample only extends to $z \sim 0.4$ and has a median of $\tilde{z} = 0.21$.

2.2 Observations

A fundamental goal of our survey is to secure multiband data from the rest-frame UV to near-infrared (NIR), to model the spectral energy distributions (SEDs) of the host galaxies. To ensure a sufficient wavelength coverage and data quality, we aimed to have at least one observation of the rest-frame UV and of the NIR and two observations of the rest-frame optical, if a galaxy was brighter than $r' = 24$ mag.

To optimize the observing campaign, we queried the VIZIER data base (Ochsenbein, Bauer & Marcout 2000) and public archives for available catalogues and data, such as the European Southern Observatory (ESO), Gemini, and Subaru archives. Our primary source catalogues are from the Canada–France–Hawaii Telescope Legacy Survey (CFHTLS; Hudelot et al. 2012), the Cosmological Evolution Survey (COSMOS; Scoville et al. 2007), the *Galaxy Evolution Explorer* (*GALEX*; Martin et al. 2005), the Sloan Digital Sky Survey (SDSS; York et al. 2000), the UKIRT Infrared Deep Sky Survey (Lawrence et al. 2007), and the *Wide-field Infrared Survey Explorer* (*WISE*; Wright et al. 2010).[1] These catalogues were complemented by the Coma Cluster catalogue (Adami et al. 2006), the UltraVISTA catalogue (McCracken et al. 2012), the VISTA Deep Extragalactic Observations survey (Jarvis et al. 2013), and the VIRMOS deep imaging survey (Le Fèvre et al. 2004). Furthermore, we incorporated measurements previously reported in Inserra et al. (2013), Lunnan et al. (2014), Nicholl et al. (2014), Vreeswijk et al. (2014), and Angus et al. (2016).

Between 2012 and 2016, we used observing proposals at the 6.5-m Magellan/Baade Telescope (PI: Schulze, Kim),[2] the ESO's 8.2-m Very Large Telescope (VLT) (PI: Leloudas, Krühler),[3] the 10.4-m Gran Telescopio Canarias (GTC) and 3.5-m Centro Astronómico Hispano Alemán (CAHA) telescope (PI: Gorosabel), and the 0.3-m UV/Optical Telescope (UVOT; Roming et al. 2005) onboard the *Swift* satellite (Gehrels et al. 2004, PI: Leloudas) to obtain rest-frame UV, optical, and NIR data. In the subsequent sections, we briefly summarize each campaign.

Our Magellan campaign was performed between 2012 and 2016 with the 6.5-m Baade telescope equipped with the optical wide-field Inamori-Magellan Areal Camera and Spectrograph (IMACS; Dressler et al. 2011), the Parallel Imager for Southern Cosmological Observations (PISCO; Stalder et al. 2014), and the NIR camera FourStar (Persson et al. 2013). The optical data were secured in $g'r'i'z'$, primarily with the IMACS *f*/2 camera, but also with the IMACS *f*/4 camera and PISCO. The NIR observations were performed in J and K_s.

The ESO VLT observations were taken in visitor and service modes. The visitor run took place between 2013 May 29 and June 2. We used the FOcal Reducer and Spectrograph 2 instrument (FORS2; Appenzeller et al. 1998), equipped with the red-sensitive CCD to secure data in *uBgVRIz*. In addition, we obtained *J*- and *K*-band imaging with the High Acuity Wide field K-band Imager (HAWK-I; Pirard et al. 2004; Casali et al. 2006; Kissler-Patig et al. 2008). Additional optical and NIR data were obtained with FORS2, the Infrared Spectrometer And Array Camera (ISAAC; Moorwood et al. 1998) and HAWK-I in queue mode.

The CAHA and GTC campaigns primarily focused on targets on the Northern hemisphere. The CAHA observing programme was carried out with the four-channel Bonn University Simultaneous CAmera (Reif et al. 1999) in $u'g'r'i'$ at the 3.5-m CAHA telescope in 2012. We also used the infrared wide-field camera Omega2000 (Kovács et al. 2004) to secure *J*- and *K*-band observations between 2013 and 2015 and also in *Y* and *H* band for a few targets. The objective of the campaign at the 10.4-m GTC telescope was to secure deep imaging of SNe 2008es and 2009jh with the Optical System for Imaging and low-Intermediate-Resolution Integrated Spectroscopy (OSIRIS; Cepa et al. 2000) camera.

Rest-frame UV data are critical to break degeneracies in the SED modelling. For objects at $z < 0.4$, observations in *U* or bluer filters are needed to probe the UV. *GALEX* provided critical rest-frame UV data for most objects. In addition, we secured UV photometry of five fields with the UV/optical telescope UVOT on board the *Swift*

---

[1] We included *WISE* data of only a few hosts.

[2] Programme IDs: CN2013A-195, CN2013B-70, CN2014A-114, CN2014B-127, CN2014B-102, CN-2015A-129, CN2015A-143, CN-2015B-87, CN2015B-99, CN2016A-108, and CN2016B-98.

[3] Programme IDs: 089.D-0902, 091.A-0703, 091.D-0734, and 290.D-5139.

Table 1. Properties of the SLSNe in our sample.

Object	RA (J2000)	Dec. (J2000)	Redshift	Type	$E(B-V)_{\mathrm{MW}}$ (mag)	Decline time scale τ_{dec} (d)	Reference
			Spectroscopic sample (23)				
PS1-10bzj	03:31:39.83	−27:47:42.2	0.649	SLSN-I	0.01	37.3(fast)	[1, 2]
PS1-11ap	10:48:27.73	+57:09:09.2	0.524	SLSN-I	0.01	87.9 (slow)	[2, 3]
PTF09cnd	16:12:08.94	+51:29:16.1	0.258	SLSN-I	0.02	75.3 (slow)	[2, 4]
PTF10heh	12:48:52.04	+13:26:24.5	0.338	SLSN-IIn	0.02	–	[5]
PTF10hgi	16:37:47.04	+06:12:32.3	0.099	SLSN-I	0.07	35.6 (fast)	[2, 6, 7]
PTF10qaf	23:35:42.89	+10:46:32.9	0.284	SLSN-IIn	0.07	–	[8]
PTF10vqv	03:03:06.84	−01:32:34.9	0.452	SLSN-I	0.06	–	[9]
PTF11dsf	16:11:33.55	+40:18:03.5	0.385	SLSN-IIn	0.01	–	[10]
PTF12dam	14:24:46.20	+46:13:48.3	0.107	SLSN-I	0.01	72.5 (slow)	[2, 11]
SN1999as	09:16:30.86	+13:39:02.2	0.127	SLSN-I	0.03	–	[8, 12]
SN1999bd	09:30:29.17	+16:26:07.8	0.151	SLSN-IIn	0.03	–	[8, 13]
SN2006oz	22:08:53.56	+00:53:50.4	0.396	SLSN-I	0.04	–	[14]
SN2006tf^{a}	12:46:15.82	+11:25:56.3	0.074	SLSN-IIn	0.02	–	[15]
SN2007bi^{b}	13:19:20.00	+08:55:44.0	0.128	SLSN-I	0.02	84.5 (slow)	[2, 16, 17]
SN2008am	12:28:36.25	+15:35:49.1	0.233	SLSN-IIn	0.02	–	[18]
SN2009jh^{c}	14:49:10.08	+29:25:11.4	0.349	SLSN-I	0.01	60.6 (slow)	[2, 4]
SN2010gx^{d}	11:25:46.71	−08:49:41.4	0.230	SLSN-I	0.03	29.1 (fast)	[2, 4, 19]
SN2010kd	12:08:01.11	+49:13:31.1	0.101	SLSN-I	0.03	–	[20, 21]
SN2011ke^{e}	13:50:57.77	+26:16:42.8	0.143	SLSN-I	0.01	25.7 (fast)	[2, 6]
SN2011kf^{f}	14:36:57.53	+16:30:56.6	0.245	SLSN-I	0.02	28.5 (fast)	[2, 6]
SN2012il^{g}	09:46:12.91	+19:50:28.7	0.175	SLSN-I	0.02	23.2 (fast)	[2, 6]
SNLS06D4eu	22:15:54.29	−18:10:45.6	1.588	SLSN-I	0.02	–	[22]
SSS120810^{h}	23:18:01.82	−56:09:25.7	0.156	SLSN-I	0.02	30.2 (fast)	[2, 23]
			Non-spectroscopic sample (46)				
CSS100217^{i}	10:29:12.56	+40:42:20.0	0.147	SLSN-IIn	0.01	–	[24]
CSS121015^{j}	00:42:44.34	+13:28:26.5	0.286	SLSN-II	0.07	37.8 (fast)	[2, 25]
CSS140925^{k}	00:58:54.11	+18:13:22.2	0.460	SLSN-I	0.06	–	[26]
DES14S2qri	02:43:32.14	−01:07:34.2	1.500	SLSN-I	0.03	–	[27]
DES14X2byo	02:23:46.93	−06:08:12.3	0.869	SLSN-I	0.03	–	[28]
DES14X3taz	02:28:04.46	−04:05:12.7	0.608	SLSN-I	0.02	–	[29]
iPTF13ajg	16:39:03.95	+37:01:38.4	0.740	SLSN-I	0.01	62.0 (slow)	[2, 30]
LSQ12dlf^{l}	01:50:29.80	−21:48:45.4	0.255	SLSN-I	0.01	35.4 (fast)	[2, 23]
LSQ14an	12:53:47.83	−29:31:27.2	0.163	SLSN-I	0.07	–	[31]
LSQ14mo	10:22:41.53	−16:55:14.4	0.2561	SLSN-I	0.06	27.3 (fast)	[2, 32]
LSQ14bdq	10:01:41.60	−12:22:13.4	0.345	SLSN-I	0.06	71.2 (slow)	[2, 33]
LSQ14fxj	02:39:12.61	+03:19:29.6	0.360	SLSN-I	0.03	–	[34]
MLS121104^{m}	02:16:42.51	+20:40:08.5	0.303	SLSN-I	0.15	–	[35, 36]
PS1-10ky	22:13:37.85	+01:14:23.6	0.956	SLSN-I	0.03	32.5 (fast)	[2, 37]
PS1-10pm	12:12:42.20	+46:59:29.5	1.206	SLSN-I	0.02	–	[38]
PS1-10ahf	23:32:28.30	−00:21:43.6	1.100	SLSN-I	0.03	–	[38]
PS1-10awh	22:14:29.83	−00:04:03.6	0.909	SLSN-I	0.07	–	[37]
PS1-11tt	16:12:45.78	+54:04:17.0	1.283	SLSN-I	0.01	–	[39]
PS1-11afv	12:15:37.77	+48:10:48.6	1.407	SLSN-I	0.01	–	[39]
PS1-11aib	22:18:12.22	+01:33:32.0	0.997	SLSN-I	0.04	–	[39]
PS1-11bam	08:41:14.19	+44:01:57.0	1.565	SLSN-I	0.02	–	[40]
PS1-11bdn	02:25:46.29	−05:06:56.6	0.738	SLSN-I	0.02	–	[39]
PS1-12zn	09:59:49.62	+02:51:31.9	0.674	SLSN-I	0.02	–	[39]
PS1-12bmy	03:34:13.12	−26:31:17.2	1.566	SLSN-I	0.01	–	[39]
PS1-12bqf	02:24:54.62	−04:50:22.7	0.522	SLSN-I	0.02	–	[39]
PS1-13gt	12:18:02.03	+47:34:46.0	0.884	SLSN-I	0.02	–	[39]
PTF09atu	16:30:24.55	+23:38:25.0	0.501	SLSN-I	0.04	–	[4]
PTF11rks	01:39:45.51	+29:55:27.0	0.190	SLSN-I	0.04	22.3 (fast)	[2, 6, 41]
SCP06F6	14:32:27.40	+33:32:24.8	1.189	SLSN-I	0.01	39.8 (fast)	[2, 42]
SN2003ma	05:31:01.88	−70:04:15.9	0.289	SLSN-IIn	0.31	–	[43]
SN2005ap	13:01:14.83	+27:43:32.3	0.283	SLSN-I	0.01	28.8 (fast)	[2, 44]
SN2006gy	03:17:27.06	+41:24:19.5	0.019	SLSN-IIn	0.14	–	[45]
SN2007bw^{n}	17:11:01.99	+24:30:36.4	0.140	SLSN-IIn	0.04	–	[46]
SN2008es^{o}	11:56:49.13	+54:27:25.7	0.205	SLSN-II	0.01	38.0 (fast)	[2, 47, 48]
SN2008fz^{p}	23:16:16.60	+11:42:47.5	0.133	SLSN-IIn	0.04	–	[49]
SN2009de^{q}	13:00:37.49	+17:50:57.0	0.311	SLSN-I	0.04	–	[50, 51, 52]
SN2009nm^{r}	10:05:24.54	+51:16:38.7	0.210	SLSN-IIn	0.01	–	[53, 54]

Table 1 – *continued*

Object	RA (J2000)	Dec. (J2000)	Redshift	Type	$E(B-V)$ (mag)	Decline time $\tau_{\rm dec}$ (days)	Reference
SN2011cp^{s}	07:52:32.61	+21:53:29.7	0.380	SLSN-IIn	0.05	–	[55]
SN2011ep^{t}	17:03:41.78	+32:45:52.6	0.280	SLSN-I	0.02	–	[56]
SN2013dg^{u}	13:18:41.38	−07:04:43.1	0.265	SLSN-I	0.04	30.7 (fast)	[2, 23]
SN2013hx^{v}	01:35:32.83	−57:57:50.6	0.130	SLSN-II	0.02	33.6 (fast)	[2, 57]
SN2013hy^{w}	02:42:32.82	−01:21:30.1	0.663	SLSN-I	0.03	–	[58]
SN2015bn^{x}	11:33:41.57	+00:43:32.2	0.110	SLSN-I	0.02	–	[59]
SN1000+0216^{y}	10:00:05.87	+02:16:23.6	3.899	SLSN-I	0.02	–	[60]
SN2213−1745^{y}	22:13.39.97	−17:45:24.5	2.046	SLSN-I	0.02	–	[60]
SNLS07D2bv	10:00:06.62	+02:38:35.8	∼1.5	SLSN-I	0.02	–	[22]

Notes. The coordinates refer to the positions of the SNe. The Galactic extinction measurements are taken from Schlafly & Finkbeiner (2011). We divide the sample into the spectroscopic sample (23 objects) presented in Leloudas et al. (2015c) and in a non-spectroscopic sample (46 objects). The decay-time-scale $\tau_{\rm dec}$ is defined as the time when the luminosity of the pseudo-bolometric $g'r'i'z'$ light curve dropped to $L_{\rm max}/e$. We divide the sample into fast and slow decliners if $\tau_{\rm dec} < 50$ and >50 d, respectively.

Alternative SN names: ^{a}CSS070320:124616+112555; ^{b}SNF20070406-008; ^{c}CSS090802:144910+292510, PTF09cwl; ^{d}CSS100313:112547-084941, PTF10cwr; ^{e}CSS110406:135058+261642, PTF11dij, PS1-11xk; ^{f}CSS111230:143658+163057; ^{g}CSS120121:094613+195028, PS1-12fo; ^{h}SSS120810:231802-560926; ^{i}CSS100217:102913+404220; ^{j}CSS121015:004244+132827; ^{k}CSS140925:005854+181322; ^{l}SSS120907:015030-214847; ^{m}MLS121104:021643+204009, LSQ12fzb; ^{n}SNF20070418-020; ^{o}ROTSE3 J115649.1+542725; ^{p}CSS080922:231617+114248; ^{q}CSS090102:130037+175057, PSN K0901-1; ^{r}CSS091120:100525+511639; ^{s}MLS110426:075233+215330, PSN J07523261+2153297; ^{t}CSS110414:170342+324553; ^{u}CSS130530:131841-070443, MLS130517:131841-070443; ^{v}SMT J013533283-5757506; ^{w}DES13S2cmm; ^{x}CSS141223:113342+004332, MLS150211:113342+004333, PS15ae; ^{y}The classifications of SN1000+0213 and SN2213−1745 are based on photometry. The light curve of SN1000+0213 shows a bump before the main emission similar to H-poor SLSNe SN2006oz and LSQ14bdq (for details see Leloudas et al. 2012; Nicholl et al. 2015a).

References. – [1] Lunnan et al. (2013); [2] Nicholl et al. (2015a); [3] McCrum et al. (2014); [4] Quimby et al. (2011c); [5] Quimby et al. (2010a); [6] Inserra et al. (2013); [7] Leloudas et al. (2015c); [8] Gal-Yam (2012); [9] Quimby et al. (2010b); [10] Quimby et al. (2011a); [11] Nicholl et al. (2013); [12] Knop et al. (1999); [13] Nugent et al. (1999); [14] Leloudas et al. (2012); [15] Smith et al. (2008); [16] Gal-Yam et al. (2009); [17] Young et al. (2010); [18] Chatzopoulos et al. (2011); [19] Pastorello et al. (2010); [20] Vinko et al. (2012); [21] Quimby et al. (2013b); [22] Howell et al. (2013); [23] Nicholl et al. (2014); [24] Drake et al. (2011a); [25] Benetti et al. (2014); [26] Campbell et al. (2014); [27] Castander et al. (2015); [28] Graham et al. (2014); [29] Smith et al. (2016); [30] Vreeswijk et al. (2014); [31] Leget et al. (2014); [32] Leloudas et al. (2015b); [33] Nicholl et al. (2015b); [34] Smith et al. (2014); [35] Drake et al. (2012); [36] Fatkhullin & Gabdeev (2012); [37] Chomiuk et al. (2011); [38] McCrum et al. (2015); [39] Lunnan et al. (2014); [40] Berger et al. (2012); [41] Quimby et al. (2011b); [42] Barbary et al. (2009); [43] Rest et al. (2011); [44] Quimby et al. (2007); [45] Smith et al. (2007); [46] Agnoletto (2010); [47] Gezari et al. (2009); [48] Miller et al. (2009); [49] Drake et al. (2010); [50] Drake et al. (2009b); [51] Drake et al. (2009a); [52] Moskvitin et al. (2010); [53] Drake et al. (2009c); [54] Christensen et al. (2009); [55] Drake et al. (2011b); [56] Graham et al. (2011a); [57] Inserra et al. (2016); [58] Papadopoulos et al. (2015); [59] Nicholl et al. (2016) [60] Cooke et al. (2012).

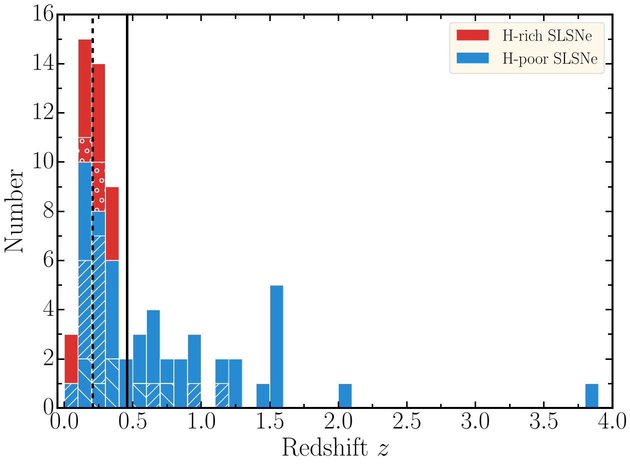

Figure 1. The redshift distribution of the SUSHIES survey. For 21 H-poor SLSNe, information about the decline time-scale are available. The region hatched by '//' displays the redshift distribution of the fast decliners and the region highlighted by '\\' signifies the redshift distribution of the slow decliners. The redshift distribution of the three SLSNe-II, CSS121015, SN2008es, and SN2013hx, are highlighted by 'o'. The median redshifts of the H-poor and H-rich sample are $\tilde{z} = 0.46$ (solid vertical line) and $\tilde{z} = 0.21$ (dashed vertical line), respectively.

satellite in 2014 and incorporated archival UVOT data of a further SLSN.

These core observing campaigns were complemented by smaller observing programmes that targeted selected host galaxies. We observed the field of SN2005ap with the Andalucia Faint Object Spectrograph and Camera (ALFOSC) at the 2.54-m Nordic Optical Telescope and the field of SN2007bi with ALFOSC and the seven-channel imager Gamma-Ray Burst Optical/Near-Infrared Detector (GROND; Greiner et al. 2008) at the 2.2-m Max-Planck-Gesellschaft telescope.

To place limits on the total SFR, we used 1.4 GHz data from the Very Large Array (VLA) Faint Images of the Radio Sky at Twenty-Centimetres survey (FIRST; Becker, White & Helfand 1995), the National Radio Astronomy Observatory (NRAO) VLA Sky Survey (NVSS, $\nu = 1.4$ GHz; Condon et al. 1998), and 843 MHz data from the Sydney University Molonglo Sky Survey (SUMSS; Bock, Large & Sadler 1999). In addition, we secured continuum observations of MLS121104, SN2005ap, and SN2008fz with the Karl Jansky Very Large Array (JVLA; PI: Ibar).[4] The continuum observations were performed in L band in the most extended A-configuration in 2015 July and September. The frequency was centred at 1.5 GHz with a total synthesized bandwidth of 1 GHz. We used the standard flux and bandwidth calibrator 3C48 for all

---

[4] Programme ID: 15A-224

the sources except SN2005ap, for which we used 3C286 instead. For phase calibration purposes, we used bright nearby point-like sources from the VLA calibrator list (MLS121104: J0238+1636; SN2005ap: J1310+3220; and SN2008fz: J2330+1100). The key properties of each observation is reported in Table A1.

2.3 Data reduction

We reduced all data in a consistent way with standard routines in IRAF (Tody 1986). The typical steps are (i) bias/overscan subtraction, (ii) flat-fielding, (iii) fringe correction, (iv) stacking of individual images, and (v) astrometric calibration. For a few instruments, we used instrument specific software packages: the GEMINI IRAF package, the GROND pipeline (Yoldaş et al. 2008; Krühler et al. 2008), PHOTPIPE for PISCO data (Bleem et al. 2015), SDFRED1 and SDFRED2 for Subaru Suprime-Cam data (Yagi et al. 2002; Ouchi et al. 2004), THELI version 2.10.0 (Erben et al. 2005; Schirmer 2013) for the FourStar data, VLT instrument pipelines for HAWK-I (version 1.8.18), and ISAAC (version 6.1.3) data,[5] and a customized pipeline for the Magellan/IMACS data. The world-coordinate systems were calibrated with ASTROMETRY.NET version 0.5 (Lang et al. 2010).

UVOT data were retrieved from the *Swift* Data Archive.[6] We used the standard UVOT data analysis software distributed with HEASOFT version 6.12, along with the standard calibration data.[7]

The JVLA data were reduced using the Common Astronomy Software Applications package (McMullin et al. 2007) and consisted of careful data flagging and standard flux, bandwidth, and phase calibration. No self-calibration was performed to the data. The obtained flux density root mean squares (rms) of the images are summarized in Table A2.

3 METHODS

3.1 Host identification

We aligned our host-only images with the original SN images that we retrieved from archives with GAIA version 4.4.6.[8] The average alignment accuracy was ~0.17 arcsec. We neither found (suitable) public data for 13 SNe from PanSTARSS, nor for SNe 2006tf, 2009de, 2009nm, and 2011cp (in total 17/69 objects). For those objects, we relied on the reported SN positions. Although this added an uncertainty to the host identification, the SN positions always coincided with a galaxy, which we assume is the host galaxy.

3.2 Photometry

We developed a PYTHON programme that is based on SOURCE EXTRACTOR version 2.19.5 (Bertin & Arnouts 1996) to perform seeing matched aperture photometry. To measure the total flux of the given object, the source radius was typically 2–4 times the full-width at half-maximum (FWHM) of the stellar point spread function (PSF). In case another object was close to the SN position or if the host had a large angular diameter, we adjusted the extraction radius accordingly. If a host evaded detection in all bands, we measured the flux and its uncertainty at the SN position using an aperture with a radius of 4 × FWHM. Those measurements have very large uncertainties, but they can be easily included in the SED modelling in contrast to upper limits.

Once an instrumental magnitude was established, it was photometrically calibrated against the brightness of several standard stars measured in a similar manner or tied to the SDSS DR8 (Aihara et al. 2011) and the AAVSO (American Association of Variable Star Observers) Photometric All-Sky Survey DR9 (Henden et al. 2016) catalogues. For Bessell/Johnson/Cousins filters, we converted the photometry of stars in the SDSS catalogue from SDSS using the Lupton colour equations.[9] In the NIR (JHK_s), the photometry was tied to Two Micron All Sky Survey (2MASS). The UVOT photometry was performed with the programme UVOTSOURCE. UVOT zero-points are defined for an aperture with a diameter of 5 arcsec. We translated these zero-points into those of our requested apertures by applying simple aperture correction methods for stars.

Finally, the measurements were corrected for Galactic extinction using the extinction maps by Schlafly & Finkbeiner (2011) and transformed into the AB system using Blanton & Roweis (2007) and Breeveld et al. (2011).

In total, we measured the brightness (and limits for the non-detections) of 53 of the 69 objects, which also includes the re-evaluation of 27 individual data sets from 2MASS, CFHTLS, and SDSS, as well as several archival data sets. In addition, we augmented the photometry of 31 objects by literature values, such as *GALEX*, Pan-STARRS, and *WISE* data. Owing to *GALEX*'s and *WISE*'s large PSFs, we only included their photometry if a contamination by neighbouring objects could be excluded. Among the 16 objects whose photometry is entirely based on literature results, four galaxies are in the footprint of the COSMOS survey: PS1-12zn, PS1-12bqf, SN1000+0213, and SNLS07D2bv. Their photometry is discussed here for the first time. Table A1 summarizes the photometry of each object.

3.3 Spectral energy distribution fitting

We modelled the SEDs with LEPHARE (Arnouts et al. 1999; Ilbert et al. 2006),[10] using a grid of galaxy templates based on Bruzual & Charlot (2003) stellar population-synthesis models with a Chabrier initial mass function (IMF, Chabrier 2003). The star formation history (SFH) was approximated by a declining exponential function of the form $\exp{(-t/\tau)}$, where t is the age of the stellar population and τ the e-folding time-scale of the SFH (varied in eight steps between 0.1 and 15 Gyr). Furthermore, we assumed the Calzetti dust attenuation curve (Calzetti et al. 2000). For a description of the galaxy templates, physical parameters of the galaxy fitting, and their error estimation, we refer to Krühler et al. (2011).[11]

As an extension to Krühler et al. (2011), we relaxed the analysis threshold of the galaxy mass to $10^4\,\mathrm{M}_\odot$ (which is pushing the definition of a galaxy), because previous studies showed that SLSNe can occur in very low-mass galaxies (Lunnan et al. 2014; Leloudas et al. 2015c; Angus et al. 2016). We modified the gas component in LEPHARE by incorporating the observed relationship between line flux and SFR for [O II] and [O III] by Krühler et al. (2015). The attenuation of the ionized gas component was linked to the stellar attenuation via $E(B-V)_{\rm star} = 0.44 \times E(B-V)_{\rm gas}$ by Calzetti et al. (2000). All

---

[5] http://www.eso.org/sci/software/cpl/esorex.html

[6] http://www.swift.ac.uk/swift_portal/

[7] http://heasarc.nasa.gov/lheasoft/

[8] http://starlink.eao.hawaii.edu/starlink/2015ADownload

[9] http://www.sdss.org/dr5/algorithms/sdssUBVRITransform.html

[10] http://www.cfht.hawaii.edu/~arnouts/LEPHARE

[11] The templates used in this paper do not account for possible binary star evolution, which could substantially alter SEDs (more hard UV photons; e.g. Stanway, Eldridge & Becker 2016).

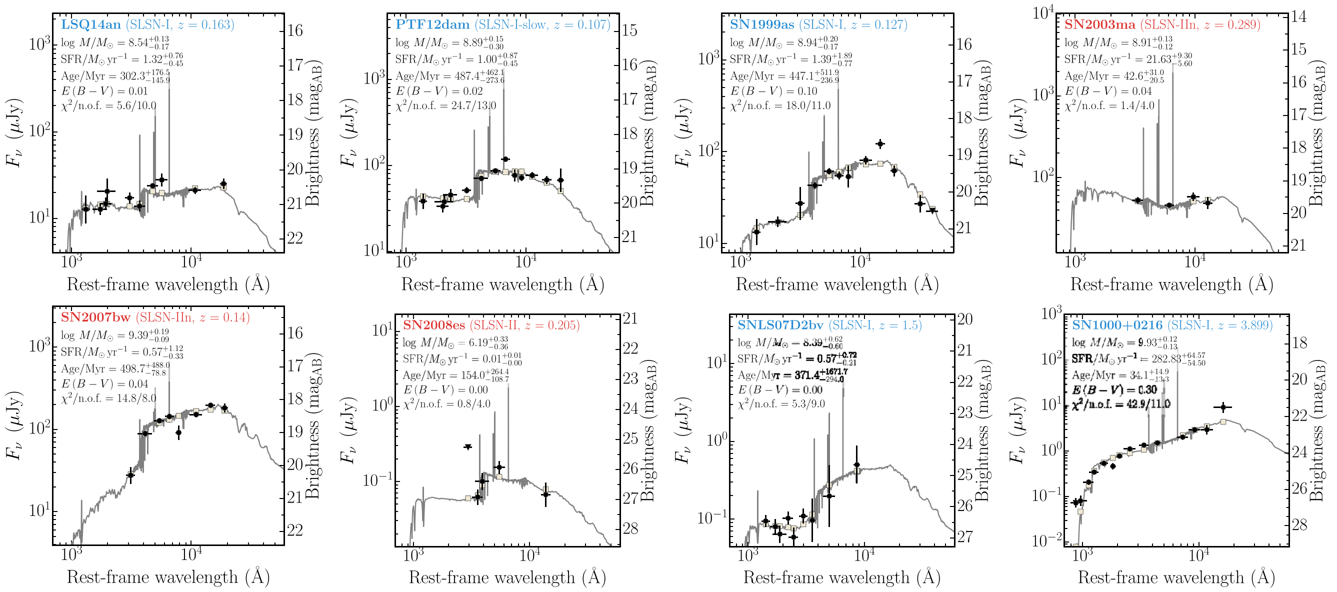

Figure 2. Selection of SEDs of hosts of H-poor and H-rich SLSNe from 700 to 60 000 Å (detections: ●; upper limits: ▼). The solid line displays the best-fitting model of the SED. The squares in a lighter shade are the model predicted magnitudes. The fitting parameters are displayed for each SED. See Table 4 and Section 3.3 for details. The full collection of SEDs are shown in Figs B1 and B2.

attenuation measurements are reported for $E(B-V)_{\rm gas}$. Finally, we used the high-resolution BC03 templates, which are defined over 6900 wavelength points instead of 1221 wavelength points from 9.1×10^{-3} to 160 μm. To account for zero-point offsets in the cross-calibration and absolute flux scale, we added a systematic error of 0.05 mag in quadrature to the uncertainty introduced by photon noise. For *GALEX*, UVOT, and *K*-band data, this systematic error was increased to 0.1 mag.

The absolute magnitudes were computed directly by convolving the filter response functions with the best-fitting template. To compute the corresponding error $\sigma(M_{\rm Q})$ in the rest-frame bandpass Q, we interpolated between the errors of the apparent magnitudes $\sigma(m_{\rm k})$ and $\sigma(m_{\rm l})$ of the observed bandpass k and l, respectively, via:

$$\sigma\left(M_{\rm Q}\right)=\frac{\sigma\left(m_{\rm k}\right)-\sigma\left(m_{\rm l}\right)}{\lambda_{\rm rest,k}-\lambda_{\rm rest,l}}\left(\lambda_{\rm rest,Q}-\lambda_{\rm rest,l}\right)+\sigma\left(m_{\rm l}\right)$$

where $\lambda_{\rm rest,k/l}=\lambda_{\rm obs,k/l}/(1+z)$ is the central wavelength of the observer-frame bandpass k and l in the rest frame of the SLSNe. In the case, a rest-frame bandpass lies blueward/redward of the observation in the bluest/reddest filter, we set the error $\sigma(M_{\rm Q})$ to the error of the observation in the bluest/reddest filter.

Our observations were characterized by a large set of different filters, of which several have similar bandpasses. To simplify the fitting, we homogenized the filter set. Specifically, we set the filter response function of $F336W$, $u_{\rm PS1}$, u^*, uvu to u', $F475$, $g_{\rm DES}$, $g_{\rm High}$, $g_{\rm PS1}$, $g+$ to g', $r_{\rm DES}$, $r_{\rm PS1}$, $r+$ to r', $F775W$, $i_{\rm DES}$, $i_{\rm PS1}$, $i+$ to i'', $F850LP$, $z_{\rm DES}$, $z_{\rm Gunn}$, $z_{\rm PS1}$, z^+ to z', $F390W$ $U38$ to U, Bj to B, Vj to V, I_c, $F814W$ to I, $y_{\rm PS1}$ to Y, $F160W$ to H, $W1$ to *Spitzer*/3.6 μm, and $W2$ to *Spitzer*/4.5 μm. It can be seen from our fits (Figs 2, B1, and B2), and quality of the derived host properties (Table 4), that the impact of these assumptions is negligible.

Studies of SLSN host galaxies and extreme emission-line galaxies (e.g. Amorín et al. 2015) showed that emission lines can significantly affect the SED fitting. To quantify this effect, we repeated the SED fitting for our spectroscopic sample (Leloudas et al. 2015c; Table 1). The contribution of the emission line i on the photometry in filter j is given by

$$\begin{aligned}\Delta m_{\rm i,j} &= -2.5\,\log\left(\frac{f_{\lambda,{\rm c}}\left(\lambda\right)+f^{i}_{\lambda,{\rm l}}\left(\lambda\right)}{f_{\lambda,{\rm c}}\left(\lambda\right)}\right)\\ &= -2.5\,\log\left(1+\frac{\int {\rm d}\lambda\; f^{i}_{\lambda,{\rm l}}\left(\lambda\right)\;T_{\rm j}\left(\lambda\right)}{\int {\rm d}\lambda\; f_{\lambda,{\rm c}}\left(\lambda\right)\;T_{\rm j}\left(\lambda\right)}\right)\end{aligned}$$

where $f^{i}_{\lambda,{\rm l}}$ is the flux density of the emission line i, $f_{\lambda,{\rm c}}$ is the flux density of the stellar continuum, and $T_{\rm j}(\lambda)$ is the transmission function of the filter j. The strength of an emission line can be characterized by its equivalent width (EW), hence $f^{i}_{\lambda,{\rm l}}=f_{\lambda,{\rm c}}\times{\rm EW}_{\rm i}$. Assuming that all emission lines are narrow compared to the width of the broad-band filter, the above expression simplifies to

$$\Delta m_{\rm i,j}=-2.5\,\times\,\log\left(1+\frac{{\rm EW}_{\rm i}\,T_{\rm j}\left(\lambda_{\rm i}\right)}{\Delta\lambda_{\rm j,eff}}\right)$$

where $T_{\rm j}(\lambda_{\rm i})$ is the filter response function of filter j at the wavelength of the emission line i (in the air reference frame) and $\Delta\lambda_{\rm j,eff}$ is the effective width of the filter. In contrast to the SED fitting, it was necessary to use the exact filter transmission function of each instrument.

We subtracted the contribution of H α–H δ, [O II], [O III], [N II], [Ne II], and [S II] from the measured brightness in the broad-band filter. Afterwards, we explicitly switched off the contribution from the ionized gas of H II regions in LEPHARE and repeated the fits with the emission-line-subtracted SEDs. The result of this experiment is discussed in Section 4.1.2.

3.4 Ensemble statistics

To compare observed distributions with distributions of other galaxy samples (parent distributions), such as extreme emission-line galaxies (hereafter EELGs), GRBs, and SNe, we performed an Monte-Carlo (MC) simulation as follows. Each SLSN host measurement was represented by a normal distribution centred at the observed value and with a width (1σ) determined from the asymmetric error or a uniform distribution between the upper limit and the smallest/faintest value in the sample for those objects with upper limits only. A two-sided Anderson–Darling (AD) test was performed between the resampled distributions and the parent distributions, using the R package KSAMPLES. This process was repeated 10 000 times and a mean AD value obtained. We rejected the null hypothesis of two distributions being drawn from the same parent distribution if the corresponding chance probability $p_{\rm ch}$ was smaller than 0.01.

To complement the 1D AD tests, we also performed 2D tests in the mass–SFR plane. We first computed the mean mass and SFR of the SLSN-host sample. After that, we bootstrapped 10 000 samples of size N from the other galaxy samples, where N is the number of SLSNe in the given redshift interval, and computed the mean mass and SFR of each bootstrapped sample. Measurement errors were propagated through an MC simulation as described above. Finally, we computed the region that contained 99 per cent of all realizations using the PYTHON package CORNER.PY (Foreman-Mackey 2016). If the estimator of the SLSN sample did not fall in that region, the chance probability $p_{\rm ch}$ is less than 0.01 and we rejected the null hypothesis of both distributions being statistically similar.

For each statistical test, we also performed a two-sided AD test on the redshift distributions to minimize systematic errors introduced by cosmic evolution, similar to Japelj et al. (2016).

We extract robust estimates of the ensemble distribution functions with a Bayesian approach, which incorporates the varying and asymmetric measurement uncertainties of individual sources and the limited sample size. For this, we fit to the sample measurements in a quantity (e.g. in $M_\star$ or SFR) a normal distribution. We constrain its parameters, the mean μ and standard deviation σ, with a likelihood defined as the product of convolutions of that distribution and the measurement probability distributions. The fit uncertainties were obtained with the MULTINEST package (Feroz et al. 2013) through the PYTHON package PYMULTINEST (Buchner et al. 2014). Flat priors were assumed on μ and $\log \sigma$.

3.5 Comparison samples

We built several comparison samples to put SLSN host galaxies in context with the cosmic SFH and to better understand the peculiar conditions that gave rise to this class of stellar explosion.

Core-collapse supernova host galaxies: Because of the connection between SLSNe and massive stars, we compiled CCSN host galaxy samples. As in Leloudas et al. (2015c), we used SNe from untargeted (with respect to galaxies) surveys. At $z < 0.3$, we use objects studied in Leloudas et al. (2011), Sanders et al. (2012), and Stoll et al. (2013). All SNe in these samples have robust spectroscopic classifications. The combined sample consists of 44 Type Ib/c SNe and 46 Type II SNe. These studies provide multiband data, which are primarily based on SDSS photometry and also spectroscopy for a number of hosts. We adopt the SED modelling by Leloudas et al. (2015c) for the Leloudas et al. (2011) and Sanders et al. (2012) samples. Note, the SEDs in Stoll et al. (2013) were modelled with the FAST stellar population synthesis code (Kriek et al. 2009) with the Bruzual & Charlot (2003) templates and a Salpeter IMF. We reduced their SFRs and galaxy masses by a factor of 1.8, to convert from a Salpeter to a Chabrier IMF, used in this paper (Kennicutt 1998).

To expand the SN sample to redshifts larger than $z > 0.3$, where most of our SLSNe are found, we added the SN sample from the Great Observatories Origins Deep Survey (GOODS) and Probing Acceleration Now with Supernovae (PANS) surveys (Riess et al. 2004). GOODS/PANS were *HST* surveys to detect Type Ia SNe at high redshift. This survey also located 58 distant CCSNe between $z = 0.28$ and 1.3 (the median being $\tilde{z} = 0.47$). In contrast to the low-z samples, their classification relied on photometric data. The method allowed a distinction between Type Ia and CCSNe, but not a categorization into subtypes. Thanks to the overlap with the GOODS field, each SN host has deep rest-frame UV to NIR data. We adopt the results of the SED modelling by Svensson et al. (2010). Note, these authors modelled the SEDs with their own software that uses observed SEDs of local galaxies and SEDs produced with various spectral synthesis codes as templates. Furthermore, they assumed a Salpeter IMF. Similar to Stoll et al. (2013), the SFRs and the masses were reduced by a factor of 1.8 to convert from a Salpeter to a Chabrier IMF.

GRB host galaxies: A member of our team (T. Krühler) collected multiband data of long GRBs. These GRBs are selected to be part of one of the following complete GRB samples: GROND 4-h sample (Greiner et al. 2011), TOUGH survey (The Optically Unbiased GRB Host Galaxy survey; Hjorth et al. 2012), BAT-6 (Salvaterra et al. 2012) or SHOALS (*Swift* Gamma-Ray Burst Host Galaxy Legacy Survey; Perley et al. 2016b). The individual measurements are reported in Krühler & Schady (2017). Among all hosts, we selected those at $z < 1$ (52 in total). At these redshifts, it is relatively easy to secure the GRB redshift, because of the sparsity of dust-obscured bursts at $z < 1$, and to build host samples with a high detection completeness. The SEDs of this sample were analysed in a similar way as our SLSN host galaxy sample.

COSMOS/UltraVISTA survey: To compare SLSN host galaxies to field galaxies, we used the ultra-deep NIR survey UltraVISTA that observed an area of 1.8 deg^2 down to $K({\rm AB})_{\rm s} = 23.9$ mag (5σ confidence). We chose the K band, i.e. mass, selected catalogue by Muzzin et al. (2013) that overlaps with the COSMOS field. This catalogue provides observations in 30 bands from rest-frame UV to NIR. Among all galaxies, we selected those at $z < 4$ with SFRs of at least 10^{-3} M$_\odot$ yr^{-1}, sSFRs between 10^{-13} and $10^{-7.5}$ yr^{-1}, and 'USE' flags equal to one. This sample comprises ∼151 000 galaxies with a median redshift of $\tilde{z} = 0.97$. Because of the small survey area, the number of hosts at $z < 0.1$ is small. This does not affect our analysis because only two SLSNe in our sample are at lower redshifts.

EELGs: Leloudas et al. (2015c) showed that H-poor SLSNe are preferentially found in EELGs. We built a master sample including results from Atek et al. (2011), Amorín et al. (2014, 2015), and Maseda et al. (2014). Those samples selected EELGs by applying different brightness cuts, colour selection criteria, spectroscopy, and redshift constraints. The total sample consists of 227 galaxies with rest-frame [O III] λ5007 EWs of >100 Å between $z = 0.11$ and 2.3. All surveys reported stellar mass and SFR for each galaxy, but other properties, such as brightness, colour or $M_{\rm B}$, were only reported for certain subsamples.

A summary of the individual surveys and which properties are used in this study is presented in Table 2.

4 RESULTS

4.1 Spectral energy distribution modelling

4.1.1 Quality of the SED modelling

We made two assumptions to model all SEDs in an automatic and self-consistent way: (i) the SEDs can be described by a stellar component with an exponentially declining SFH and a contribution

Table 2. Properties of the comparison samples and their selection criteria.

Sample	Selection criteria	Number of objects	Redshift interval	Which properties used?
CCSN host galaxies (total number 265)				
Leloudas et al. (2011) (L11)	Ib/c SNe, detected by untargeted surveys spectroscopic classification	12	$0.02 \leq z \leq 0.18$ $\tilde{z} = 0.04$	M_B, mass, SFR[a]
Sanders et al. (2012) (S12)	Ib/c SNe, detected by untargeted surveys spectroscopic classification	31	$0.01 \leq z \leq 0.26$ $\tilde{z} = 0.03$	M_B, mass, SFR[a]
Svensson et al. (2010)	GOODS SN sample photometric SN classification	165	$0.28 \leq z \leq 1.30$ $\tilde{z} = 0.47$	M_B, mass, SFR
Stoll et al. (2013) (S13)	First-year PTF CCSN sample primarily Type II SNe	58	$0.01 \leq z \leq 0.18$ $\tilde{z} = 0.04$	M_B, mass, SFR
EELGs (total number 227)				
Amorín et al. (2014)	VUDS survey (Le Fèvre et al. 2015), $23\,\mathrm{mag} < I(\mathrm{AB}) < 25\,\mathrm{mag}$	31	$0.21 \leq z \leq 0.86$ $\tilde{z} = 0.57$	Colour, m_R, M_B, mass, SFR
Amorín et al. (2015)	zCOSMOS survey, $I(\mathrm{AB}) \leq 22.5$ mag $\mathrm{EW_{rest}}$ ([O III] λ5007) > 100 Å	165	$0.11 < z < 0.92$ $\tilde{z} = 0.48$	Colour, m_R, M_B, mass, SFR
Atek et al. (2011)	WISPS survey (Atek et al. 2010), $0.5 < z < 2.3$ $\mathrm{EW_{rest}}$ ([O III] λ5007) > 200 Å	9	$0.9 \leq z \leq 2.04$ $\tilde{z} = 1.36$	Mass, SFR
Maseda et al. (2014)	3D-*HST* survey (Brammer et al. 2012), colour selection emission lines do not fall in the NIR band gaps	22	$1.3 \leq z \leq 2.3$ $\tilde{z} = 1.65$	Mass, SFR
Field galaxies (total number 150 900)				
Muzzin et al. (2013)	*K*-band selected COSMOS/UltraVISTA survey $\mathrm{SFR} > 10^{-3}\,\mathrm{M_\odot\,yr^{-1}}$, USE = 1, $z < 4$ $10^{-13}\,\mathrm{yr^{-1}} < \mathrm{sSFR} < 10^{-7.5}\,\mathrm{yr^{-1}}$	150 900	$0.01 \leq z \leq 3.96$ $\tilde{z} = 0.97$	Colour, m_R, mass, SFR
Long GRB host galaxies (total number 52)				
Krühler & Schady (2017)	$z < 1$, long-duration *Swift* GRBs detected before 2014 May, part of the GROND 4-h, TOUGH, SHOALS BAT-6 samples	52	$0.06 \leq z \leq 0.98$ $\tilde{z} = 0.67$	Colour, m_R, M_B, mass, SFR

Notes. The selection criteria consist of the criteria from each individual survey and those we imposed to build the final samples. All samples were cleaned from duplicates.

[a] We used the re-computed values in Leloudas et al. (2015c).

from the ionized gas of the H II regions and (ii) the number of filters (n.o.f.) can be reduced to the homogenized filter set in Section 3.3. Over 90 per cent of our hosts have good fits with an average χ^2/n.o.f. of 0.5 and derived physical parameters that are comparable to other galaxy samples (Table 4 and Figs 2, B1, and B2).

The fits of only six hosts had χ^2/n.o.f. between 3.9 and 10.4. The fits of PS1-11bdn and SN1000+0216 are of poorer quality (χ^2/n.o.f. = 3.9 and 6.3, respectively) caused by a few data points. The host of PS1-10bzj has very strong emission lines that fall in the wings of the i'-band transmission function, which increased the normalized χ^2 to 10.4. Apart from data points in a few individual filters, the fits are none the less very good and can be used without restriction.

The fits of CSS100217, PTF11dsf, SN1999bd, and SN2006gy have to be used with more caution. Drake et al. (2011a) revealed a narrow-line Seyfert in the host galaxy of CSS100217. Furthermore, Leloudas et al. (2015c) reported on the discovery of broad H α and [O III] in the host spectrum of PTF11dsf, which could be due to an active galactic nucleus (AGN) as well. The hosts of SLSNe-IIn SN1999bd and SN2006gy are evolved galaxies that experienced a recent starburst. This is demonstrated by the detection of Balmer lines in both spectra (Smith et al. 2007; Leloudas et al. 2015c; Fox et al. 2015), while the SED cannot be modelled by an exponentially declining SFH. A reliable modelling of the SEDs of these three hosts requires a detailed modelling of their SFHs and the inclusion of an AGN component, which is beyond the scope of this paper. Leloudas et al. (2015c) mentioned that the host of PTF11dsf could also harbour an AGN. Similar to the three aforementioned hosts, we only use the mass and the *B*-band luminosities of PTF11dsf's host in our discussion, but not the SFR.

4.1.2 *Contribution of emission lines*

Our SED modelling includes the contribution of the H II regions. This is of particular importance because previous studies showed that emission lines can significantly affect the SED fitting (e.g. Castellano et al. 2014; Lunnan et al. 2014; Chen et al. 2015; Santini et al. 2015). This motivated Lunnan et al. (2014) to omit filters that were affected by [O III] λ5007, if [O III] had a large EW, and Chen et al. (2015) to subtract the emission-line contribution from the broad-band photometry. Both approaches are strictly limited to objects with host spectroscopy.

Thanks to LEPHARE capabilities, we quantify the impact of emission lines on the SED fitting with a more sophisticated approach. First, we fit the SEDs of the spectroscopic subsample with templates that include a stellar and a gas component. Then, we subtract the contribution of the emission lines from the broad-band photometry and fit the new SEDs with a stellar component only, i.e. the gas component is explicitly switched off in LEPHARE.

Fig. 3 shows how the primary diagnostics mass and SFR change if emission lines are included in the SED fitting. The absolute value of the average mean bias deviation and the average rms error in the mass and SFR estimates are <0.06 and <0.18 dex, respectively, and smaller than the 1σ error bars of individual measurements. The most critical object in this analysis is PTF12dam,

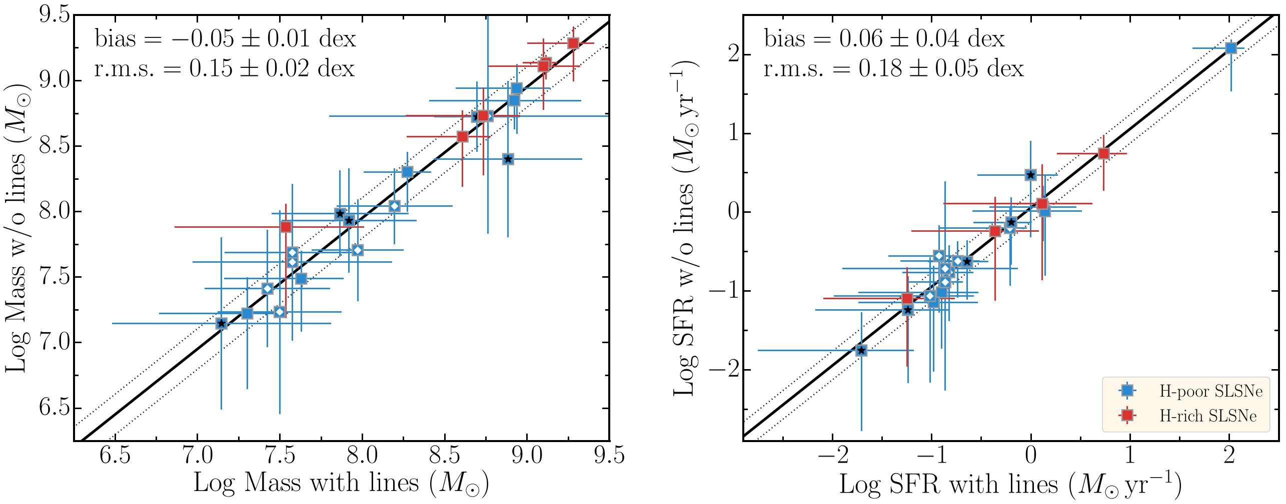

Figure 3. Derived masses (left) and SFRs (right) of galaxies from the spectroscopic subsample. The SEDs are fitted with two different procedures: i) the photometry of the galaxies with the contribution of the emission lines is fitted with galaxy templates and an emission-line component in LEPHARE; (ii) the photometry of the same galaxies is fitted after removal of the emission-line contribution and switching off the ionized gas component in LEPHARE. The values in the upper left corners report the mean bias deviations and the average root square errors (rms) between the measurements with and without emission-line contribution and their corresponding errors. The solid line indicates the bias between both diagnostics and the dotted lines the mean rms centred around the bias. The agreement is very good, showing that we can obtain reliable results with LEPHARE also for the galaxies where spectroscopic information is not available. The hosts of fast and slow-declining H-poor SLSNe are signified by '⋆' and '◇', respectively.

the most extreme SLSN host galaxy known to date. Its deviations between the mass and SFR estimates with and without lines are $\Delta\mathrm{SFR} = \log \mathrm{SFR}_{\mathrm{w/\,lines}} - \log \mathrm{SFR}_{\mathrm{w/o\,lines}} = -0.47 \pm 0.45$ dex and $\Delta M = 0.48 \pm 0.42$ dex. Apart from this object, the agreement between the two fits is excellent. This reflects the fact that we have good photometry spanning a large wavelength interval *and* a good handle on the gas emission in the SED fitting, so that the uncertainty in the emission-line contribution does not affect our results.

4.1.3 SED versus emission-line diagnostics

By combining results from the spectroscopic observations in Leloudas et al. (2015c) with the results from our SED modelling, we have two independent estimates on the recent star-formation activity for our spectroscopic subsample. Both diagnostics assume a particular SFH and a particular IMF. In addition, different diagnostics average the star formation activity over different time intervals, e.g. the H α SFR indicator is sensitive to the star formation activity over the past 6 Myr, whereas the SFR derived from rest-frame UV continuum averages over a time period of 100 Myr (e.g. Kennicutt & Evans 2012; Calzetti 2013). Because of the extreme nature of SLSNe, we examine whether we can isolate the differences that occur due to the time-scales that the H α and SED-inferred SFRs probe.

Assessing these differences requires that the systematic uncertainties in the data are well understood. Spectroscopic observations with slits are subject to flux losses, because a slit may only cover a part of a given galaxy. Most SLSN host galaxies are relatively compact (Lunnan et al. 2015) so that the expected losses are small. To correct these, Leloudas et al. (2015c) convolved the spectrum of a given object with the filter bandpasses of its imaging data to extract synthetic photometry. In most cases, a simple rescaling was sufficient to adjust the absolute flux scale, i.e. the extracted spectrum is representative for the entire galaxy. Only a few objects required low-order polynomials to correct the warping of the spectrum. In the following, we use the spectroscopic data of a subsample of 16 host galaxies with a reliable absolute flux scale.

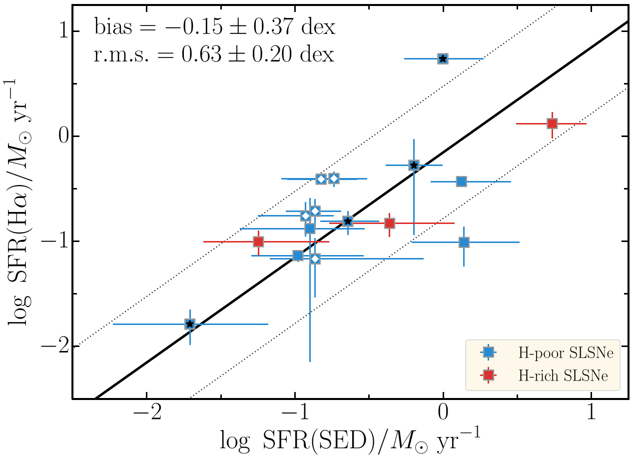

Figure 4. SFRs obtained from SED modelling and from emission lines for the spectroscopic subsample. The values in the upper left corners report the mean bias deviation and the mean rms between the H α- and SED-derived SFRs. The solid line indicates the bias between both diagnostics and the dotted lines the mean rms centred around the bias. Symbols are identical to Fig. 3.

Fig. 4 compares the extinction-corrected SFR's from SED modelling and H α emission lines of these 16 hosts. Both diagnostics reassuringly show consistency. The mean bias deviation and the mean rms between the H α and SED-derived SFRs are -0.16 ± 0.37 and 0.63 ± 0.20 dex, respectively. Conroy (2013) pointed out that a systematic uncertainty in the SED-based SFRs of a factor of 0.3 dex is expected. Our observed value is larger than the expected value but consistent within 2σ.

The most interesting object in our sample to identify differences in the SFR indicators is again the host of PTF12dam. Thöne et al.

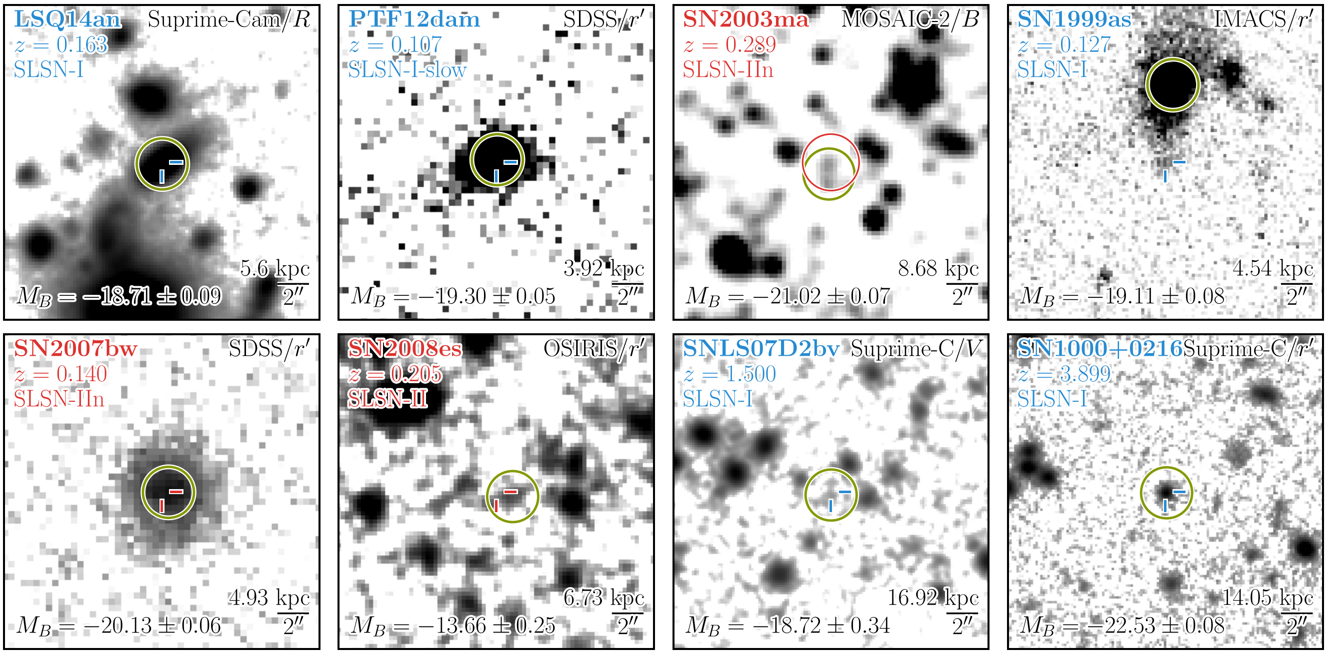

Figure 5. Selection of postage stamps of the hosts of H-poor and H-rich SLSN host galaxies in our sample. The images were taken before the SN occurred or after the SN faded. Each panel has a size of 20 arcsec × 20 arcsec, where north is up and east is left. The crosshair marks the position of the SNe after aligning on an SN and a host image (H-poor SLSN: blue and H-rich SLSNe: red). If no SN image was available, a circle in blue or red (arbitrary radius) is shown instead, indicating the SN position reported in the literature. The average alignment error is 0.17 arcsec, but it exceeds 1.0 arcsec in a few cases. The green circle (arbitrary radius) marks the host galaxy. The observed absolute B-band magnitude is displayed in the lower left corner. The image of SNLS07D2bv is smoothed with a Gaussian kernel (width of 1 pixel) to improve the visibility of the field. The complete collection of postage stamps is shown in Figs C1 and C2.

(2015) reported that the head of the tadpole galaxy is characterized by a very young stellar population which is ~3 Myr old. Calzetti (2013) showed that in such cases, the UV SFR estimator will be underestimated by a factor of a few. We measure an excess of 0.74 ± 0.27 dex in the H α inferred SFR. Even in that case, the deviation between the H α- and SED-inferred SFRs only has a significance of $<2.7\sigma$, reassuring us that even in such an extreme case the SED modelling can provide robust results.

4.2 Host offsets

Figs 5, C1, and C2 show postage stamps of each field in our sample. The detected host galaxies (detection rate of ≈90 per cent) are marked by green circles. The SN positions, after astrometrically aligning the SN and the host images, are indicated by crosshairs. The average uncertainty of 0.17 arcsec is dominated by the different pixel scales of the SN and host images. In few examples, this uncertainty exceeds 1 arcsec because of the coarse spatial resolution of the SN images, the small spatial overlap of SN and host images, or the low number of reference stars. We lack SN images for 17 hosts in our sample. Their SN positions are indicated by circles as reported in the literature.

Thanks to the high host recovery rate (85 per cent and 100 per cent for H-poor and H-rich SLSNe, respectively), we present a relatively complete distribution of the distances between the SN positions and the barycentres of the host light (predominantly in r' band) of H-poor and H-rich SLSNe. In addition, we incorporate results on CSS100217 by Drake et al. (2011a), on SN2003ma by Rest et al. (2011), and on Pan-STARRS SLSNe by Lunnan et al. (2015). The observed distribution is skewed to small radii (the expectation value being 1.3 kpc) but has a long tail extending up to 12 kpc. For the smallest offsets, the measurements are comparable to the errors. In this regime, Gaussian noise superimposed on a vector with length μ results in a non-Gaussian probability distribution of the vector length, i.e. an overestimated host offset (Rice 1944). The expected probability distribution function of a host offset measurement r is given by

$$p\,(r|\mu,\sigma) = \frac{r}{\sigma^2}\,I_0\left(\frac{r\,\mu}{\sigma^2}\right)\,\exp\left(-\frac{r^2+\mu^2}{\sigma^2}\right)$$

where μ is the true offset, σ is the dispersion of the distribution, which can be assumed to be comparable to the measurement error, and I_0 is the modified Bessel function of the first kind. By differentiating $p(r|\mu,\sigma)$ with respect to r, a closure relation can be derived between the observed offset, its error and the true offset (Wardle & Kronberg 1974):

$$I_0\left(\frac{r\,\mu}{\sigma^2}\right)\left(1-\frac{r^2}{\sigma^2}\right)+\frac{r\,\mu}{\sigma^2}\,I_1\left(\frac{r\,\mu}{\sigma^2}\right)=0\,.$$

We solved this equation numerically to build the intrinsic host offset distribution. The black curve in Fig. 6 shows the joint cumulative distribution of H-poor and -rich SLSNe. The grey-shaded regions display the expected parameter space of our distribution after bootstrapping the sample 30 000 times with darker regions, indicating a higher probability. The distribution is well described by the cumulative distribution function of a negative exponential distribution $1-\exp\left(-r/r_{\mathrm{mean}}\right)$ with a mean offset of $r_{\mathrm{mean}} \sim 1.3$ kpc.

The fit underpredicts the fraction of hosts with offsets smaller than <0.5 and >4 kpc. The discrepancy for small host offsets can be reconciled with the alignment errors between SN and host image, and intrinsically small host offsets. As the alignment error exceeds the offset measurement, the closure relation is only fulfilled if $\mu = 0$.

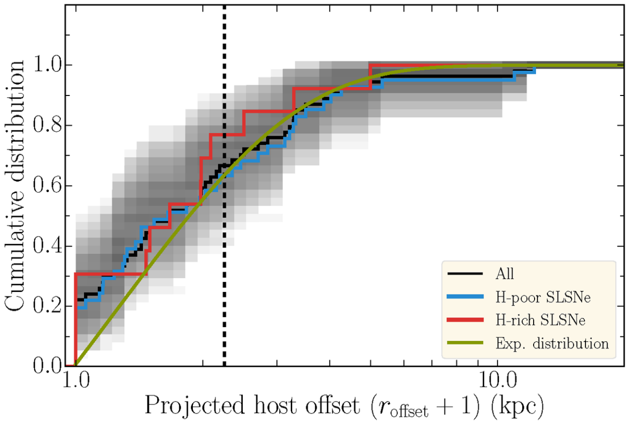

Figure 6. Host offset cumulative distribution for 41 H-poor (blue) and 13 H-rich (red) SLSNe and the total sample (black). The shaded region displays the expected parameter space after bootstrapping the sample 30 000 times. The dotted, vertical line indicates the median offset. We shifted the distribution by 1 kpc in order to use a logarithmic scaling for presentation purposes.

Therefore, the fraction of SLSNe with negligible host offsets is a strict upper limit. In addition, any inclination will lead to an underestimation of the true host offset. The blue and red curves in Fig. 6 show the observed offset distribution after separating the sample in H-poor and H-rich SLSNe, respectively. Both samples are statistically identical.

The offsets of PTF11rks and SN1999as are >10 kpc and therefore they exceed the median of 0.7 kpc by a large factor. The host of SN1999as is an irregular galaxy interacting with its environment (Fig. 5). At the explosion site, a faint object is detected in continuum. The explosion site of PTF11rks is connected by a linear feature with the nucleus (Perley et al. 2016b). This could point to a spiral galaxy morphology or galaxy interaction whereby the SN exploded in a faint satellite galaxy. Spectroscopic observation of SN1999as by Leloudas et al. (2015c) showed that the explosion site is characterized by strong emission lines. In this case, the true host is a fainter galaxy that is difficult to disentangle from the more massive galaxy.

4.3 Brightness, colour, and luminosity

4.3.1 Brightness and luminosity

More than 87 per cent of all hosts were detected at >2σ confidence in a R-band filter. Their observed distribution, displayed in the upper panel of Fig. 7, extends from $R \sim 13.3$ mag (SN2006gy) to $R \sim 27.9$ mag (SCP06F6) and shows a clear trend to fainter galaxies as redshift increases (Table 3). The average brightness of SLSN-I host galaxies decreases from $m_{\rm R} \sim 22.7$ mag at $z \sim 0.5$ to $m_{\rm R} \sim 25.4$ mag at $z > 1$, while the dispersion remains at ~1.6 mag at all redshifts. Compared to a sample of SF galaxies from the UltraVISTA survey (density plot in Fig. 7), they are on average fainter and their distributions become more incompatible as redshift increases.

The class of H-poor SLSNe is comprised of fast- and slow-declining SLSNe, which might have different progenitors and host environments. Using the gap in the decline time-scale at ~50 d (Table 1), we define a subsample of 12 fast and seven slow declining H-poor SLSNe at $z < 0.5$ (Table 1). The properties of the two samples appear to be indistinguishable (Table 3). However, the samples are too small to draw a conclusion yet.

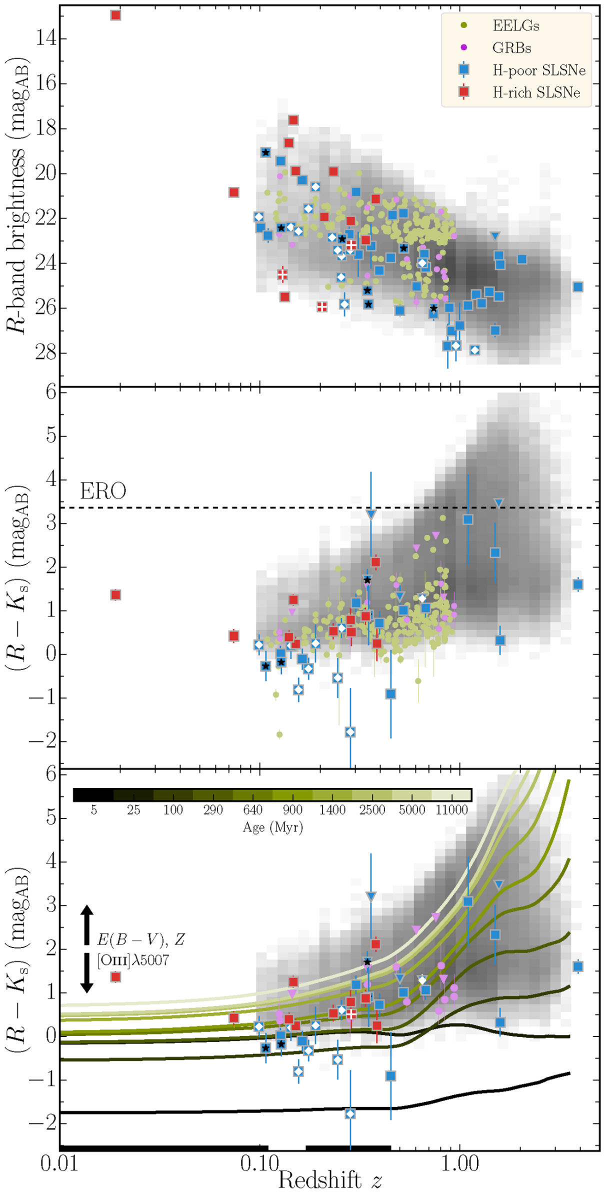

Figure 7. Top: the observed R-band host magnitude as a function of redshift for H-poor (blue) and H-rich (red) SLSNe. In case of a R-band upper limit, the measurement is displayed as a downward pointing triangle. The hosts of fast- and slow-declining H-poor SLSNe are signified by '⋆' and '◇', respectively, and SLSNe-II by '+'. Middle: the $R - K_{\rm s}$ colour evolution. The observed $R - K_{\rm s}$ colour evolution of SUSHIES, GRB host galaxies, and SF galaxies from the UltraVISTA survey (density plot). Bottom: the colour evolution of galaxies with a metallicity of 0.2 solar for different stellar population ages, derived from templates by Bruzual & Charlot (2003). The tracks are shown up to $z = 3.5$ to avoid corrections for Lyα absorption in the host galaxies and in the intergalactic medium. The vectors on the left indicate how extinction, metallicity, and emission lines with very large EWs, such as Hα and [O III] λ5007, can alter the intrinsic colour. Note, Hα and [O III] λ5007 can turn the colour to the blue only at $z \lesssim 0.11$ and between $z \sim 0.17$ and 0.45, respectively (indicated by the bars at the bottom).

Host galaxies of H-rich SLSNe are on average 1.5 mag brighter than hosts of H-poor SLSNe at $z < 0.5$ (upper panel in Fig. 7 and Table 3). Most striking about the SLSN-II/IIn host population is the exceptionally large dispersion of 3.4 mag that is even a factor of 2–3 larger than that of H-poor SLSNe and the UltraVISTA

Table 3. Statistical properties of H-poor and H-rich SLSN host galaxies per redshift bin.

Sample	Number	Mean redshift	$m_{\rm R}^{a}$ (mag)	$(R-K_{\rm s})^{a}$ (mag)	$M_{\rm B}$ (mag)	$\log M/{\rm M}_{\odot}$	log SFR (${\rm M}_{\odot}\,{\rm yr}^{-1}$)	log sSFR (${\rm yr}^{-1}$)
				$z \le 0.5$				
I-fast	11	0.21	22.96 ± 0.48	-0.10 ± 0.24 (8)	-16.71 ± 0.37	7.86 ± 0.16	-0.89 ± 0.08	-8.70 ± 0.11
			$1.46^{+0.42}_{-0.33}$	$0.41^{+0.37}_{-0.19}$	$1.14^{+0.31}_{-0.24}$	$0.45^{+0.14}_{-0.11}$	$0.03^{+0.05}_{-0.02}$	$0.05^{+0.11}_{-0.04}$
I-slow	5	0.24	23.06 ± 1.58	0.01 ± 0.26 (4)	-16.76 ± 0.96	7.69 ± 0.49	-0.73 ± 0.29	-8.55 ± 0.33
			$3.00^{+1.43}_{-0.97}$	$0.07^{+0.20}_{-0.05}$	$1.82^{+0.80}_{-0.50}$	$0.86^{+0.49}_{-0.31}$	$0.22^{+0.63}_{-0.16}$	$0.15^{+0.52}_{-0.12}$
H-poor	27	0.24	22.68 ± 0.34	0.07 ± 0.16 (16)	-17.10 ± 0.30	7.94 ± 0.13	-0.61 ± 0.11	-8.59 ± 0.10
			$1.75^{+0.27}_{-0.24}$	$0.50^{+0.16}_{-0.12}$	$1.45^{+0.23}_{-0.20}$	$0.62^{+0.12}_{-0.10}$	$0.40^{+0.13}_{-0.10}$	$0.10^{+0.24}_{-0.07}$
II	3	0.21	24.46 ± 1.46	–	-15.29 ± 1.48	7.22 ± 0.93	-1.27 ± 0.72	-8.39 ± 0.42
			$1.77^{+1.47}_{-0.80}$	–	$2.31^{+1.50}_{-0.90}$	$1.18^{+0.93}_{-0.52}$	$0.80^{+1.01}_{-0.45}$	$0.08^{+0.26}_{-0.06}$
IIn^{b}	13	0.21	20.37 ± 0.96 (12)	0.83 ± 0.22 (10)	-18.89 ± 0.67	9.08 ± 0.35	-0.16 ± 0.39 (9)	-8.71 ± 0.31(9)
			$3.25^{+0.82}_{-0.65}$	$0.60^{+0.19}_{-0.14}$	$2.30^{+0.56}_{-0.45}$	$1.23^{+0.30}_{-0.24}$	$1.03^{+0.36}_{-0.27}$	$0.57^{+0.31}_{-0.20}$
H-rich^{b}	16	0.21	21.20 ± 0.90 (15)	0.80 ± 0.20 (11)	-18.18 ± 0.70	8.74 ± 0.38	-0.45 ± 0.33 (12)	-8.61 ± 0.23(12)
			$3.41^{+0.73}_{-0.60}$	$0.57^{+0.17}_{-0.13}$	$2.70^{+0.57}_{-0.47}$	$1.37^{+0.29}_{-0.24}$	$1.05^{+0.27}_{-0.24}$	$0.46^{+0.32}_{-0.19}$
				$0.5 < z \le 1.0$				
H-poor	14	0.73	25.24 ± 0.54 (13)	1.11 ± 0.07 (4)	-17.66 ± 0.44	8.50 ± 0.24	-0.10 ± 0.19	-8.56 ± 0.21
			$1.86^{+0.47}_{-0.37}$	$0.03^{+0.05}_{-0.02}$	$1.52^{+0.34}_{-0.28}$	$0.71^{+0.22}_{-0.17}$	$0.44^{+0.25}_{-0.16}$	$0.47^{+0.18}_{-0.13}$
				$1.0 < z \le 4.0$				
H-poor	12	1.67	25.38 ± 0.43 (11)	1.59 ± 0.60 (5)	-19.86 ± 0.68	8.91 ± 0.27	0.70 ± 0.30	-8.00 ± 0.23
			$1.32^{+0.35}_{-0.27}$	$0.75^{+1.00}_{-0.43}$	$2.25^{+0.58}_{-0.46}$	$0.77^{+0.24}_{-0.18}$	$0.93^{+0.24}_{-0.19}$	$0.25^{+0.54}_{-0.17}$

Notes. The first row of each ensemble property shows the mean value and its error and the second row the standard deviation of the sample. The values of the R-band brightness, the B-band luminosity, and the $R - K_{\rm s}$ colour are not corrected for host attenuation. The H-poor and H-rich samples include all SLSNe irrespective of subtype.

^{a}The number of objects with measured $R - K_{\rm s}$ colour or with an $F625W/R/r'$-band observation are given in parenthesis, if they are less than the total number in the sample.

^{b}SNe 1999bd and 2006gy are not considered in the sSFR and SFR calculations because their SFHs is more complex than assumed in this paper, while CSS100217 and PTF11dsf are excluded because of a possible AGN contamination.

sample (Tables 3 and D1, and Fig. D1). The large dispersion remains after separating out the three SLSNe-II from the H-rich population (Table 1). The distribution is incompatible with the UltraVISTA sample (chance probability $p_{\rm ch} = 7 \times 10^{-4}$) and with the fainter and narrower distribution of SLSN-I host galaxies ($p_{\rm ch} = 8.4 \times 10^{-3}$). Among the hosts of the three SLSNe-II are two of the faintest H-rich SLSN host galaxies in our sample ($R \sim 24.6$–26.4; Table A1). They are more than a hundred times fainter than an $L^{\star}_{\rm B}$ galaxy at $z \sim 0.2$ (Faber et al. 2007), and about two magnitudes fainter than the Small Magellanic Cloud galaxy at $z \sim 0.2$.

Panel A of Fig. 8 shows the evolution of the absolute B-band luminosity (not corrected for host reddening) with redshift. The distribution spans a wide range from −13 to −22 mag. Compared with appropriate luminosity functions (e.g. Faber et al. 2007; Ilbert et al. 2005; Marchesini et al. 2007, tracks in Fig. 8), the span corresponds to a range from a few thousandths of $L^{\star}$ to a few $L^{\star}$. Clear differences are visible between hosts of H-poor and H-rich SLSNe. In their common redshift interval ($z < 0.5$), the distribution of the H-poor SLSN hosts is narrower by >1 mag and in addition shifted by ∼1 mag towards lower luminosities (Table 3). Intriguingly, the luminosity distribution shows a rapid evolution from $0.04L^{\star}$ at $z < 1$ to $\sim 0.2L^{\star}$ at $z > 1$. We discuss its origin in Section 5.1.

With the B-band luminosity distribution in hand, we put SLSN host galaxies into context with unbiased GRB and regular CCSN host galaxy samples. Between $z = 0.3$ and 1, Type I SLSNe reside in galaxies that are 1.61 ± 0.42 mag less luminous than GRBs. The AD test gives a chance probability of $p_{\rm ch} = 2 \times 10^{-4}$ that both distributions are drawn from the same parent distribution (Fig. 14). This result contradicts Japelj et al. (2016), who argued that previously claimed differences between the two populations are an artefact of the comparison methodology. We discuss this finding in Section 5.4.1 in detail. The population of SLSN-I host galaxies is also incompatible with those of regular CCSNe from untargeted surveys at all redshifts ($p_{\rm ch} < 1 \times 10^{-5}$; Fig. 14). In contrast, the SLSN-IIn host population is closer to the GRB host population ($p_{\rm ch} > 0.26$; Fig. 16).

4.3.2 R − K$_{\rm s}$ *colour*

The middle panel of Fig. 7 shows the redshift evolution of the $R - K_{\rm s}$ colour of the 25 H-poor and 11 H-rich SLSN hosts with R- and $K_{\rm s}$-band observations. The colour varies between ∼−2 and 3 mag, though with large errors. No SLSNe are found in extremely red objects ($R - K_{\rm s} \geq 3.3$ mag). At $z < 0.5$, SLSN-I hosts are characterized by significantly bluer average colours ($R - K_{\rm s} \sim 0.07$ mag; Table 3) than SF galaxies from the UltraVISTA survey (grey-shaded region; $R - K_{\rm s} \sim 1.10$ mag; Table D1). The chance of randomly drawing a distribution from the UltraVISTA sample that is at least as extreme as the SLSN-I is $<10^{-5}$. The average colour is $>0.45 \pm 0.19$ mag bluer and statistically incompatible with those extreme emission galaxies in the VUDS and zCOSMOS surveys ($p_{\rm ch} < 1 \times 10^{-2}$). At $z > 1$, the average colour increases to 1.59 ± 0.60 mag, but still remains below the average colour of UltraVISTA galaxies (2.43 mag; Tables 3 and D1).

The mean colour of hydrogen-rich SLSNe ($R - K_{\rm s} \sim 0.80$ mag) is modestly bluer compared to the general population of SF galaxies in

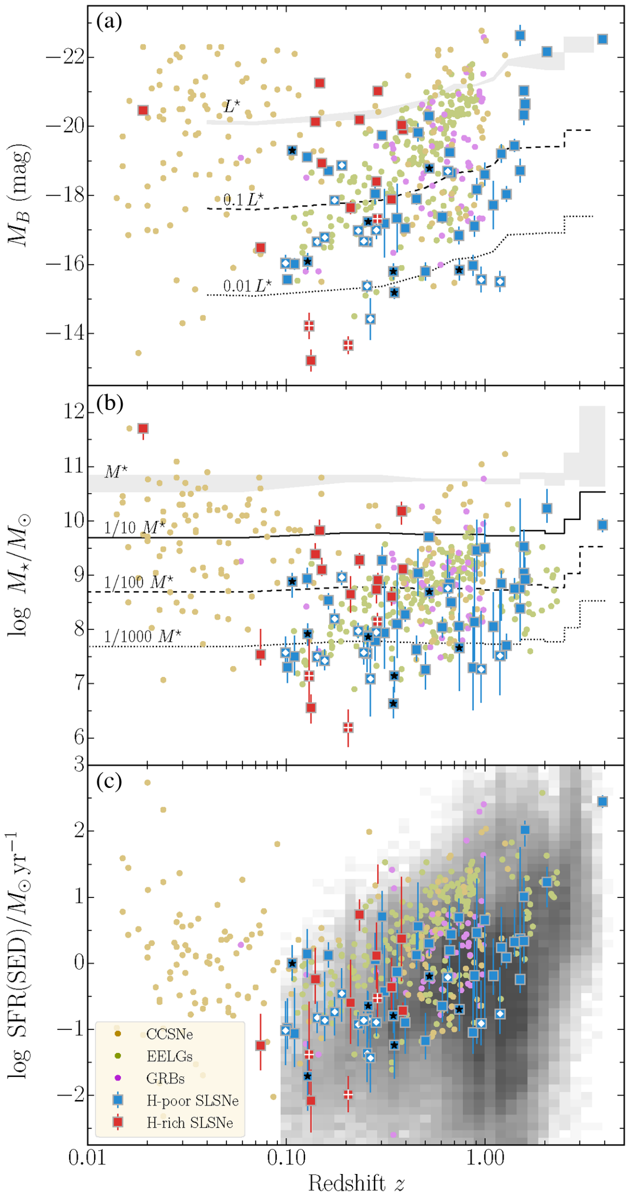

Figure 8. Evolution of the physical properties of SLSN host galaxies and comparison samples with redshift. Symbols are identical to previous figures. In panel A, we overlay the evolution of the characteristic luminosity $L^\star$ of the B-band luminosity function of blue galaxies, reported in Faber et al. (2007), Ilbert et al. (2005), and Marchesini et al. (2007) in grey, and several luminosity tracks. In panel B, we overlay the evolution of the characteristic mass $M^\star$ of the MF from the GAMA (Baldry et al. 2012) and UltraVISTA surveys in grey, and several mass tracks. These characteristic masses and luminosities are defined where the power-law form of the Schechter function cuts off. The parameter space of the UltraVISTA sample is shown as a grey-shaded density plot in panel C. For clarity, measurement errors are omitted for the comparison samples. They are comparable to those of the SLSN host galaxies.

the UltraVISTA survey and of GRB host galaxies (Tables 3 and D1). While the dispersions of the brightness and luminosity distributions are broader than of other galaxy samples, the colour distribution has a dispersion comparable to all other samples [$\sigma(R-K_\mathrm{s})\sim 0.57$ mag; Tables 3 and D1]. Hosts of Type II SLSNe tend to be too faint to obtain meaningful K_s-band constraints, which prevents contrasting their properties to the ensemble of Type IIn SLSNe.

In the bottom panel of Fig. 7, we overlay expected colour tracks for the stellar population synthesis templates from Bruzual & Charlot (2003) for a metallicity of 0.2 solar and a wide range of ages. The colour of SLSN-I hosts of ∼0 mag at $z<0.5$ points to stellar population ages of several up to a few hundred million years, whereas H-rich SLSNe are found in galaxies with a redder $R-K_\mathrm{s}$ colour because of more evolved stellar populations. However, the exact relation between colour and age is a complicated function of metallicity, extinction, the EW of emission lines and SFHs (for a detailed discussion see Conroy 2013). The vectors in Fig. 7 indicate how they can alter the intrinsic colour.

A critical aspect of this analysis is the R- and K_s-band observing completeness. Almost all hosts were observed in R band, but only ∼57 per cent were observed in K_s band. The colour incompleteness is a direct consequence of the difficulty to obtain meaningful K_s-band constraints for hosts fainter than $K_\mathrm{s}=23$–24 mag. This is supported by the SED modelling, which always suggests K_s-band magnitudes below this detection limit and colours that are comparable to the observed colour distribution. In the unlikely case that the hosts without K_s-band observations had $K_\mathrm{s}=23$–24 mag, the colour distribution would span a range from 0.3 to 4.7 mag. Such red colours are in stark contrast to the observed distribution, the SED modelling, and SN observations (e.g. Quimby et al. 2011c; Inserra et al. 2013; Lunnan et al. 2013; Nicholl et al. 2014).

4.4 Physical properties and distribution functions

In the following, we take advantage of the full SUSHIES sample and present distribution functions of the primary diagnostics mass and SFR of H-poor and H-rich SLSNe host galaxies.[12] Figs 2, B1, and B2 show the best fit of each host galaxy and the evolution of the galaxy properties are shown in Fig. 8. Table 4 lists the model parameters. The ensemble properties in different redshift bins are summarized in Table 3.

4.4.1 Stellar mass

The host masses (panel B in Fig. 8) span a range between 10^6 and $10^{10}\,\mathrm{M}_\odot$ for both classes of SLSNe. This dearth of hosts above $10^{10}\,\mathrm{M}_\odot$ is remarkable. Assuming that SLSNe populate galaxies according to their SFR, we would in fact expect ∼40 per cent of hosts galaxies to have masses above $10^{10}\,\mathrm{M}_\odot$. However, only one of the 53 SLSNe-I and two of the 16 H-rich SLSNe have such a high stellar mass. The probability of randomly drawing a sample that is at least as extreme as the SLSN-I sample from UltraVISTA, weighted by the SFR, is $<10^{-5}$ at all redshifts (Fig. 14). For H-rich SLSNe, this scenario cannot be excluded, however, as we will show below, the H-rich SLSN host sample has also some peculiar properties compared to the general population of SF galaxies. The lack of massive galaxies for both classes strongly argues for a stifled production efficiency in massive galaxies (see also Perley et al. 2016b). We investigate its origin in detail in Section 5.2.

Apart from the dearth of massive hosts, we observe clear differences between the host populations of both SLSN classes. H-poor SLSNe are preferentially found in galaxies with average masses of $\sim 10^{7.9}\,\mathrm{M}_\odot$ at $z=0.5$. As redshift increases, the average masses gradually increase to $\sim 10^{8.9}\,\mathrm{M}_\odot$ at $z>1$, while the dispersion remains constant at ∼0.65 dex (Figs 8 and D1, and Table 3). Using

---

[12] We omit discussing the age of the stellar populations and their attenuation. In particular, the age is notoriously difficult to measure accurately and precisely.

Table 4. Results from the SED modelling.

SLSN	Redshift	χ^2/n.o.f.	$E(B-V)$ (mag; host)	$M_{\rm FUV}$ (mag)	$M_{\rm B}$ (mag)	$M_{\rm Ks}$ (mag)	logSFR ($\mathrm{M}_\odot\,\mathrm{yr}^{-1}$)	log$M$ ($\mathrm{M}_\odot$)	logsSFR (yr^{-1})	logAge (yr)
SLSN-I host galaxies										
CSS140925	0.460	0.32/4	0.50	-17.96 ± 0.24	-19.82 ± 0.26	<-21.12	$0.56^{+0.66}_{-0.34}$	$9.04^{+0.44}_{-0.41}$	$-8.34^{+0.68}_{-0.67}$	$8.37^{+0.57}_{-0.65}$
DES14S2qri	1.500	1.06/4	0.07	-18.19 ± 0.82	<-22.63	<-24.15	$0.37^{+1.39}_{-0.34}$	$8.76^{+1.65}_{-0.87}$	$-8.14^{+0.73}_{-1.07}$	$8.19^{+0.80}_{-0.69}$
DES14X2byo	0.869	0.00/2	0.30	-14.86 ± 0.99	<-15.97	<-16.71	$-1.05^{+0.83}_{-0.32}$	$7.30^{+1.13}_{-0.78}$	$-8.14^{+0.72}_{-1.06}$	$8.19^{+0.79}_{-0.68}$
DES14X3taz	0.608	4.78/8	0.00	-16.57 ± 0.20	-17.37 ± 0.17	-17.13 ± 0.19	$-0.65^{+0.48}_{-0.24}$	$8.04^{+0.19}_{-0.19}$	$-8.64^{+0.46}_{-0.34}$	$8.60^{+0.33}_{-0.39}$
iPTF13ajg†	0.740	0.00/1	0.00	-16.68 ± 0.21	<-15.84	<-15.08	$-0.70^{+1.02}_{-0.33}$	$7.66^{+1.36}_{-0.79}$	$-8.15^{+0.74}_{-1.15}$	$8.22^{+0.82}_{-0.71}$
LSQ12dlf‡	0.255	0.54/5	0.00	-14.72 ± 0.25	-15.38 ± 0.17	-15.91 ± 0.31	$-1.36^{+0.54}_{-0.43}$	$7.56^{+0.33}_{-0.34}$	$-8.86^{+0.75}_{-0.85}$	$8.73^{+0.73}_{-0.57}$
LSQ14an	0.163	5.60/10	0.01	-18.34 ± 0.26	-18.71 ± 0.09	-18.60 ± 0.11	$0.12^{+0.20}_{-0.18}$	$8.54^{+0.13}_{-0.17}$	$-8.42^{+0.27}_{-0.20}$	$8.48^{+0.20}_{-0.29}$
LSQ14mo‡	0.256	2.37/5	0.00	-15.92 ± 0.08	-16.66 ± 0.11	-16.95 ± 0.13	$-0.84^{+0.42}_{-0.34}$	$7.89^{+0.15}_{-0.19}$	$-8.77^{+0.62}_{-0.43}$	$8.67^{+0.35}_{-0.48}$
LSQ14bdq†	0.345	5.77/5	0.00	-16.46 ± 0.21	-15.80 ± 0.23	<-14.09	$-0.79^{+0.39}_{-0.26}$	$6.64^{+0.30}_{-0.27}$	$-7.41^{+0.63}_{-0.52}$	$7.50^{+0.47}_{-0.76}$
LSQ14fxj	0.360	0.27/3	0.00	-18.40 ± 0.99	-17.34 ± 0.99	<-16.03	$-0.13^{+0.63}_{-0.41}$	$8.10^{+0.94}_{-0.62}$	$-8.10^{+0.71}_{-1.09}$	$8.16^{+0.83}_{-0.67}$
MLS121104	0.303	8.46/7	0.20	-18.18 ± 0.17	-19.74 ± 0.14	-20.57 ± 0.13	$0.71^{+0.39}_{-0.56}$	$9.27^{+0.25}_{-0.24}$	$-8.56^{+0.59}_{-0.82}$	$8.60^{+0.86}_{-0.57}$
PS1-10ky	0.956	0.01/4	0.20	-15.66 ± 0.99	-15.56 ± 0.37	<-13.73	$-0.91^{+0.65}_{-0.33}$	$7.27^{+1.07}_{-0.61}$	$-8.06^{+0.68}_{-0.99}$	$8.10^{+0.86}_{-0.63}$
PS1-10pm	1.206	0.30/4	0.50	<-17.61	-19.21 ± 0.26	-19.68 ± 0.09	$0.24^{+0.62}_{-0.26}$	$8.85^{+0.23}_{-0.69}$	$-8.42^{+0.79}_{-0.57}$	$8.45^{+0.52}_{-0.74}$
PS1-10ahf	1.158	3.98/5	0.30	-17.10 ± 0.25	-17.72 ± 0.99	-17.62 ± 0.99	$-0.19^{+0.56}_{-0.29}$	$8.05^{+0.63}_{-0.59}$	$-8.10^{+0.66}_{-0.75}$	$8.15^{+0.59}_{-0.62}$
PS1-10awh	0.909	0.09/4	0.50	<-14.11	-18.18 ± 0.32	-22.01 ± 0.28	$0.46^{+0.82}_{-1.68}$	$9.45^{+0.56}_{-0.56}$	$-9.22^{+0.98}_{-1.36}$	$8.97^{+0.63}_{-0.67}$
PS1-10bzj‡	0.649	51.95/5	0.00	-18.64 ± 0.09	-18.70 ± 0.12	-18.18 ± 0.17	$-0.21^{+0.17}_{-0.54}$	$8.76^{+0.61}_{-0.35}$	$-8.95^{+0.49}_{-1.12}$	$8.93^{+0.66}_{-0.41}$
PS1-11ap†	0.524	1.83/5	0.00	-18.00 ± 0.05	-18.79 ± 0.11	-18.55 ± 0.37	$-0.20^{+0.19}_{-0.19}$	$8.70^{+0.13}_{-0.13}$	$-8.89^{+0.22}_{-0.21}$	$8.71^{+0.28}_{-0.24}$
PS1-11tt	1.283	0.00/2	0.00	<-18.49	-18.04 ± 0.22	-17.24 ± 0.07	$0.09^{+0.29}_{-0.17}$	$7.71^{+0.22}_{-0.25}$	$-7.58^{+0.38}_{-0.35}$	$7.65^{+0.34}_{-0.40}$
PS1-11afv	1.407	0.00/2	0.10	<-18.70	-19.45 ± 0.19	-19.79 ± 0.09	$0.32^{+0.50}_{-0.22}$	$8.76^{+0.19}_{-0.19}$	$-8.39^{+0.49}_{-0.35}$	$8.42^{+0.29}_{-0.46}$
PS1-11aib	0.997	1.34/5	0.20	-15.62 ± 0.71	-18.61 ± 0.34	-21.11 ± 0.32	$0.65^{+0.97}_{-1.65}$	$9.50^{+0.52}_{-0.52}$	$-9.01^{+1.02}_{-1.52}$	$8.88^{+0.67}_{-0.84}$
PS1-11bam	1.565	0.56/5	0.02	-20.81 ± 0.14	-21.03 ± 0.15	-20.66 ± 0.15	$1.01^{+0.29}_{-0.18}$	$9.04^{+0.37}_{-0.37}$	$-8.01^{+0.56}_{-0.52}$	$8.04^{+0.52}_{-0.51}$
PS1-11bdn	0.738	31.69/5	0.50	-15.19 ± 0.11	-16.84 ± 0.25	<-16.49	$0.69^{+0.29}_{-0.29}$	$8.06^{+0.25}_{-0.26}$	$-7.42^{+0.51}_{-0.48}$	$7.50^{+0.45}_{-0.55}$
PS1-12zn	0.674	12.73/12	0.20	-17.76 ± 0.14	-18.65 ± 0.06	-19.37 ± 0.07	$0.43^{+0.13}_{-0.13}$	$8.50^{+0.11}_{-0.12}$	$-8.06^{+0.16}_{-0.21}$	$8.14^{+0.23}_{-0.18}$
PS1-12bmy	1.566	3.22/6	0.00	-18.96 ± 0.11	-20.33 ± 0.29	<-19.79	$0.34^{+0.44}_{-0.33}$	$9.53^{+0.31}_{-0.26}$	$-9.31^{+0.69}_{-0.36}$	$8.92^{+0.58}_{-0.42}$
PS1-12bqf	0.522	9.88/15	0.10	-18.55 ± 0.09	-20.30 ± 0.05	-21.14 ± 0.07	$0.30^{+0.17}_{-0.19}$	$9.71^{+0.04}_{-0.04}$	$-9.40^{+0.16}_{-0.23}$	$8.93^{+0.08}_{-0.05}$
PS1-13gt	0.884	0.00/1	0.00	<-18.13	<-17.11	<-16.04	$-0.19^{+0.84}_{-0.35}$	$8.14^{+1.18}_{-0.72}$	$-8.15^{+0.74}_{-1.11}$	$8.22^{+0.82}_{-0.71}$
PTF09atu	0.501	0.93/5	0.00	<-15.22	-15.80 ± 0.25	<-14.98	$-1.18^{+0.42}_{-0.27}$	$7.26^{+0.32}_{-0.36}$	$-8.38^{+0.61}_{-0.55}$	$8.40^{+0.47}_{-0.60}$
PTF09cnd†	0.258	2.67/6	0.00	-16.97 ± 0.32	-17.24 ± 0.08	-16.87 ± 0.46	$-0.64^{+0.21}_{-0.18}$	$7.87^{+0.20}_{-0.21}$	$-8.49^{+0.32}_{-0.31}$	$8.52^{+0.21}_{-0.31}$
PTF10hgi‡	0.099	7.40/7	0.01	-14.36 ± 0.24	-16.04 ± 0.24	-16.09 ± 0.18	$-1.02^{+0.44}_{-0.52}$	$7.58^{+0.29}_{-0.31}$	$-8.62^{+0.69}_{-0.71}$	$8.61^{+0.38}_{-0.61}$
PTF10vqv	0.452	0.51/6	0.07	-18.60 ± 0.12	-17.90 ± 0.17	-16.92 ± 0.99	$0.12^{+0.33}_{-0.21}$	$7.63^{+0.26}_{-0.21}$	$-7.48^{+0.46}_{-0.37}$	$7.55^{+0.36}_{-0.54}$
PTF11rks‡	0.190	8.72/9	0.00	-17.27 ± 0.50	-18.87 ± 0.07	-19.20 ± 0.41	$-0.46^{+0.38}_{-0.43}$	$8.96^{+0.12}_{-0.14}$	$-9.43^{+0.44}_{-0.46}$	$8.98^{+0.36}_{-0.31}$
PTF12dam†	0.107	24.66/13	0.02	-18.65 ± 0.19	-19.30 ± 0.05	-18.61 ± 0.32	$-0.00^{+0.27}_{-0.26}$	$8.89^{+0.15}_{-0.30}$	$-8.87^{+0.35}_{-0.19}$	$8.69^{+0.29}_{-0.36}$
SCP06F6‡	1.189	0.00/1	0.00	-16.56 ± 0.21	<-15.50	<-14.19	$-0.77^{+0.70}_{-0.30}$	$7.51^{+1.21}_{-0.72}$	$-8.10^{+0.71}_{-1.05}$	$8.14^{+0.81}_{-0.66}$
SN1999as	0.127	17.97/11	0.10	-17.93 ± 0.28	-19.11 ± 0.08	-19.38 ± 0.13	$0.14^{+0.37}_{-0.35}$	$8.94^{+0.20}_{-0.17}$	$-8.83^{+0.48}_{-0.39}$	$8.65^{+0.33}_{-0.33}$
SN2005ap‡	0.283	10.52/10	0.00	-16.44 ± 0.10	-17.00 ± 0.25	-16.21 ± 0.36	$-0.89^{+0.19}_{-0.21}$	$7.95^{+0.11}_{-0.15}$	$-8.82^{+0.26}_{-0.21}$	$8.66^{+0.25}_{-0.22}$
SN2006oz	0.396	15.05/7	0.15	-15.50 ± 0.25	-17.05 ± 0.08	-17.53 ± 0.22	$-0.90^{+0.37}_{-0.47}$	$8.27^{+0.14}_{-0.12}$	$-9.18^{+0.38}_{-0.52}$	$8.89^{+0.41}_{-0.34}$
SN2007bi†	0.128	6.62/9	0.04	-14.52 ± 0.34	-16.09 ± 0.24	-15.73 ± 0.24	$-1.71^{+0.53}_{-0.52}$	$7.92^{+0.20}_{-0.21}$	$-9.68^{+0.65}_{-0.41}$	$8.88^{+0.15}_{-0.27}$
SN2009de	0.311	0.99/4	0.30	-16.50 ± 0.99	-17.19 ± 0.99	<-17.87	$-0.42^{+0.70}_{-0.45}$	$7.94^{+0.93}_{-0.66}$	$-8.20^{+0.76}_{-1.27}$	$8.26^{+1.04}_{-0.73}$
SN2009jh†	0.349	5.87/5	0.15	<-14.85	-15.19 ± 0.18	-15.70 ± 0.16	$-1.24^{+0.42}_{-0.51}$	$7.15^{+0.36}_{-0.30}$	$-8.36^{+0.69}_{-0.92}$	$8.42^{+0.60}_{-0.69}$
SN2010gx‡	0.230	2.85/5	0.00	-16.30 ± 0.06	-16.98 ± 0.06	-16.96 ± 0.05	$-0.93^{+0.19}_{-0.32}$	$7.97^{+0.14}_{-0.13}$	$-8.89^{+0.23}_{-0.37}$	$8.87^{+0.13}_{-0.30}$
SN2010kd	0.101	4.37/5	0.15	-15.83 ± 0.53	-15.57 ± 0.07	-15.22 ± 0.07	$-0.98^{+0.44}_{-0.31}$	$7.30^{+0.25}_{-0.29}$	$-8.25^{+0.61}_{-0.52}$	$8.30^{+0.40}_{-0.59}$
SN2011ep	0.280	0.02/4	0.15	-18.17 ± 0.41	<-18.05	<-16.02	$0.05^{+0.41}_{-0.30}$	$7.79^{+0.42}_{-0.36}$	$-7.71^{+0.51}_{-0.58}$	$7.74^{+0.59}_{-0.49}$
SN2011ke‡	0.143	2.70/6	0.00	-16.38 ± 0.09	-16.66 ± 0.06	-16.57 ± 0.27	$-0.82^{+0.24}_{-0.23}$	$7.50^{+0.20}_{-0.18}$	$-8.34^{+0.31}_{-0.23}$	$8.40^{+0.25}_{-0.33}$
SN2011kf‡	0.245	4.60/6	0.00	-16.41 ± 0.08	-16.68 ± 0.08	-15.72 ± 0.43	$-0.86^{+0.18}_{-0.20}$	$7.58^{+0.19}_{-0.22}$	$-8.43^{+0.33}_{-0.32}$	$8.43^{+0.24}_{-0.29}$
SN2012il‡	0.175	12.26/10	0.02	-16.82 ± 0.37	-17.86 ± 0.09	-17.19 ± 0.21	$-0.74^{+0.22}_{-0.36}$	$8.20^{+0.18}_{-0.17}$	$-8.92^{+0.27}_{-0.48}$	$8.68^{+0.27}_{-0.19}$
SN2013dg‡	0.265	0.11/3	0.80	-11.05 ± 0.68	-14.42 ± 0.60	<-17.15	$-1.43^{+0.80}_{-0.52}$	$7.09^{+0.82}_{-0.70}$	$-8.34^{+0.81}_{-1.32}$	$8.39^{+1.09}_{-0.78}$
SN2013hy	0.663	0.31/4	0.01	-18.39 ± 0.14	-19.25 ± 0.11	-19.06 ± 0.18	$0.20^{+0.68}_{-0.30}$	$8.85^{+0.21}_{-0.19}$	$-8.59^{+0.62}_{-0.42}$	$8.56^{+0.39}_{-0.54}$
SN2015bn	0.110	8.18/6	0.30	-14.81 ± 0.59	-16.02 ± 0.17	-17.27 ± 0.41	$-1.06^{+0.69}_{-0.50}$	$7.50^{+0.38}_{-0.35}$	$-8.51^{+0.72}_{-0.73}$	$8.52^{+0.50}_{-0.66}$
SN1000+0216	3.899	42.94/11	0.30	-21.52 ± 0.08	-22.53 ± 0.08	-23.65 ± 0.28	$2.45^{+0.09}_{-0.09}$	$9.93^{+0.12}_{-0.13}$	$-7.46^{+0.14}_{-0.18}$	$7.53^{+0.16}_{-0.21}$

Table 4 – *continued*

SLSN	Redshift	χ^2/n.o.f.	$E(B-V)$ (mag; host)	$M_{\rm FUV}$ (mag)	$M_{\rm B}$ (mag)	$M_{\rm Ks}$ (mag)	logSFR ($M_\odot$ yr^{-1})	log$M$ ($M_\odot$)	logsSFR (yr^{-1})	logAge (yr)
SN2213-1745	2.046	0.34/6	0.02	-21.00 ± 0.05	-22.16 ± 0.13	-21.44 ± 0.13	$1.23^{+0.23}_{-0.38}$	$10.23^{+0.36}_{-0.26}$	$-9.15^{+0.55}_{-0.34}$	$8.90^{+0.43}_{-0.41}$
SNLS06D4eu	1.588	2.47/7	0.30	-20.00 ± 0.05	-20.65 ± 0.18	< -19.34	$2.02^{+0.14}_{-0.25}$	$8.92^{+0.41}_{-0.11}$	$-6.91^{+0.25}_{-0.65}$	$6.96^{+0.65}_{-0.27}$
SNLS07D2bv	1.500	5.34/9	0.00	-17.66 ± 0.20	-18.72 ± 0.34	-19.23 ± 0.60	$-0.24^{+0.35}_{-0.20}$	$8.39^{+0.62}_{-0.60}$	$-8.58^{+0.76}_{-0.79}$	$8.57^{+0.74}_{-0.68}$
SSS120810‡	0.156	5.20/7	0.00	-16.61 ± 0.18	-16.79 ± 0.11	-15.80 ± 0.24	$-0.86^{+0.73}_{-0.31}$	$7.42^{+0.21}_{-0.17}$	$-8.35^{+1.00}_{-0.31}$	$8.27^{+0.30}_{-0.82}$
SLSN-IIn host galaxies										
CSS100217	0.147	78.34/11	0.50	-19.64 ± 0.09	-21.26 ± 0.05	-21.76 ± 0.05	$2.35^{+0.24}_{-0.14}$	$9.82^{+0.20}_{-0.07}$	$-7.46^{+0.10}_{-0.11}$	$7.53^{+0.08}_{-0.05}$
PTF10heh	0.338	2.97/7	0.15	-15.84 ± 0.21	-17.88 ± 0.09	-18.66 ± 0.13	$-0.36^{+0.44}_{-0.41}$	$8.61^{+0.17}_{-0.17}$	$-8.97^{+0.56}_{-0.54}$	$8.87^{+0.60}_{-0.47}$
PTF10qaf	0.284	0.49/6	0.00	-17.71 ± 0.16	-18.40 ± 0.15	-18.98 ± 0.19	$0.11^{+0.50}_{-0.50}$	$8.73^{+0.22}_{-0.25}$	$-8.61^{+0.71}_{-0.73}$	$8.63^{+0.69}_{-0.67}$
PTF11dsf	0.385	18.56/8	0.00	-18.84 ± 0.30	-19.91 ± 0.07	-19.09 ± 0.38	$-0.72^{+0.12}_{-0.13}$	$9.12^{+0.07}_{-0.07}$	$-9.85^{+0.13}_{-0.16}$	$8.67^{+0.04}_{-0.05}$
SN1999bd	0.151	52.37/11	0.80	-16.02 ± 0.33	-18.95 ± 0.07	-19.99 ± 0.10	$2.42^{+0.22}_{-0.10}$	$9.10^{+0.22}_{-0.11}$	$-6.70^{+0.07}_{-0.07}$	$6.70^{+0.03}_{-0.03}$
SN2003ma	0.289	1.43/4	0.04	-21.31 ± 0.08	-21.02 ± 0.07	-20.91 ± 0.17	$1.34^{+0.16}_{-0.13}$	$8.91^{+0.13}_{-0.12}$	$-7.55^{+0.21}_{-0.24}$	$7.63^{+0.24}_{-0.29}$
SN2006gy	0.019	46.32/10	0.15	-13.54 ± 0.10	-20.46 ± 0.05	-22.99 ± 0.05	$-1.12^{+0.08}_{-0.08}$	$11.70^{+0.06}_{-0.21}$	$-6.78^{+0.12}_{-7.17}$	$9.91^{+0.10}_{-3.18}$
SN2006tf	0.074	8.54/11	0.07	-15.45 ± 0.18	-16.49 ± 0.06	-17.05 ± 0.10	$-1.25^{+0.48}_{-0.37}$	$7.54^{+0.47}_{-0.20}$	$-8.88^{+0.35}_{-0.29}$	$8.86^{+0.40}_{-0.35}$
SN2007bw	0.140	14.85/8	0.04	-17.72 ± 0.25	-20.13 ± 0.06	-20.59 ± 0.09	$-0.24^{+0.47}_{-0.37}$	$9.39^{+0.19}_{-0.09}$	$-9.74^{+0.53}_{-0.25}$	$8.70^{+0.30}_{-0.07}$
SN2008am	0.233	5.63/12	0.20	-19.02 ± 0.11	-20.19 ± 0.06	-20.70 ± 0.14	$0.74^{+0.23}_{-0.24}$	$9.28^{+0.13}_{-0.15}$	$-8.50^{+0.20}_{-0.35}$	$8.57^{+0.33}_{-0.24}$
SN2008fz	0.133	1.53/6	0.01	-12.43 ± 0.55	-13.22 ± 0.32	-13.56 ± 0.08	$-2.08^{+0.47}_{-0.48}$	$6.55^{+0.25}_{-0.28}$	$-8.64^{+0.71}_{-0.67}$	$8.62^{+0.41}_{-0.62}$
SN2009nm	0.210	2.39/5	0.15	-14.61 ± 0.21	-17.65 ± 0.18	-17.71 ± 0.21	$-0.60^{+0.65}_{-0.62}$	$8.65^{+0.33}_{-0.34}$	$-9.20^{+0.79}_{-0.83}$	$8.95^{+0.62}_{-0.52}$
SN2011cp	0.380	10.25/9	0.30	-16.90 ± 0.28	-20.04 ± 0.14	-21.79 ± 0.08	$0.37^{+0.93}_{-0.64}$	$10.18^{+0.17}_{-0.25}$	$-9.88^{+1.28}_{-0.70}$	$9.53^{+0.32}_{-0.89}$
SLSN-II host galaxies										
CSS121015‡	0.287	0.97/6	0.00	-16.70 ± 0.08	-17.33 ± 0.07	-17.53 ± 0.29	$-0.52^{+0.38}_{-0.29}$	$8.15^{+0.15}_{-0.17}$	$-8.69^{+0.51}_{-0.35}$	$8.65^{+0.33}_{-0.43}$
SN2008es‡	0.205	0.84/4	0.00	-12.95 ± 0.30	-13.66 ± 0.25	-12.79 ± 0.40	$-1.99^{+0.28}_{-0.27}$	$6.19^{+0.33}_{-0.36}$	$-8.15^{+0.57}_{-0.54}$	$8.19^{+0.43}_{-0.53}$
SN2013hx‡	0.130	1.55/3	0.50	-12.04 ± 0.38	-14.22 ± 0.38	-16.43 ± 0.33	$-1.38^{+0.81}_{-0.60}$	$7.14^{+0.71}_{-0.67}$	$-8.33^{+0.79}_{-1.32}$	$8.38^{+1.10}_{-0.77}$

Notes. The absolute magnitudes are not corrected for host reddening, to compare those measurements with luminosity functions from flux-limited surveys. The SFRs are corrected for host reddening. The host attenuation was modelled with the Calzetti model. The abbreviation 'n.o.f.' stands for number of filters. The age refers to the age of the stellar population. Objects with measured decline time-scale are marked by a †/‡ if their decay is slower/faster than 50 d. For details on the fitting, see Section 3.3.

the parametrization of the MF in Muzzin et al. (2013), the average masses correspond to 1/500 and 1/50 $M^\star$ at $z \sim 0.5$ and 1, respectively. Differences between the hosts of fast- and slow-declining SLSNe are not present in our sample. A two-sided AD test gives p value of 0.72.

Hydrogen-rich SLSNe, in contrast to SLSNe-I, probe a significantly larger portion of the parameter space of the general population of SF galaxies. Their distribution is not only shifted by 0.8 dex to higher masses, but the distribution also includes three hosts that are even less massive than the least massive SLSN-I host. The dispersion is ~0.8 dex broader compared to the H-poor sample and even ~0.5 dex broader compared to the UltraVISTA survey (Tables 3 and D1). Despite a larger dispersion, the probability of randomly drawing a distribution that is at least as extreme as the H-rich population from the UltraVISTA sample is 25 per cent and hence does not point to a significant difference to the general population of SF galaxies Even after separating out the three SLSNe-II, of which two occurred in galaxies with masses between 10^6 and 10^7 $M_\odot$, the dispersion remains unchanged. While this result is noteworthy, the chance probability to randomly draw the SLSN-IIn sample from the UltraVISTA sample is 21 per cent (Fig. 16).

4.4.2 *Star formation rate*

Panel C in Fig. 8 displays the evolution of the dust-corrected SFR. Hosts of H-poor SLSNe have similar SFRs to the general population of SF galaxies (Tables 3 and D1), but smaller SFRs than host galaxies of GRBs and regular CCSNe. The mean SFR rapidly grows with increasing lookback time from 0.25 $M_\odot$ yr^{-1}, at $z < 0.5$ to 5 $M_\odot$ yr^{-1} at $z > 1$ (Table 3). In singular cases, the SFR reaches >100 $M_\odot$ yr^{-1} (SN1000+0216 and SNLS06D4eu; Fig. 8). While the mean value evolves with redshift, the dispersion remains constant at ~0.4 dex. The SFR increases somewhat faster compared to UltraVISTA, out to $z \sim 2$, but statistically both distributions remain similar (Fig. 14).

Host galaxies of H-rich SLSNe exhibit different characteristics. The three H-rich SLSNe with broad Balmer emission lines exploded in galaxies with low SFRs. Two of the hosts (SNe 2008es and 2013hx) have very low SFRs between 0.01 and 0.1 $M_\odot$ yr^{-1}. In contrast, SLSNe-IIn are found in a more diverse population of SF galaxies. Their defining property is again the large dispersion of ~1 dex (Table 3). Their average SFR is only modestly larger compared to the galaxy samples discussed in this paper (Fig. D1).

Although the SFRs of SLSN-I hosts are similar to the general population of SF galaxies, they are on average less vigorously SF than GRB and regular CCSN host galaxies. However, in the previous section, we revealed that especially the H-poor SLSNe are found in very low-mass galaxies. Likewise, hosts of H-rich SLSNe have higher average SFRs but their mass distribution is skewed to higher masses and is substantially broader. To better understand how SLSN host galaxies fit in the context of other galaxy samples, we normalize the SFR by the stellar mass (so-called specific star formation rate, sSFR).

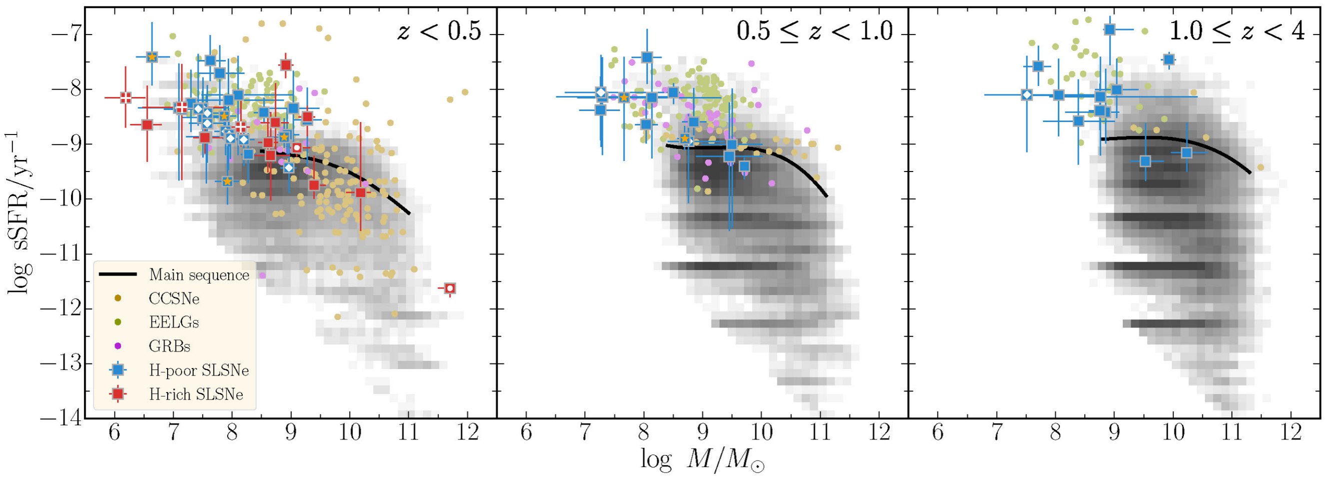

Figure 9. sSFRversus stellar mass in three different redshift intervals. The SUSHIES sample is displayed in red and blue. Similar to previous figures, hosts of slow- and fast-declining SLSNe-I are signified by '⋆' and '◇', respectively. In contrast to the other plots, we use the H α and IR luminosity as an SFR indicator for SLSNe-IIn SN1999bd and SN2006gy, respectively (highlighted by a •; measurements taken from Smith et al. 2007 and Leloudas et al. 2015c). Overlaid are the locus of SF galaxies from the UltraVISTA survey (grey-shaded area) and of other comparison samples (in colour). The black curve shows the location of the galaxy main sequence in each redshift bin. The values were taken from Whitaker et al. (2014) and Lee et al. (2015). Measurement errors are omitted for comparison samples. They are similar to those of SLSN host galaxies.

Fig. 9 displays the two classes of SLSNe in the sSFR–mass plane in three different redshift intervals. Both classes are characterized by high sSFR between $10^{-8.7}$ and $10^{-8.0}$ yr^{-1} at all redshifts. They reside in a part of the parameter space well above the galaxy main sequence (black curves in Fig. 9) that is occupied by starburst galaxies. The most extreme hosts have sSFR that are two orders of magnitude in excess to the galaxy main sequence, indicating that some hosts experience very extreme starbursts. In general, SLSN-I hosts are found in the region of the parameter space that is occupied by EELGs and more extreme than of GRBs and of regular CCSNe, which trace the bulk of the population of SF galaxies. Host galaxies of H-rich SLSNe have high sSFR as well but because of their high stellar masses, their parameter space is more extended.

4.5 A radio perspective on SLSN host galaxies

Radio emission from SF galaxies is an excellent tracer of the total SFR (Condon 1992; Schmitt et al. 2006; Murphy et al. 2011; Calzetti 2013). In contrast to SED modelling and emission-line diagnostics, e.g. Balmer lines, it is independent of any extinction correction, although radio SFRs do suffer from time delay for SNe to explode and create sufficient cosmic rays.

Almost all SLSN hosts lie in the footprints of wide-field radio surveys, such as FIRST, NVSS, and SUMSS. All hosts evaded detection in individual images down to the nominal rms levels of the surveys: FIRST ∼ 0.15 mJy beam^{-1}, NVSS ∼ 0.45 mJy beam^{-1}, and SUMSS ∼ 1.3 mJy beam^{-1} (see Table A2 for individual measurements). To place tighter constraints on the average radio brightness of the host populations, we stack the data of the 51 fields with VLA FIRST data. We first divide the sample into three redshift bins ($z \leq 0.5$, $0.5 < z \leq 1.0$, and $z > 1$) and according to the SN type. Afterwards, we centre the images on the SN positions and median combine them. Also, in the stacks no host population is detected down to an rms of 32–60 μJy beam^{-1} at all redshifts (Table 5).

Table 5. Properties of the stacked FIRST data.

Redshift interval	Number	rms (μJy beam^{-1})	log SFR(tot.) (M$_\odot$yr^{-1})	log SFR(SED) (M$_\odot$yr^{-1})
		H-poor SLSN host galaxies		
$z \leq 0.5$ $(\langle z \rangle = 0.26)$	17	42.5	<1.11	− 0.61 ± 0.12
$0.5 < z \leq 1.0$ $(\langle z \rangle = 0.74)$	12	44.2	<1.96	− 0.10 ± 0.19
$1.0 < z \leq 4.0$ $(\langle z \rangle = 1.41)$	9	56.3	<2.51	0.68 ± 0.30
		H-rich SLSN host galaxies		
$z \leq 0.5$ $(\langle z \rangle = 0.21)$	13	49.4	<1.00	− 0.44 ± 0.36
		H-poor and H-rich SLSN host galaxies		
$z \leq 0.5$ $(\langle z \rangle = 0.23)$	30	32.2	<0.90	− 0.42 ± 0.17

Notes. The rms level is calculated from the stacked FIRST image and converted into a 4σ limit on the total unobscured SFR at the median redshift of each sample. The weighted means of the SED-derived SFR is reported for comparison. For details, see Section 4.5. The second value in the redshift column reports the mean redshift of each redshift interval.

Following the method in Michałowski et al. (2009), we translate the flux density into SFR limits.[13] The non-detections correspond to 4σ SFR limits between 8.0 M$_\odot$ yr^{-1} at $z \sim 0.23$ to 326 M$_\odot$ yr^{-1} at $z \sim 1.41$, and exceed the SED-derived SFRs by factors 21–120 (Table 5). This allows ruling out truly extreme obscured star formation, in agreement with the observed $R - K_s$ colours and the absence of reddened SLSNe in our sample.

In addition to the survey data, the hosts of MLS121104, SN2005ap, and SN2008fz were targets of our JVLA campaign.

---

[13] This method is based on Bell (2003) and assumes a power-law-shaped radio continuum with a spectral index of $\alpha = -0.75$ ($F_\nu \propto \nu^\alpha$; Condon 1992; Ibar et al. 2009).

All three hosts evaded detection down to nominal rms values of 15, 25, and 15 μJy beam^{-1} for MLS121104, SN2005ap, and SN2008fz, respectively. Those limits correspond to 4σ SFR limits of 6.2, 9.0, and 1.6 $M_{\odot}$ yr^{-1}, respectively. The limit on MLS121104 is of particular interest. It is the only known host with a supersolar metal abundance. The SED modelling revealed a dust-corrected SFR of $5.13^{+7.46}_{-3.72}$ $M_{\odot}$ yr^{-1} (Table 4), which is comparable to the radio limit within errors, implying that the optical diagnostics probed the total star formation activity in the galaxy. The high upper limits on the hosts of SNe 2005ap and 2008fz exceed the SED–SFRs by at least a factor of 50 and, hence, do not have much meaning (Table 4).

5 DISCUSSION

5.1 Evolution of SLSN-I host galaxies

In the previous sections, we revealed a rapid evolution of *B*-band luminosity and the SFR of SLSN-I host galaxies. In the following, we quantify how mass, far-UV (FUV) luminosity (as a tracer of the SFR), and the *B*-band luminosity of the SLSN-I host population evolve throughout cosmic time. The redshift evolution of these diagnostics is displayed in Fig. 10 (left-hand panels). We fit these data with the linear model $Y = A + B\log(1 + z)$ and propagate errors through an MC simulation and bootstrapping, as described in Section 3.4.

The left-hand panels in Fig. 10 show the best fits and their 1σ error contours. The mass, FUV, and the *B*-band luminosity of SLSN-I hosts show a moderate to strong redshift dependence with a linear correlation coefficient between $|r| = 0.5$ and 0.6 (Table 6). The probability of generating each of these linear correlations by chance is between 4×10^{-5} and 3.5×10^{-6}, respectively (∼4.0–4.5σ; Table 6).

To isolate the differential evolution of SLSN host galaxies from known global trends, we repeat the analysis after subtracting the evolution of the MF, and the FUV and *B*-band luminosity functions of SF galaxies. As tracers for the secular evolution, we use the characteristic luminosities and masses of the luminosity and MFs: FUV: Wyder et al. (2005) and Cucciati et al. (2012); *B* band: Madgwick et al. (2002), Faber et al. (2007), and Marchesini et al. (2007); and mass: Baldry et al. (2012), Muzzin et al. (2013), and Grazian et al. (2015).

The right-hand panels in Fig. 10 show the redshift evolution of the host properties after detrending. The strong redshift evolution in the *B* band and the FUV is consistent with the general cosmic evolution of SF galaxies. After detrending the data, the differential evolution in the FUV and *B* band is consistent with no evolution. The chance probability increases from $<4 \times 10^{-5}$ to $>2 \times 10^{-2}$ (i.e. $<3\sigma$; Table 6). The galaxy mass, on the other hand, still shows a moderate redshift dependence [$\Delta M/\Delta\log(1 + z) = 2.92^{+0.89}_{-0.88}$], though with a significantly higher chance probability of 1.1×10^{-4} (equivalent to 3.9σ; Table 6).

Intriguingly, the rate with which the stellar mass of SLSN-I host galaxies increases with redshift before and after detrending is close to the redshift dependence of the characteristic mass in the mass–metallicity relation [$\Delta M/\Delta\log(1 + z) \sim 2.64$; Zahid et al. 2014. This suggests that metallicity could be a regulating factor in the SLSN production (as argued by Chen et al. 2016 and Perley et al. 2016b). In the following section, we investigate this relationship in detail.

Due to the small redshift range probed by our H-rich SLSN sample, the redshift dependence of their physical properties is inconclusive.

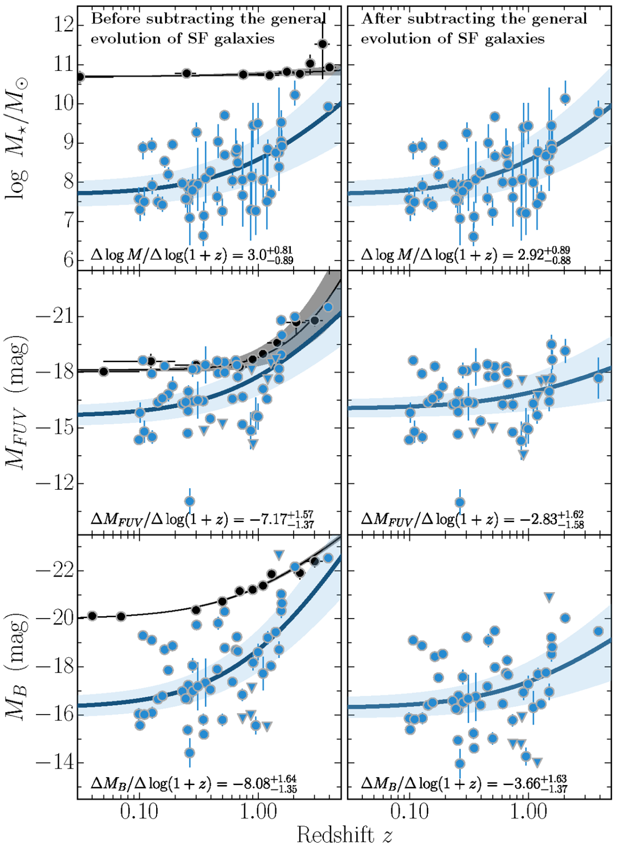

Figure 10. Mass, FUV luminosity at 1500 Å (as proxy of the observed SFR), and *B*-band luminosity plotted versus redshift (detections: ● and non-detections: ▼). The observed evolution (left-hand panels) is the sum of the differential evolution of SLSN-I host galaxies and the general cosmic evolution of SF galaxies. This general cosmic evolution is indicated by the evolution of the characteristic luminosity and mass of appropriate luminosity and MFs (black data points; x-errors indicate the redshift intervals of the luminosity and MFs). The right-hand panels display the differential evolution of SLSN-I host galaxies after detrending. Each data set was fitted with the linear model $Y = A + B\log(1 + z)$. The curves represent the best fit and the shaded regions the 1σ error contour. The slopes of the best fits are displayed at the bottom of the panels. Note the significant change in the redshift evolution of the FUV and *B*-band luminosity after detrending, while the evolution of the galaxy mass remains unchanged.

Table 6. Redshift evolution of SLSN-I host galaxies.

Property	Linear correlation		Linear model	
	r	$p_{\rm ch}$	Slope	Intercept
	Before removing the cosmic evolution of SF galaxies			
Mass	$0.52^{+0.13}_{-0.18}$	7.7×10^{-5}	$3.00^{+0.81}_{-0.89}$	$7.68^{+0.30}_{-0.31}$
$M_{\rm FUV}$	$-0.53^{+0.13}_{-0.10}$	4.0×10^{-5}	$-7.17^{+1.57}_{-1.37}$	$-15.63^{+0.53}_{-0.50}$
$M_{\rm B}$	$-0.59^{+0.13}_{-0.10}$	3.5×10^{-6}	$-8.08^{+1.64}_{-1.35}$	$-16.28^{+0.41}_{-0.40}$
	After removing the cosmic evolution of SF galaxies			
Mass	$0.51^{+0.14}_{-0.18}$	1.1×10^{-4}	$2.92^{+0.89}_{-0.88}$	$7.68^{+0.29}_{-0.31}$
$M_{\rm FUV}$	$-0.24^{+0.14}_{-0.13}$	7.7×10^{-2}	$-2.83^{+1.62}_{-1.58}$	$-16.04^{+0.46}_{-0.44}$
$M_{\rm s}$	$-0.32^{+0.15}_{-0.13}$	2.1×10^{-2}	$-3.66^{+1.63}_{-1.37}$	$-16.28^{+0.41}_{-0.40}$

Note. The two sets of fits show the redshift evolution before and after correction for global trends of SF galaxies. The columns of the linear correlation analysis display the linear correlation coefficient r, and the corresponding chance probability $p_{\rm ch}$. The redshift evolution is parametrized with the linear model $Y = A + B\log(1 + z)$.

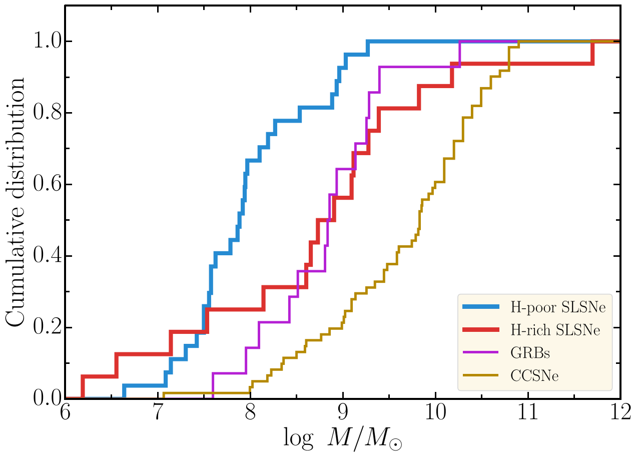

Figure 11. Cumulative histograms of the stellar-mass distributions of various galaxy samples at $z < 0.5$. SLSNe-I show a strong preference for the least massive hosts, even compared to GRBs. The mass distribution of H-rich SLSNe and GRBs is similar and skewed by 0.6 dex to higher masses than the SLSN-I sample. The SN sample was taken from Stoll et al. (2013).

5.2 Metallicity bias

5.2.1 *Dependence of SLSN formation on host galaxy mass*

To quantify the effect of the physical parameters of SLSN host galaxies on SLSN formation, we contrast the galactic environments of SLSN explosions to those of SF galaxies in general. In addition to our SLSN host data, we hence require a census of cosmic star-formation in the respective redshift range as complete as possible. Fortunately, numerous deep-field photometric galaxy surveys compiled in recent years provide a good match to our SLSN imaging data.

The deepest surveys that probe a sufficient cosmic volume are COSMOS (Scoville et al. 2007) and CANDELS (Grogin et al. 2011); both have high completeness levels for galaxies above stellar masses of $M_\star \gtrsim 10^8\,\mathrm{M}_\odot$ at $z \sim 0.5$ (e.g. Tomczak et al. 2014). However, this is still two orders of magnitude higher than our least massive SLSN hosts (Table 4). None the less, we extrapolate the MFs to the lowest observed galaxy masses ($M \sim 10^6\,\mathrm{M}_\odot$). This extrapolation will add some uncertainty, but mass and luminosity functions of SF galaxies are rather well constrained and show no hints for plunging at the faint-end.

The primary parameter that we are interested in is galaxy stellar mass $M_\star$, because it is known to correlate well with the average galaxy metallicity. Metallicity, in turn, has a strong effect on the evolution of massive stars through line-driven stellar winds. Similar considerations have previously been applied to GRB hosts, where after a long debate, the impact of metallicity on long GRB-selected galaxies is now relatively robustly established (e.g. Krühler et al. 2015; Schulze et al. 2015; Vergani et al. 2015; Perley et al. 2016c).

In addition to galaxies from wide-field surveys, we also compare the mass distribution of our SLSN hosts to those of SF galaxies selected through GRBs (Hjorth et al. 2012; Perley et al. 2016a) and low-redshift CCSNe from untargeted surveys (Stoll et al. 2013). The latter is a particularly suitable control sample, as normal CCSNe are thought to trace all SF environments in a relatively direct and unbiased way (Stoll et al. 2013). For simplicity and the sake of clarity, we do not differentiate between CCSNe subtypes.

Fig. 11 shows the cumulative histograms of stellar masses for the four kinds of transients at $z < 0.5$. Clearly, SLSNe-I trace the least massive systems. The median stellar mass increases towards GRB hosts and galaxies selected by more frequent regular CCSNe (Fig. 11). An AD test between GRB and SLSN-I host galaxies at $z < 0.5$ rejects the notion that long GRBs and SLSN-I have similar host mass distributions ($p_{\mathrm{ch}} < 8 \times 10^{-4}$). Moreover, at $z < 1.0$, none of the SLSN-I hosts in our sample of 41 events has a stellar mass above $10^{10}\,\mathrm{M}_\odot$, whereas ∼40 per cent of CCSNe form in such massive galaxies. Thus, it is immediately obvious that a strong effect prevents SLSN-I from forming in galaxies of high stellar mass.

SLSN-IIn hosts are 0.8 dex more massive than SLSN-I hosts, as noted previously in Leloudas et al. (2015c) and Perley et al. (2016b). Their mass distribution is comparable to the GRB hosts (within the limited number statistics). Here, we also find a lack of massive hosts above $10^{10}\,\mathrm{M}_\odot$, though the metallicity dependence is weaker.

5.2.2 *SLSNe are biased tracers of SFR*

Under the working hypothesis that massive stars are the progenitors of SLSNe, they should also trace star formation in a particular way. However, previous experience with GRB hosts has illustrated that environmental factors, most commonly attributed to a low progenitor metallicity, can have a significant effect (e.g. Graham & Fruchter 2013; Schulze et al. 2015; Perley et al. 2016b). This effect is presumably even stronger in SLSN-selected galaxies, considering their mass distributions (Fig. 11).

To better illustrate the efficiency of SLSN production with host stellar mass (or metallicity), we need to normalize the number of SLSN-selected galaxies by the contribution of similar massive systems to the cosmic star formation at the given redshifts. We derive this by starting with the stellar MF $\Phi(M)\mathrm{d}M$ of SF galaxies from CANDELS. This yields the number density of galaxies per stellar-mass bin. We use the parametrization of Φ for SF galaxies from table 2 of Tomczak et al. (2014) and note that the stellar MFs from Ilbert et al. (2013) or Muzzin et al. (2013) are similar and do not alter our conclusions significantly.

Then, we sum the SFR of all contributing galaxies by integrating over the scatter of all galaxies in the galaxy main sequence at a given stellar mass (e.g. Whitaker et al. 2012; Sobral et al. 2014; Speagle et al. 2014; Tasca et al. 2015). The SFR-weighted mass histogram, shown in Fig. 12 in yellow, peaks at around $10^{9.5-10.5}\,\mathrm{M}_\odot$, and provides a good match to the sample of host galaxies of CCSN selected from untargeted surveys. In contrast, the mass histogram of SLSN-hosting galaxies peaks two orders of magnitudes lower, which is clearly inconsistent with the typical environments where the bulk of the stars are produced at $z \sim 0.5$.

5.2.3 *SLSNe production efficiency*

We modelled the SLSN-I host stellar-mass histogram by applying a function that describes an efficiency $\rho(M)$ of producing SLSNe from star formation. We chose $\rho(M)$ as an exponential function in the form of $\rho = \exp\,(-\beta\, M/M_0)$, where M_0 is a characteristic cut-off mass, where the production efficiency dropped to $1/e$, and β a cut-off strength. This essentially shuts off SLSN production in galaxies of high stellar mass. Physically, this can be interpreted as a decrease in the probability of creating SLSNe-I from massive stars above a characteristic cut-off metallicity, where we assume that stellar mass at a given SFR relates to host metallicity at stellar masses below $\sim 10^{10}\,\mathrm{M}_\odot$ (e.g. Maiolino et al. 2008; Yates, Kauffmann & Guo 2012).

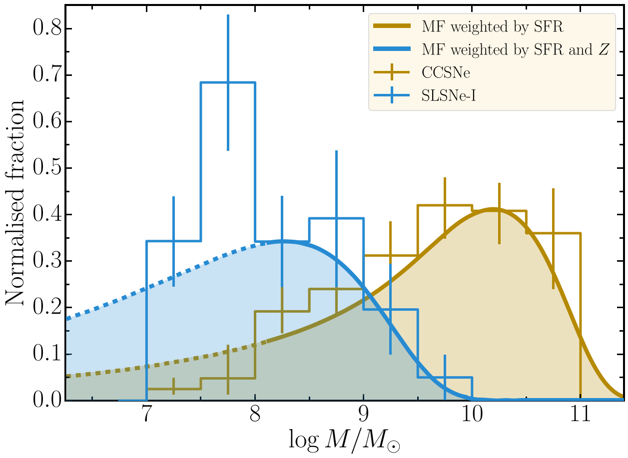

Figure 12. Histogram of the mass distribution of SLSN-I host galaxies and hosts of CCSNe from the Stoll et al. (2013) sample at $z < 1$. The area of each histogram is normalized to unity. The yellow curve shows the SFR-weighted CANDELS. This model describes the observed distribution for CCSNe reasonably well. To match the distribution of H-poor SLSN host galaxies, a further weighting is required that stifles the SLSN production in high-mass galaxies. This mass-dependent (i.e. metallicity dependent) production efficiency can be modelled by an exponential metallicity cut-off at $12 + \log \mathrm{O/H} = 8.31^{+0.16}_{-0.26}$ (blue curve). The dashed lines of the model fits indicate the mass regime where the CANDELS MF had to be extrapolated.

We minimize the deviation between model and data by varying M_0 and β using an MC method on 10^5 bootstrapped distributions of SLSN-I host masses derived from our parent sample. Statistical errors on host masses are included in the procedure by varying them according to the uncertainties in Table 4 within each trial. The best-fitting model is obtained at M_0 corresponding to $12 + \log(\mathrm{O/H})_0 = 8.31^{+0.16}_{-0.26}$ and $\beta = 2.1$. While our procedure can constrain $12 + \log(\mathrm{O/H})_0$ relatively accurately, the cut-off shape is not yet well measured. Acceptable fits are obtained in a range between $\beta = 1$ and $\beta > 30$, where the latter illustrates an infinitively sharp cut-off at $12 + \log(\mathrm{O/H})_0 = 8.4$. Of course, the parameters M_0 and β are not fully independent. The higher the cut-off mass, the sharper the cut-off. Fig. 13 shows the best fit and a region which contains 68 per cent of all MC trials.

For comparison, we modelled the mass distribution of our GRB host galaxy sample with the same model (purple curve in Fig. 13). Its mass distribution points to a higher metallicity cut-off at $12 + \log(\mathrm{O/H})_0 \sim 8.6 \pm 0.10$ (i.e. a 0.3 dex larger oxygen abundance than SLSN-I host galaxies), in agreement with Krühler et al. (2015) and marginally lower than Perley et al. (2016b).

For SLSNe-II, number statistics are still too low to derive robust constraints, but the host mass distribution indicates a behaviour similar to that observed for GRB hosts.

5.3 On the factors behind forming H-poor SLSNe

In the first paper of our series (Leloudas et al. 2015c), we showed that the metallicities (directly measured from spectra) of SLSN-I hosts were low (median value being 0.27 solar metallicity). They were modestly lower than those of GRB hosts, although the difference was statistically insignificant. What is even more striking in the case of SLSNe-I is that their host spectra exhibit emission lines with very large rest-frame EWs. In ≈50 per cent of the cases, we observed rest-frame EWs exceeding 100 Å and in some extreme cases reaching up to 500–800 Å.

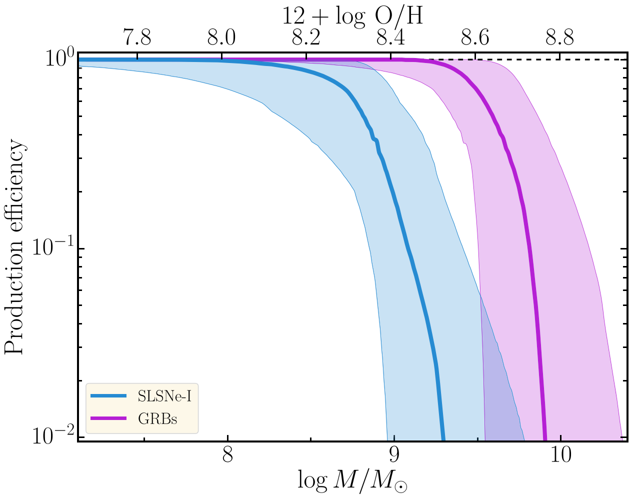

Figure 13. Production efficiency of H-poor SLSNe in galaxies with stellar mass M. Applying the mass–metallicity relation in Mannucci, Salvaterra & Campisi (2011) maps a given mass of a galaxy with a given metallicity. The shaded regions show the 1σ uncertainty. For comparison, the GRB production efficiency is displayed. The production of SLSN progenitors must be stifled in galaxies with metallicity above $12 + \log \mathrm{O/H} = 8.31^{+0.16}_{-0.26}$, 0.3 dex lower than for GRBs, indicating that SLSN progenitors are on average less metal-enriched than GRBs.

The presence of EELGs in our sample is extremely unusual (only 1 per cent of galaxies in the zCOSMOS survey have rest-frame EW >100 Å; Amorín et al. 2015), and we determined that their frequency could not be a chance coincidence ($p_{\mathrm{ch}} \sim 10^{-12}$; Leloudas et al. 2015c). On average, even GRB hosts do not show such strong emission lines. The difference to the distribution of a complete sample of GRBs at $z < 1$ (Hjorth et al. 2012) was found to be statistically significant, although the strongest emitters in our sample were mostly found at $z < 0.3$. The difference was even more pronounced in [O III] λ5007 than in H α, pointing to a higher ionization fraction in the gas around SLSNe.

These extreme properties were also seen by directly measuring the ionization parameter q and the ratio between [N II]/H β and [O III] λ5007/H α (BPT diagram; Baldwin, Phillips & Terlevich 1981), where the overwhelming majority of H-poor SLSNe were found to be in regions with log [O III] /H β > 0.5. As the EWs of the lines decrease with time after a starburst (e.g. Leitherer et al. 1999), this evidence strongly points towards very young environments for SLSN-I hosts.[14] This led us to propose that the progenitors of H-poor SLSNe are very young, and are on average more short-lived than those of GRBs (Leloudas et al. 2015c). Although absolute ages are notoriously difficult to determine, we identified a very young stellar population with an age of only ∼3Myr at the explosion site of PTF12dam, which is the most extreme example in our sample (in terms of emission-line strength; Thöne et al. 2015).

Recently, Chen et al. (2016) questioned the importance of young age for H-poor SLSN progenitors, proposing that metallicity is the only key factor leading to the production of SLSNe. These authors approximated the effect of age through the sSFR and by comparing the parameter spaces of their SLSN host samples in the metallicity–sSFR plane to complete samples of SF galaxies in

---

[14] The relation between the H β EW and the age of the starburst also has a dependence on metallicity (Inoue 2011) and the shape of the SFHs (e.g. Terlevich et al. 2004; Lee et al. 2009).

the *local volume* (11HUGS and LVL; Kennicutt et al. 2008; Lee et al. 2011). However, the two properties are intimately connected through the mass–metallicity–SFR fundamental relation (Mannucci et al. 2011) and can therefore not be easily disentangled. Thus, we expect to see metallicity and age to drive the SLSN production. Attributing the dependence of H-poor SLSNe simply on metallicity has led many authors (e.g. Lunnan et al. 2014; Chen et al. 2016) to support a magnetar origin for these explosions, although this explanation is not unique. Acknowledging that young age plays an important role as well allows models based on more massive progenitors to remain equally competitive (Leloudas et al. 2015c; Thöne et al. 2015).

In contrast to Leloudas et al. (2015c), Perley et al. (2016b) argued that the fraction of starbursts (defined as sSFR $> 10^{-8}$ yr^{-1} in their papers) among SLSN-I hosts is not exceptionally large and that the starburst fraction among H-poor SLSN hosts may be explained by the fact that dwarf galaxies tend to have bursty SFHs (e.g. Guo et al. 2016). By using the study of Lee et al. (2009), we show that the fraction of SLSNe-I occurring in EELGs in the Leloudas et al. (2015c) sample is significantly increased, even with respect to dwarf galaxies. Lee et al. (2009) determined the fraction of starbursts among local dwarfs in the 11HUGS survey, which is the same survey that Perley et al. (2016b) and Chen et al. (2016) used as their main comparison galaxy sample. Furthermore, Lee et al. (2009) used the same operational definition of starburst that we use for EELGs ($\mathrm{EW}_{\mathrm{rest}} > 100$ Å), making a direct comparison straightforward. They determined that only 6 per cent of dwarf galaxies in the absolute magnitude range of interest ($-19 < M_{\mathrm{B}} < -15$) have $\mathrm{EW}_{\mathrm{rest}} > 100$ Å (and only 8 per cent have $\mathrm{EW}_{\mathrm{rest}} > 80$ Å). This means that the probability of attaining the same fraction of EELGs among H-poor SLSN hosts as in Leloudas et al. (2015c) by chance is $p_{\mathrm{ch}} < 10^{-6}$. This might be larger than what is obtained by comparing with zCOSMOS ($p_{\mathrm{ch}} \sim 10^{-12}$), but a chance coincidence is still extremely unlikely. This can also be understood in the following way: if the duty cycles in the bursty SFH of dwarf galaxies are 1–2 Gyr, it is very unlikely that we would happen to catch them by chance so close to an initial starburst, when selecting them through H-poor SLSNe.

We therefore argue that *both* low metallicity *and* young age play important roles in the formation of H-poor SLSNe, and that stellar evolution in metal-poor, starburst environments needs to be better understood to fully appreciate the context. In particular, mass loss in these extreme regimes is poorly understood and more effort needs to be put into understanding why these explosions are H-poor and whether this can be attributed to eruptive mass loss (Woosley et al. 2007; Quataert & Shiode 2012), homogeneous evolution (Yoon & Langer 2005), binarity (Eldridge, Izzard & Tout 2008) or another, yet unknown, factor.

5.4 SLSN host galaxies in the context of other galaxy populations

In the previous sections, we discussed particular aspects of the host populations. In the following, we compare the host properties to those of other galaxy samples.

5.4.1 SLSN-I host population

Hydrogen-poor SLSNe are preferentially found in blue low-mass dwarf galaxies with high sSFR and metallicities of $<0.4\,\mathrm{Z}_{\odot}$. These properties are similar to those of EELGs and GRB host galaxies. This sparked a long-standing debate on how strong the similarities actually are (e.g. Lunnan et al. 2014; Chen et al. 2015; Leloudas et al. 2015c; Angus et al. 2016; Japelj et al. 2016). The answer to this question was not only of interest to compare the galaxy populations, but also to draw conclusions on the progenitors of GRBs and SLSNe (see previous section) and even to propose similarities in the energy source powering these two stellar explosions.

Previous studies were limited to small samples (∼10 objects) or even to the comparison with galaxy samples at different redshifts. In some cases, selection criteria were introduced that led to non-random sampling of distribution functions, such as excluding GRB and SLSN host galaxies without *K*-band observations (Japelj et al. 2016).[15] Given the size of our GRB and SLSN samples (>50 objects each; Table 2), we attempt to provide a new perspective on this conundrum and to how SLSN hosts compare to other galaxy samples. We divide our samples into two redshift intervals: $0.3 \leq z \leq 1.0$ and $1.0 \leq z \leq 2.0$. Each of these intervals covers a look-back-time interval of 2.6–4.4 Gyr, which is a compromise between minimizing the impact of the general cosmic evolution of SF galaxies and maximizing number statistics. For the GRB sample, we also modelled the SEDs with the same assumptions and the same software as for the SLSN host galaxies, to minimize systematic errors.

To assess the differences, we apply two distinct tests. We use two-sided AD tests to ascertain differences in the distribution functions, and we quantify the frequency of how often the estimator of the mean mass and SFR of SLSN-I host galaxies can be obtained from the comparison samples by chance (2D test; for details see Section 3.4). While an AD test compares distribution functions, the 2D test compares multiple parameters at the same time, namely SFR, mass, and indirectly the sSFR. Therefore, its outcome is less sensitive to the selected properties. The 2D tests are, however, limited to mean values. We reject the null hypothesis that two distributions are statistically similar, if the chance probability is $p_{\mathrm{ch}} < 10^{-2}$ for a given test.

Fig. 14 summarizes the *p* values of the AD tests for five different properties (*B*-band luminosity, $R - K_{\mathrm{s}}$ colour, mass, SFR, and sSFR). The AD tests between distributions of SLSN-I and GRB hosts reveal low *p* values between 2×10^{-4} (*B*-band luminosity) and 0.01 (SFR). The statistical tests in the mass–SFR plane, displayed in Fig. 15, corroborate these results. The chance probability to extract an estimator from the GRB sample with a mean mass and SFR similar to SLSN-I hosts is $\sim 10^{-3}$ (equivalent to 3.3σ). Therefore, we reject the null hypothesis that GRB and SLSN host galaxies are statistically similar. We stress that revealing these differences requires large and homogenous samples, like the one presented in this paper, which were not available in previous studies.

Leloudas et al. (2015c) ignited the SLSN–EELG connection by unravelling a high incidence rate of hosts with intense [O III] emission and ionization conditions comparable to EELGs for our spectroscopy sample. The comparison between properties of the stellar component is less straightforward. The statistical tests point to similarities with 3D-*HST* EELGs at $1 < z < 2$ ($p_{\mathrm{ch}} \sim 0.03$–$0.16$), but to weaker similarities with VUDS EELGs ($p_{\mathrm{ch}} \lesssim 0.01$–$0.09$) and even stark differences to zCOSMOS EELGs ($p_{\mathrm{ch}} < 10^{-5}$) at lower redshift (Figs 14 and 15).

These findings can be reconciled with the definition of EELGs and how they are identified in galaxy surveys. EELGs are defined

---

[15] For example, ∼30 per cent of our SLSN hosts at $z < 1$ are too faint to obtain meaningful K_{s}-band constraints, even with the most efficient instruments.

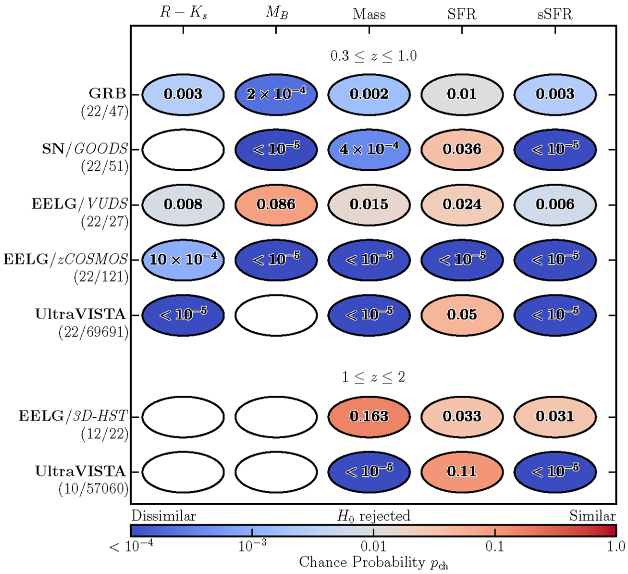

Figure 14. Two-sided AD tests between SLSN-I host galaxies and different galaxy samples at $0.3 \leq z \leq 1.0$ and $1 \leq z \leq 2$. The p are reported in the ellipses. The diverging colour scheme is centred at the p-value of 0.01, where we reject the null hypothesis that the two samples have the same parent distribution. For all tests, we required that the redshift distributions are similar ($p_{\mathrm{ch}} > 0.01$) and that each sample consists of at least nine objects. The size of the SLSN-I host sample (first) and of the galaxy sample (last) are given below each sample.

spectroscopically by $\mathrm{EW_{rest}}([\mathrm{O\,III}]\lambda5007) > 100$ Å (a measure of the recent star formation activity normalized to the light from all stars). Furthermore, the VUDS EELGs were originally pooled from a galaxy sample with a brightness of $25 < I(\mathrm{AB}) < 23$, whereas the zCOSMOS sample was limited to bright and therefore more massive EELG candidates [I(AB) < 22 mag; Tables 2 and D1]. In contrast, the average R-band brightness of SLSN-I hosts at $0.3 < z < 1.0$ is ∼24.6 mag, similar to VUDS EELGs but >2.5 mag fainter than the I-band magnitude limit of the zCOSMOS sample. This immediately explains why the properties of the stellar component of SLSN-I host galaxies and zCOSMOS EELGs are so distinct. The stellar component in SLSN-I host galaxies is more similar to VUDS EELGs, though the statistical tests are inconclusive as to whether they are indeed statistically similar or distinct. Differences between the stellar components of SLSN-I host galaxies and EELG samples are expected because the properties of the ionized gas for a larger number of SLSN-I hosts is not as extreme as that of EELGs. Furthermore, the different EELG samples show that this ephemeral and transformative phase in galaxy evolution is observed in galaxies over a wide range of masses.

The AD and the 2D tests (Figs 14 and 15) show that the properties of the SLSN-I host population are more extreme and in stark contrast to the general population of SF galaxies in the UltraVISTA survey and the hosts galaxies of regular CCSNe from the GOODS survey.

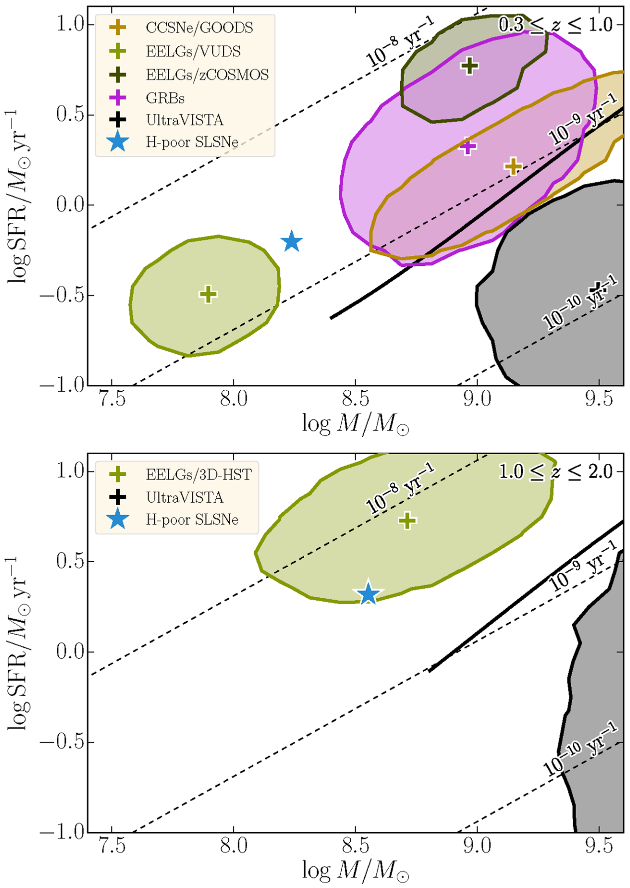

Figure 15. Statistical tests in the mass–SFR plane between SLSN-I host galaxies and various galaxy samples at $0.3 \leq z \leq 1.0$ (top) and $1 \leq z \leq 2$ (bottom). The mean mass and SFR of the SLSN-I hosts is indicated by the '⋆'. To assess how SLSN-I hosts differ from other galaxy samples, we bootstrap each galaxy sample 30 000 times, randomly draw 22 objects (the size of the SLSN-I host sample), and compute the mean SFR and mass. The barycentre of each distribution is indicated by a '+'. For the sake of clarity, these values are not displayed for the UltraVISTA sample. The shaded areas display the regions that encompass 99 per cent of all realizations. The mean SFR and the mean mass of SLSN-I host galaxies cannot be generated from random subsamples of the GRB, EELG, and UltraVISTA samples at $z < 0.3$. At $0.3 < z < 1.0$, the mean SFR and mean mass can be generated from random subsamples of the 3D-*HST* EELG sample. The dashed lines show curves of constant sSFR. The thick line shows the galaxy main sequence.

5.4.2 SLSN-IIn host population

The host population of SLSNe-IIn is characterized by a rich diversity: (i) the mass and luminosity distributions have dispersions that are a factor of 1.5–2 larger compared to any other class of SF galaxies discussed in this paper; (ii) hosts with stellar masses of more than $10^{10}\,\mathrm{M}_\odot$ are scarce, despite the large dispersion in galaxy mass; (iii) the $R - K_s$ colour has a mean and a dispersion that is similar to SF galaxies; and (iv) the sSFRs are shifted by 0.6 dex towards higher sSFR with respect to the main sequence of SF galaxies in the mass–sSFR plane (Fig. 9).

The large dispersion measurements are difficult to map to a single progenitor system of SLSNe-IIn. Type IIn SNe are primarily powered by the interaction of the SN ejecta with the CSM expelled prior to explosion. If the interaction is strong, the signature of the original SN gets washed out. In the most extreme cases of CSM interaction, even different types of CCSNe as well as thermonuclear Type Ia SNe could give rise to Type IIn SNe (e.g. Leloudas et al. 2015a). The fact that all hosts show evidence for recent star formation and have very high sSFRs suggests that the contamination by Type Ia SNe is low. This implies that the diversity is primarily due to different progenitor channels (see also Angus et al. 2016).

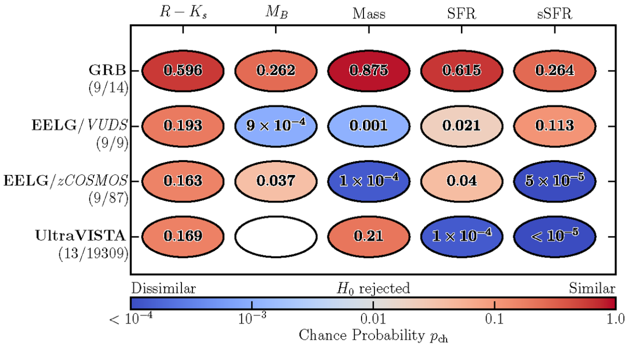

Figure 16. Two-sided AD tests between SLSN-IIn host galaxies and different galaxy samples at $z < 0.5$ (similar to Fig. 14). The sizes of the SLSN-IIn host sample (first) and of the galaxy sample (last) are given below each sample.

Similar to the SLSN-I host population, we perform AD tests and the tests (Fig. 16) in the mass–SFR plane (Fig. 17) to put the SLSN-IIn host population in context with other galaxy samples. Despite the limited number statistics, the SLSN-IIn host population is clearly distinct from the general population of SF galaxies in the UltraVISTA survey. While the distribution functions are broader than those of other galaxy samples, the lack of massive hosts suggests some dependence on environment properties. The similarities of the distribution functions to GRBs as well as the locus in the mass–SFR plane suggests that their hosts are similar. The lack of massive host galaxies would suggests a stifled production efficiency at metallicities higher than $Z \sim 0.8\,Z_\odot$, the metallicity above which the GRB production efficiency is significantly reduced (Section 5.2.3). However, the small number of SLSN-IIn in conjunction with their rich diversity precludes drawing a firm conclusion, yet.

5.4.3 *SLSN-II host population*

The family of Type II SLSNe is the rarest class among SLSNe. In constrast to SLSN-IIn, the emission of SLSNe-II is not powered by strong interaction of the SN ejecta with the CSM. Only three events among the 29 H-rich SLSNe known today belong to this class.[16] Their host properties seem to be distinct from the average properties of the SLSN-IIn family. Type II SLSNe occupy the lower to bottom half of the distribution functions. Two of three hosts are even among the least massive galaxies in our sample (10^6–$10^7\,M_\odot$). Those masses are comparable to the least massive dwarf galaxies in the local Universe. According to the parametrization of the mass–metallicity relation in Andrews & Martini (2013), their masses point to galaxies with metallicity of $\lesssim 0.3\,Z_\odot$.

Intriguingly, Yan et al. (2015, 2017) revealed that an increasing number of SLSNe-I showed episodic hydrogen emission at late phases. The properties of these hydrogen emission lines are similar to those of CSS121015, SN2008es, and SN2013hx. Yan et al. (2015, 2017) attributed this feature to pulsational instabilities, where the outer H-rich envelope is expelled during a violent mass-loss episode. As the SN ejecta traverses the CSM, shocks between the ejecta and the CSM produce episodic hydrogen emission. Alternatively, these authors proposed that the progenitor retained a thin layer of hydrogen where recombination lines emerge only after the SN ejecta cooled down. Hence, it is possible that SLSNe-II are more closely connected to SLSNe-I.

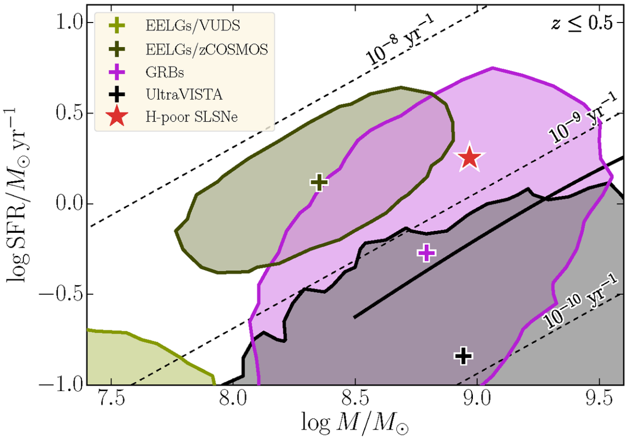

Figure 17. Statistical tests in the mass–SFR plane between SLSN-IIn host galaxies and various galaxy samples at $z < 0.5$ (similar to Fig. 15). The mean mass and mean SFR of the SLSN-IIn host sample (indicated by '$\star$') can be generated by random subsamples of the GRB sample, but is inconsistent with the EELG and UltraVISTA samples.

Inserra et al. (2016) noted that the spectroscopic and photometric properties of SN2013hx showed similarities to brighter regular Type II SNe. However, even these brighter regular Type II SNe are still significantly less luminous than SLSNe. It is not clear how stars with an extended hydrogen envelope could produce such high luminosities. Larger samples are needed to better understand how the SLSN II population compares to different classes of SNe and SLSNe.

5.5 Selection biases

Our conclusions could be affected by various selection biases, such as publication bias, target selection bias and classification bias. Moreover, the SUSHIES sample is compiled from different SN surveys, which makes it even more difficult to quantify the effective bias.

To examine whether our sample has the same level of bias as the PS1 and PTF samples, we perform two-sided AD tests between the distributions of the host properties. If the probability of randomly drawing a distribution from the PS1/PTF samples, which is at least as extreme as the SUSHIES sample, is larger than 1 per cent, we reject the hypothesis that the level of bias in SUSHIES is different from the PS1 and PTF samples. For a fair comparison, we remove common objects and split our sample into two redshift intervals to take the redshift domains of the PS1 and the PTF samples into account: $z < 0.5$ for the PTF sample and $z > 0.5$ for the PS1 sample.

The AD tests between the B-band luminosity, mass and SFR distributions of 20 SLSN-I hosts from our sample and 16 SLSN-I hosts from the PTF sample give a high chance probability of agreement of >19 per cent. For SLSN-II/IIn hosts, the chance probability of >27 per cent is even substantially higher (SUSHIES: 13 objects and PTF: 14 objects). A similar result can be obtained from the comparison with the PS1 sample ($p_{\rm ch}$ > 8 per cent; SUSHIES: 11 objects and PS1: 15 objects).

In conclusion, the heterogeneous SUSHIES sample has a similar effective bias to the PS1 and the PTF samples. A detailed discussion

---

[16] This number was compiled from the sample presented here and in Perley et al. (2016b), and also includes two H-rich SLSNe that were reported in the literature but not discussed in these papers.

about possible selection effects biasing the PS1 and PTF samples is presented in Lunnan et al. (2014) and Perley et al. (2016b).

6 SUMMARY

We present the photometric properties of 53 H-poor and 16 H-rich SLSNe, detected before 2015 and publicly announced before mid-2015. Among those are four new SLSNe (two of each type), found in the ASIAGO SN catalogue, with a peak luminosity significantly brighter than $M_{\rm V} = -21$ mag. Each host is a target of deep imaging campaigns that probe the rest-frame UV to NIR. In addition, we incorporate radio data from wide-field surveys and JVLA observations to put limits on the total star formation activity. By modelling the SEDs, we derive physical properties, such as mass, SFR, and luminosity, and build distribution functions to ascertain the influence of these properties on the SLSN population. Our main conclusions are:

(i) H-poor SLSNe are preferentially found in very blue low-mass dwarf galaxies. Their sSFRs are on average 0.5 dex larger compared to the main sequence of SF galaxies and they populate a part of the sSFR–mass parameter space that is typically occupied by EELGs.

(ii) The host population of SLSNe-IIn shows very complex properties: (1) the mass and luminosity distributions have dispersions that are a factor of 1.5–2 larger compared to all comparison samples; (2) the $R - K_{\rm s}$ colour has a mean and a dispersion which is similar to SF galaxies; and (3) the sSFRs are on average a factor of 10 larger than of regular SF galaxies discussed in this paper. These properties argue for a massive star origin of all SLSNe-IIn in our sample but to a low dependency on integrated host properties. Because the luminosity of SLSNe-IIn is determined by the strength of the interaction and not by a particular type of stellar explosion, this diversity suggests multiple progenitor channels.

(iii) The hosts of the three Type II SLSNe are at the bottom of any distribution function. Two out of three Type II SLSNe exploded in the least massive host galaxies in our sample (10^6–$10^7\,{\rm M}_{\odot}$). Their hosts are similar to those of H-poor SLSNe. Their preference for low-mass and hence low-metallicity galaxies hints to different progenitors from Type IIn SLSNe. Larger samples are needed to draw a conclusion on this question.

(iv) The scarcity of hosts above $10^{10}\,{\rm M}_{\odot}$ for SLSNe-I and SLSNe-IIn can be attributed to a metallicity bias above which the production efficiency is stifled. Assuming an exponential cut-off, the best-fitting cut-off metallicity of H-poor SLSNe at $z < 1$ is $12 + \log {\rm O/H} = 8.31^{+0.16}_{-0.31}$ ($Z \sim 0.4\,{\rm Z}_{\odot}$), which is 0.4 dex lower than for GRBs. The similarities between the mass distributions of SLSN-IIn and GRB host galaxies suggest a metallicity cut-off at ~0.8 solar metallicity.

(v) A growing population of SLSN hosts have masses between 10^6 and $10^7\,{\rm M}_{\odot}$. Those objects are among the least massive SF galaxies known to date and could represent environments similar to those of starburst galaxies in the early Universe.

(vi) The redshift evolution of the SLSN-I host population is consistent with the general cosmic evolution of SF galaxies. After detrending the data, the galaxy mass shows evidence for differential evolution at 3.8σ confidence, while differential evolution in the B band and FUV luminosity can be excluded at 3σ confidence. The evolution of the mass distribution of SLSN-I hosts is similar to the evolution of the mass–metallicity relation, supporting connecting the dearth of massive hosts to a metallicity bias.

(vii) Multiple statistical tests between the host properties of SLSN-I and GRB host galaxies reveal differences at $>3\sigma$ confidence. H-poor SLSNe are found in less massive (and therefore more metal-poor) hosts than GRBs. To conclusively show that SLSN-I and GRB host galaxies are different on average, large samples with well-sampled SEDs are needed.

(viii) SLSN-I hosts and EELGs show similarities, even in broad-band properties. This suggests that environmental conditions in EELGs play a very important role in the formation of SLSNe-I. We conclude that metallicity is *not* the sole ingredient regulating the SLSN-I production and suggest that a young age plays an important role in the formation of H-poor SLSNe as well.

(ix) The class of H-poor SLSNe comprises of fast- and slow-declining SLSNe. A subsample of 21 SLSNe-I have measured decline time-scales: 14 fast- and 7 slow-declining SLSNe-I. We find no differences between both host populations. However, larger samples of SLSNe with measured decay time-scales are needed to draw a firm conclusion.

(x) No host is detected in wide-field radio surveys. At $z < 0.5$, the 4σ limits on the total SFR are a factor of 20 larger than the SFRs derived from SED modelling, ruling out truly obscured star formation missed by optical diagnostics. This result is consistent with the lack of high-obscured hosts and SLSNe. The deep radio observation of the solar-metallicity host of the H-poor SLSN MLS121104 reveals no difference to the SED-derived SFR.

ACKNOWLEDGEMENTS

We acknowledge with sadness the unexpected passing of our esteemed colleague, co-author, and friend JG. His support of and contributions to this work and astronomy in general are greatly appreciated.

We thank the referee Sandra Savaglio for a careful reading of the manuscript and for lots of helpful comments that improved this paper.

We thank R. Quimby for sharing an explosion image of SN2005ap, P. Vresswijk and D. A. Perley for the host image of PTF13ajg, T.-W. Chen for an SN image of MLS121104, and A. Uldaski for an SN image of SN2003ma. SS thanks P. Pietrukowicz, D. Whalen, and A. Gal-Yam for fruitful discussions.

SS acknowledges support from the CONICYT-Chile FONDECYT Postdoctorado fellowship 3140534 and the Feinberg Graduate School. SS and FEB acknowledge support from Basal-CATA PFB-06/2007, and Project IC120009 ‘Millennium Institute of Astrophysics (MAS)’ of Iniciativa Científica Milenio del Ministerio de Economía, Fomento y Turismo. TK acknowledges support through the Sofja Kovalevskaja Award to P. Schady from the Alexander von Humboldt Foundation of Germany. AdUP and CT acknowledge support from the Ramón y Cajal fellowships and the Spanish Ministry of Economy and Competitiveness through project AyA2014-58381-P. RA acknowledges support from the European Research Council Advanced Grant 695671 ‘QUENCH’.

This paper is based partly on observations made with: ESO Telescopes at the La Silla Paranal Observatory; the 6.5-m Magellan Telescopes located at the Las Campanas Observatory, Chile; the GTC), installed in the Spanish Observatorio del Roque de los Muchachos of the Instituto de Astrofísica de Canarias, in the island of La Palma; the CAHA at Calar Alto, Spain, operated jointly by the Max-Planck Institut für Astronomie and the Instituto de Astrofísica de Andalucía (CSIC); the Nordic Optical Telescope, operated by the Nordic Optical Telescope Scientific Association at the Observatorio del Roque de los Muchachos, La Palma, Spain, of the Instituto de Astrofísica de Canarias; and Karl G. JVLA, New Mexico, United States of

America. This research draws upon data provided by Cypriano as distributed by the National Optical Astronomy Observato (NOAO) Science Archive. NOAO is operated by the Association of Universities for Research in Astronomy (AURA) under a cooperative agreement with the National Science Foundation. This publication makes use of data products from the *WISE*, which is a joint project of the University of California, Los Angeles, and the Jet Propulsion Laboratory/California Institute of Technology, funded by the National Aeronautics and Space Administration. *GALEX* (Galaxy Evolution Explorer) is a NASA Small Explorer, launched in 2003 April. We gratefully acknowledge NASA's support for construction, operation, and science analysis for the *GALEX* mission, developed in cooperation with the Centre National d'Etudes Spatiales of France and the Korean Ministry of Science and Technology. Based in part on data collected at the Subaru Telescope, Hawaii, United States of America, which is operated by the National Astronomical Observatory of Japan. The NRAO) is a facility of the National Science Foundation operated under cooperative agreement by Associated Universities, Inc. Part of the funding for GROND was generously granted from the Leibniz-Prize to Prof G. Hasinger (DFG grant HA 1850/28-1).

Funding for SDSS-III has been provided by the Alfred P. Sloan Foundation, the Participating Institutions, the National Science Foundation, and the U.S. Department of Energy Office of Science. The SDSS-III web site is http://www.sdss3.org/. SDSS-III is managed by the Astrophysical Research Consortium for the Participating Institutions of the SDSS-III Collaboration, including the University of Arizona, the Brazilian Participation Group, Brookhaven National Laboratory, University of Cambridge, Carnegie Mellon University, University of Florida, the French Participation Group, the German Participation Group, Harvard University, the Instituto de Astrofísica de Canarias, the Michigan State/Notre Dame/JINA Participation Group, Johns Hopkins University, Lawrence Berkeley National Laboratory, Max Planck Institute for Astrophysics, Max Planck Institute for Extraterrestrial Physics, New Mexico State University, New York University, Ohio State University, Pennsylvania State University, University of Portsmouth, Princeton University, the Spanish Participation Group, University of Tokyo, University of Utah, Vanderbilt University, University of Virginia, University of Washington, and Yale University. Based on observations obtained with MegaPrime/MegaCam, a joint project of CFHT and CEA/IRFU, at CFHT, which is operated by the National Research Council (NRC) of Canada, the Institut National des Science de l'Univers of the Centre National de la Recherche Scientifique (CNRS) of France and the University of Hawaii. This work is partly based on data products produced at Terapix available at the Canadian Astronomy Data Centre as part of the CFHTLS, a collaborative project of NRC and CNRS.

This project used public archival data obtained withthe Dark Energy Camera by the Dark Energy Survey (DES). Funding for the DES Projects has been provided by the DOE and NSF (USA), MISE (Spain), STFC (UK), HEFCE (UK), NCSA (UIUC), KICP (U. Chicago), CCAPP (Ohio State), MIFPA (Texas A&M), CNPQ, FAPERJ, FINEP (Brazil), MINECO (Spain), DFG (Germany), and the collaborating institutions in the DES, which are Argonne Lab, UC Santa Cruz, University of Cambridge, CIEMAT-Madrid, University of Chicago, University College London, DES-Brazil Consortium, University of Edinburgh, ETH Zürich, Fermilab, University of Illinois, ICE (IEEC-CSIC), IFAE Barcelona, Lawrence Berkeley Lab, LMU München and the associated Excellence Cluster Universe, University of Michigan, NOAO, University of Nottingham, Ohio State University, University of Pennsylvania, University of Portsmouth, SLAC National Lab, Stanford University, University of Sussex, and Texas A&M University.

This research has made use of the NASA/IPAC Infrared Science Archive, which is operated by the Jet Propulsion Laboratory and the California Institute of Technology, under contract with the National Aeronautics and Space Administration.

This research made use of ASTROPY (Robitaille et al. 2013), MATPLOTLIB (Hunter 2007), NUMPY (van der Walt, Colbert & Varoquaux 2011) and SCIPY (Jones et al. 2001). The results in this paper were obtained using R version 3.3.2 with the packages KSAMPLES version 1.2.4. R itself and all packages used are available from the Comprehensive R Archive Network (CRAN) at http://CRAN.R-project.org/.

REFERENCES

Adami C. et al., 2006, A&A, 451, 1159
Agnoletto I., 2010, PhD thesis, Universitá degli Studi di Padova
Aihara H. et al., 2011, ApJS, 193, 29
Amorín R. et al., 2014, A&A, 568, L8
Amorín R. et al., 2015, A&A, 578, A105
Andrews B. H., Martini P., 2013, ApJ, 765, 140
Angus C. R., Levan A. J., Perley D. A., Tanvir N. R., Lyman J. D., Stanway E. R., Fruchter A. S., 2016, MNRAS, 458, 84
Appenzeller I. et al., 1998, The Messenger, 94, 1
Arnouts S., Cristiani S., Moscardini L., Matarrese S., Lucchin F., Fontana A., Giallongo E., 1999, MNRAS, 310, 540
Asplund M., Grevesse N., Sauval A. J., Scott P., 2009, ARA&A, 47, 481
Atek H. et al., 2010, ApJ, 723, 104
Atek H. et al., 2011, ApJ, 743, 121
Baldry I. K. et al., 2012, MNRAS, 421, 621
Baldwin J. A., Phillips M. M., Terlevich R., 1981, PASP, 93, 5
Barbary K. et al., 2009, ApJ, 690, 1358
Barbon R., Buondi V., Cappellaro E., Turatto M., 2010, VizieR Online Data Catalog, 1
Barkat Z., Rakavy G., Sack N., 1967, Phys. Rev. Lett., 18, 379
Becker R. H., White R. L., Helfand D. J., 1995, ApJ, 450, 559
Bell E. F., 2003, ApJ, 586, 794
Benetti S. et al., 2014, MNRAS, 441, 289
Berger E. et al., 2012, ApJ, 755, L29
Bertin E., Arnouts S., 1996, A&AS, 117, 393
Bianchi L., Herald J., Efremova B., Girardi L., Zabot A., Marigo P., Conti A., Shiao B., 2011, Ap&SS, 335, 161
Bisnovatyi-Kogan G. S., Kazhdan Y. M., 1967, SvA, 10, 604
Blanchard P. K., Berger E., Fong W.-F., 2016, ApJ, 817, 144
Blanton M. R., Roweis S., 2007, AJ, 133, 734
Bleem L. E., Stalder B., Brodwin M., Busha M. T., Gladders M. D., High F. W., Rest A., Wechsler R. H., 2015, ApJS, 216, 20
Blinnikov S. I., Sorokina E. I., 2010, preprint (arXiv:1009.4353)
Bock D. C.-J., Large M. I., Sadler E. M., 1999, AJ, 117, 1578
Brammer G. B. et al., 2012, ApJS, 200, 13
Breeveld A. A., Landsman W., Holland S. T., Roming P., Kuin N. P. M., Page M. J., 2011, in McEnery J. E., Racusin J. L., Gehrels N., eds, AIP Conf. Ser., Vol. 1358, Gamma Ray Bursts. Am. Inst. Phys., New York, p. 373
Bruzual G., Charlot S., 2003, MNRAS, 344, 1000
Buchner J. et al., 2014, A&A, 564, A125
Calzetti D., 2013, in Falcón-Barroso J., Knapen J. H., eds, Star Formation Rate Indicators. Cambridge Univ. Press, Cambridge, p. 419
Calzetti D., Armus L., Bohlin R. C., Kinney A. L., Koornneef J., Storchi-Bergmann T., 2000, ApJ, 533, 682
Campbell H. et al., 2014, Astron. Telegram, 6524
Casali M. et al., 2006, in McLean I. S., Iye M., eds, Proc. SPIE Conf. Ser. Vol. 6269, Ground-Based and Airborne Instrumentation for Astronomy. SPIE, Bellingham, p. 62690W
Castander F. J. et al., 2015, Astron. Telegram, 7199
Castellano M. et al., 2014, A&A, 566, A19

Cepa J. et al., 2000, in Iye M., Moorwood A. F., eds, Proc. SPIE Conf. Ser. Vol. 4008, Optical and IR Telescope Instrumentation and Detectors. SPIE, Bellingham, p. 623
Chabrier G., 2003, PASP, 115, 763
Chatzopoulos E., Wheeler J. C., 2012, ApJ, 760, 154
Chatzopoulos E. et al., 2011, ApJ, 729, 143
Chatzopoulos E., van Rossum D. R., Craig W. J., Whalen D. J., Smidt J., Wiggins B., 2015, ApJ, 799, 18
Chen T.-W. et al., 2013, ApJ, 763, L28
Chen T.-W. et al., 2015, MNRAS, 452, 1567
Chen T.-W., Smartt S. J., Yates R. M., Nicholl M., Krühler T., Schady P., Dennefeld M., Inserra C., 2016, MNRAS, 470, 3566
Chevalier R. A., Irwin C. M., 2011, ApJ, 729, L6
Chomiuk L. et al., 2011, ApJ, 743, 114
Christensen E. et al., 2009, CBET, 2106, 1
Condon J. J., 1992, ARA&A, 30, 575
Condon J. J., Cotton W. D., Greisen E. W., Yin Q. F., Perley R. A., Taylor G. B., Broderick J. J., 1998, AJ, 115, 1693
Conroy C., 2013, ARA&A, 51, 393
Cooke J. et al., 2012, Nature, 491, 228
Cucciati O. et al., 2012, A&A, 539, A31
Dessart L., Waldman R., Livne E., Hillier D. J., Blondin S., 2013, MNRAS, 428, 3227
Drake A. J. et al., 2009a, CBET, 1766, 1
Drake A. J. et al., 2009b, Astron. Telegram, 1911
Drake A. J. et al., 2009c, Astron. Telegram, 2359
Drake A. J. et al., 2010, ApJ, 718, L127
Drake A. J. et al., 2011a, ApJ, 735, 106
Drake A. J. et al., 2011b, CBET, 2733, 1
Drake A. J. et al., 2011c, Astron. Telegram, 3324
Drake A. J. et al., 2011d, Astron. Telegram, 3340
Drake A. J. et al., 2012, Astron. Telegram, 4595
Dressler A. et al., 2011, PASP, 123, 288
Eldridge J. J., Izzard R. G., Tout C. A., 2008, MNRAS, 384, 1109
Erben T. et al., 2005, Astron. Nachr., 326, 432
Faber S. M. et al., 2007, ApJ, 665, 265
Fatkhullin T., Gabdeev M., 2012, Astron. Telegram, 4599
Feroz F., Hobson M. P., Cameron E., Pettitt A. N., 2013, preprint (arXiv:1306.2144)
Filippenko A. V., 1997, ARA&A, 35, 309
Foreman-Mackey D., 2016, J. Open Source Softw., 24
Fowler W. A., Hoyle F., 1964, ApJS, 9, 201
Fox O. D. et al., 2015, MNRAS, 454, 4366
Fraley G. S., 1968, Ap&SS, 2, 96
Gal-Yam A., 2012, Science, 337, 927
Gal-Yam A. et al., 2009, Nature, 462, 624
Gehrels N. et al., 2004, ApJ, 611, 1005
Gezari S. et al., 2009, ApJ, 690, 1313
Graham J. F., Fruchter A. S., 2013, ApJ, 774, 119
Graham M. J. et al., 2011a, CBET, 2787, 1
Graham M. J. et al., 2011b, Astron. Telegram, 3477
Graham M. L. et al., 2014, Astron. Telegram, 6635
Grazian A. et al., 2015, A&A, 575, A96
Greiner J. et al., 2008, PASP, 120, 405
Greiner J. et al., 2011, A&A, 526, A30
Grogin N. A. et al., 2011, ApJS, 197, 35
Guo Y. et al., 2016, ApJ, 833, 37
Heger A., Fryer C. L., Woosley S. E., Langer N., Hartmann D. H., 2003, ApJ, 591, 288
Henden A. A., Templeton M., Terrell D., Smith T. C., Levine S., Welch D., 2016, VizieR Online Data Catalog, 2336
Hjorth J. et al., 2012, ApJ, 756, 187
Howell D. A. et al., 2013, ApJ, 779, 98
Hudelot P. et al., 2012, VizieR Online Data Catalog, 2317
Hunter J. D., 2007, Comput. Sci. Eng., 9, 90
Ibar E., Ivison R. J., Biggs A. D., Lal D. V., Best P. N., Green D. A., 2009, MNRAS, 397, 281
Ilbert O. et al., 2005, A&A, 439, 863
Ilbert O. et al., 2006, A&A, 457, 841
Ilbert O. et al., 2009, ApJ, 690, 1236
Ilbert O. et al., 2013, A&A, 556, A55
Inoue A. K., 2011, MNRAS, 415, 2920
Inserra C., Smartt S. J., 2014, ApJ, 796, 87
Inserra C. et al., 2013, ApJ, 770, 128
Inserra C. et al., 2016, ApJ, preprint (arXiv:1604.01226)
Japelj J., Vergani S. D., Salvaterra R., Hunt L. K., Mannucci F., 2016, A&A, 593, A115
Jarvis M. J. et al., 2013, MNRAS, 428, 1281
Jerkstrand A., Smartt S. J., Heger A., 2016, MNRAS, 455, 3207
Jones E. et al., 2001, SciPy: Open Source Scientific Tools for Python, available at: http://www.scipy.org/
Kasen D., Bildsten L., 2010, ApJ, 717, 245
Kato D. et al., 2007, PASJ, 59, 615
Kennicutt R. C., Evans N. J., 2012, ARA&A, 50, 531
Kennicutt R. C., Jr, 1998, ARA&A, 36, 189
Kennicutt R. C., Jr, Lee J. C., Funes J. G. J. S., Sakai S., Akiyama S., 2008, ApJS, 178, 247
Kiewe M. et al., 2012, ApJ, 744, 10
Kissler-Patig M. et al., 2008, A&A, 491, 941
Knop R. et al., 1999, IAU Circ., 7128, 1
Kovács Z., Mall U., Bizenberger P., Baumeister H., Röser H.-J., 2004, in Garnett J. D., Beletic J. W., eds, Proc. SPIE Conf. Ser., Vol. 5499, Optical and Infrared Detectors for Astronomy. SPIE, Bellingham, p. 432
Kozyreva A. et al., 2017, MNRAS, 464, 2854
Kriek M., van Dokkum P. G., Labbé I., Franx M., Illingworth G. D., Marchesini D., Quadri R. F., 2009, ApJ, 700, 221
Krühler T., Schady S., 2017, Photometry and Stellar Masses for GRB Host Galaxies with Emission-line Spectra
Krühler T. et al., 2008, ApJ, 685, 376
Krühler T. et al., 2011, A&A, 534, A108
Krühler T. et al., 2015, A&A, 581, A125
Lang D., Hogg D. W., Mierle K., Blanton M., Roweis S., 2010, AJ, 139, 1782
Law N. M. et al., 2009, PASP, 121, 1395
Lawrence A. et al., 2007, MNRAS, 379, 1599
Le Fèvre O. et al., 2004, A&A, 417, 839
Le Fèvre O. et al., 2015, A&A, 576, A79
Lee J. C., Kennicutt R. C., Jr, Funes S. J. J. G., Sakai S., Akiyama S., 2009, ApJ, 692, 1305
Lee J. C. et al., 2011, ApJS, 192, 6
Lee N. et al., 2015, ApJ, 801, 80
Leget P.-F. et al., 2014, Astron. Telegram, 5718
Leitherer C. et al., 1999, ApJS, 123, 3
Leloudas G. et al., 2011, A&A, 530, A95
Leloudas G. et al., 2012, A&A, 541, A129
Leloudas G. et al., 2015a, A&A, 574, A61
Leloudas G. et al., 2015b, ApJ, 815, L10
Leloudas G. et al., 2015c, MNRAS, 449, 917
Lunnan R. et al., 2013, ApJ, 771, 97
Lunnan R. et al., 2014, ApJ, 787, 138
Lunnan R. et al., 2015, ApJ, 804, 90
Madgwick D. S. et al., 2002, MNRAS, 333, 133
Maiolino R. et al., 2008, A&A, 488, 463
Mannucci F., Salvaterra R., Campisi M. A., 2011, MNRAS, 414, 1263
Marchesini D. et al., 2007, ApJ, 656, 42
Martin D. C. et al., 2005, ApJ, 619, L1
Maseda M. V. et al., 2014, ApJ, 791, 17
Mauch T., Murphy T., Buttery H. J., Curran J., Hunstead R. W., Piestrzynski B., Robertson J. G., Sadler E. M., 2003, MNRAS, 342, 1117
McCracken H. J. et al., 2012, A&A, 544, A156
McCrum M. et al., 2014, MNRAS, 437, 656
McCrum M. et al., 2015, MNRAS, 448, 1206
McMullin J. P., Waters B., Schiebel D., Young W., Golap K., 2007, in Shaw R. A., Hill F., Bell D. J., eds, ASP Conf. Ser., Vol. 376, Astronomical Data Analysis Software and Systems XVI. Astron. Soc. Pac., San Francisco, p. 127

Michałowski M. J. et al., 2009, ApJ, 693, 347
Miller A. A. et al., 2009, ApJ, 690, 1303
Modjaz M. et al., 2009, ApJ, 702, 226
Moorwood A. et al., 1998, The Messenger, 94, 7
Moskvitin A. S., Fatkhullin T. A., Sokolov V. V., Komarova V. N., Drake A. J., Roy R., Tsvetkov D. Y., 2010, Astrophys. Bull., 65, 230
Murphy E. J. et al., 2011, ApJ, 737, 67
Muzzin A. et al., 2013, ApJ, 777, 18
Neill J. D. et al., 2011, ApJ, 727, 15
Nicholl M. et al., 2013, Nature, 502, 346
Nicholl M. et al., 2014, MNRAS, 444, 2096
Nicholl M. et al., 2015a, MNRAS, 452, 3869
Nicholl M. et al., 2015b, ApJ, 807, L18
Nicholl M. et al., 2016, ApJ, 826, 39
Nugent P., Aldering G., Phillips M. M., Richards G., Newberg H., Kent S., 1999, IAU Circ., 7133, 1
Ochsenbein F., Bauer P., Marcout J., 2000, A&AS, 143, 23
Ouchi M. et al., 2004, ApJ, 611, 660
Papadopoulos A. et al., 2015, MNRAS, 449, 1215
Pastorello A. et al., 2010, ApJ, 724, L16
Perley D. A. et al., 2016a, ApJ, 817, 7
Perley D. A. et al., 2016b, ApJ, 830, 13
Perley D. A. et al., 2016c, ApJ, 817, 8
Persson S. E. et al., 2013, PASP, 125, 654
Pirard J.-F. et al., 2004, in Moorwood A. F. M., Iye M., eds, Proc. SPIE Conf. Ser., Vol. 5492, Ground-based Instrumentation for Astronomy. SPIE, Bellingham, p. 1763
Planck Collaboration XVI, 2014, A&A, 571, A16
Quataert E., Shiode J., 2012, MNRAS, 423, L92
Quimby R. M., Castro F., Gerardy C. L., Hoeflich P., Kannappan S. J., Mondol P., Sellers M., Wheeler J. C., 2005, BAAS, 37, 171.02
Quimby R. M., Aldering G., Wheeler J. C., Höflich P., Akerlof C. W., Rykoff E. S., 2007, ApJ, 668, L99
Quimby R. et al., 2010a, Astron. Telegram, 2634
Quimby R. M. et al., 2010b, Astron. Telegram, 2979
Quimby R. M. et al., 2011a, Astron. Telegram, 3465
Quimby R. M., Gal-Yam A., Arcavi I., Yaron O., Horesh A., Mooley K., 2011b, Astron. Telegram, 3841
Quimby R. M. et al., 2011c, Nature, 474, 487
Quimby R. M. et al., 2013a, CBET, 3461
Quimby R. M., Yuan F., Akerlof C., Wheeler J. C., 2013b, MNRAS, 431, 912
Rakavy G., Shaviv G., 1967, ApJ, 148, 803
Reif K. et al., 1999, in Blouke M. M., Williams G. M., eds, Proc. SPIE, Vol. 3649, Sensors, Cameras, and Systems for Scientific/Industrial Applications. SPIE, Bellingham, p. 109
Rest A. et al., 2011, ApJ, 729, 88
Rice S. O., 1944, Bell Syst. Tech. J., 23, 282
Riess A. G. et al., 2004, ApJ, 607, 665
Robitaille T. P. et al., 2013, A&A, 558, A33
Roming P. W. A. et al., 2005, SSR, 120, 95
Salvaterra R. et al., 2012, ApJ, 749, 68
Sanders N. E. et al., 2012, ApJ, 758, 132
Santini P. et al., 2015, ApJ, 801, 97
Schirmer M., 2013, ApJS, 209, 21
Schlafly E. F., Finkbeiner D. P., 2011, ApJ, 737, 103
Schlegel E. M., 1990, MNRAS, 244, 269
Schmitt H. R., Calzetti D., Armus L., Giavalisco M., Heckman T. M., Kennicutt R. C., Jr,, Leitherer C., Meurer G. R., 2006, ApJS, 164, 52
Schulze S. et al., 2015, ApJ, 808, 73
Scovacricchi D., Nichol R. C., Bacon D., Sullivan M., Prajs S., 2016, MNRAS, 456, 1700
Scoville N. et al., 2007, ApJS, 172, 1
Smith N. et al., 2007, ApJ, 666, 1116
Smith N., Chornock R., Li W., Ganeshalingam M., Silverman J. M., Foley R. J., Filippenko A. V., Barth A. J., 2008, ApJ, 686, 467
Smith M. et al., 2014, Astron. Tel., 6739
Smith M. et al., 2016, ApJ, 818, L8
Sobral D., Best P. N., Smail I., Mobasher B., Stott J., Nisbet D., 2014, MNRAS, 437, 3516
Sorokina E., Blinnikov S., Nomoto K., Quimby R., Tolstov A., 2016, ApJ, 829, 17
Speagle J. S., Steinhardt C. L., Capak P. L., Silverman J. D., 2014, ApJS, 214, 15
Stalder B., Stark A. A., Amato S. M., Geary J., Shectman S. A., Stubbs C. W., Szentgyorgyi A., 2014, in Proc. SPIE, Vol. 9147, Ground-based and Airborne Instrumentation for Astronomy V. SPIE, Bellingham, p. 91473Y
Stanway E. R., Eldridge J. J., Becker G. D., 2016, MNRAS, 456, 485
Stoll R., Prieto J. L., Stanek K. Z., Pogge R. W., 2013, ApJ, 773, 12
Svensson K. M., Levan A. J., Tanvir N. R., Fruchter A. S., Strolger L.-G., 2010, MNRAS, 405, 57
Tasca L. A. M. et al., 2015, A&A, 581, A54
Terlevich R., Silich S., Rosa-González D., Terlevich E., 2004, MNRAS, 348, 1191
Thöne C. C., de Ugarte Postigo A., García-Benito R., Leloudas G., Schulze S., Amorín R., 2015, MNRAS, 451, L65
Tody D., 1986, in Crawford D. L., ed., Proc. SPIE Conf. Ser., Vol. 627, Instrumentation in Astronomy VI. SPIE, Bellingham, p. 733
Tomczak A. R. et al., 2014, ApJ, 783, 85
Tonry J. L. et al., 2012, ApJ, 750, 99
van der Walt S., Colbert S. C., Varoquaux G., 2011, Comput. Sci. Eng., 13, 22
Vergani S. D. et al., 2015, A&A, 581, A102
Vinko J. et al., 2012, American Astronomical Society Meeting Abstracts #219, 436.04
Vreeswijk P. M. et al., 2014, ApJ, 797, 24
Wardle J. F. C., Kronberg P. P., 1974, ApJ, 194, 249
Whitaker K. E., van Dokkum P. G., Brammer G., Franx M., 2012, ApJ, 754, L29
Whitaker K. E. et al., 2014, ApJ, 795, 104
Woosley S. E., 2012, in Kouveliotou C., Wijers R. A. M. J., Woosley S., eds, Models for Gamma-Ray Burst Progenitors and Central Engines. Cambridge Univ. Press, Cambridge, p. 191
Woosley S. E., Blinnikov S., Heger A., 2007, Nature, 450, 390
Wright E. L. et al., 2010, AJ, 140, 1868
Wyder T. K. et al., 2005, ApJ, 619, L15
Yagi M., Kashikawa N., Sekiguchi M., Doi M., Yasuda N., Shimasaku K., Okamura S., 2002, AJ, 123, 66
Yan L. et al., 2015, ApJ, 814, 108
Yan L. et al., 2017, ApJ, 840, 57
Yates R. M., Kauffmann G., Guo Q., 2012, MNRAS, 422, 215
Yoldaş A. K., Krühler T., Greiner J., Yoldaş A., Clemens C., Szokoly G., Primak N., Klose S., 2008, in Galassi M., Palmer D., Fenimore E., eds, AIP Conf. Proc., Vol. 1000, Gamma-Ray Bursts. Am. Inst. Phys., New York, p. 227
Yoon S.-C., Langer N., 2005, A&A, 443, 643
York D. G. et al., 2000, AJ, 120, 1579
Young D. R. et al., 2010, A&A, 512, A70
Yuan F. et al., 2007, BAAS, 39, 105.05
Zahid H. J., Dima G. I., Kudritzki R.-P., Kewley L. J., Geller M. J., Hwang H. S., Silverman J. D., Kashino D., 2014, ApJ, 791, 130

SUPPORTING INFORMATION

Supplementary data are available at *MNRAS* online.

Appendix A. Data Table.
Appendix B. Spectral Energy Distribution Fits.
Appendix C. Postage Stamps.
Appendix D. Statistical Properties of the Comparison Samples.

[1] *Department of Particle Physics and Astrophysics, Weizmann Institute of Science, Rehovot 7610001, Israel*
[2] *Instituto de Astrofísica, Facultad de Física, Pontificia Universidad Católica de Chile, Vicuña Mackenna 4860, 7820436 Macul, Santiago, Chile*
[3] *Millennium Institute of Astrophysics, Vicuña Mackenna 4860, 7820436 Macul, Santiago, Chile*
[4] *Max-Planck-Institut für extraterrestrische Physik, Gießenbachstraße, D-85748 Garching, Germany*
[5] *Dark Cosmology Centre, Niels Bohr Institute, University of Copenhagen, Juliane Maries Vej 30, DK-2100 Copenhagen, Denmark*
[6] *Departamento de Física Aplicada I, Unidad Asociada Grupo Ciencia Planetarias UPV/EHU-IAA/CSIC, E.T.S. Ingeniería, Universidad del País-Vasco UPV/EHU, Alameda de Urquijo s/n, E-48013 Bilbao, Spain*
[7] *Ikerbasque, Basque Foundation for Science, Alameda de Urquijo 36-5, E-48008 Bilbao, Spain*
[8] *Instituto de Astrofísica de Andalucía (IAA-CSIC), Glorieta de la Astronomía s/n, E-18008, Granada, Spain*
[9] *ESO, Alonso de Cordova 3107, Vitacura, Santiago de Chile, Chile*
[10] *Instituto de Física y Astronomía, Universidad de Valparaíso, Avda. Gran Bretaña 1111, Valparaíso, Chile*
[11] *Cavendish Laboratory, University of Cambridge, 19 JJ Thomson Avenue, Cambridge CB3 0HE, UK*
[12] *Kavli Institute for Cosmology, University of Cambridge, Madingley Road, Cambridge CB3 0HA, UK*
[13] *Space Science Institute, 4750 Walnut Street, Suite 205, Boulder, CO 80301, USA*
[14] *Mullard Space Science Laboratory - University College London, Holmbury Rd, Dorking RH5 6NT, UK*
[15] *INAF – Osservatorio Astrofisico di Arcetri, Largo Enrico Fermi 5, I-50125 Firenze, Italy*
[16] *Las Campanas Observatory, Carnegie Observatories, Casilla 601, La Serena, Chile*
[17] *Heidelberger Institut fur Theoretische Studien, Schloss-Wolfsbrunnenweg 35, D-69118 Heidelberg, Germany*
[18] *Institute for Astronomy, University of Hawaii, 2680 Woodlawn Drive, Honolulu, HI 96822, USA*
[19] *Smithsonian Astrophysical Observatory, 60 Garden Street, Cambridge, MA 02138, USA*
[20] *Department of Astronomy, University of Texas at Austin, Austin, TX 78712, USA*

This paper has been typeset from a TEX/LATEX file prepared by the author.